Large Impacts of Small Particles: The Effects of Active Particles on Colloidal Gels and Crystals and of Inulin Microparticles on Gut Retention in Mice

by

Keara Therese Saud Greatwood

A dissertation submitted in partial fulfillment
of the requirements for the degree of
Doctor of Philosophy
(Materials Science and Engineering)
in the University of Michigan
2022

Doctoral Committee:

Professor Michael J. Solomon, Co-Chair
Professor Sharon C. Glotzer, Co-Chair
Professor Brian J. Love
Professor Robert M. Ziff

Keara T. S. Greatwood

ktsaud@umich.edu

ORCID iD: 0000-0001-8456-2139

Dedication

To my mom and dad for their continued love, support, and example.

And to Angelica Rose Galvan for continually inspiring and reminding me of the humanity in all that we do.

Acknowledgements

Ubuntu – "I am because you are"

Ubuntu is a word from the Zulu language that I was fortunate enough to be introduced to in my study abroad experience in South Africa. Though there are many interpretations and applications of the word, one common understanding is that ubuntu is the recognition that we are all bound to each other in ways we cannot see. It is a principle (or word) used by many, most notably: Nelson Mandela. This word has found meaning in many aspects of my life. However, at the end of this Ph.D. journey, ubuntu feels more relevant than before because this dissertation only exists because of you all. Though the words here are my own (with input, of course, from my adviser and wonderful collaborators), they have been inspired, encouraged, and motivated by so many others before and beside me – whether they (you) realize it or not. And so, to you all, I am so thankful.

The Ph.D. is no walk in the park. The professor of my "Intro to Engineering" class at NC State, Dr. Laura Bottomley, said the Ph.D. isn't about smarts but about stubbornness and, boy, was she right. I found myself ready to quit many times throughout the six years, but the support and encouragement from so many people kept me here, kept me stubborn. That's not to say that quitting the Ph.D. is easy; in many cases that is the harder thing to do, and I don't think that is acknowledged enough. However, I do believe that this Ph.D. and these past few years at Michigan are for a reason, a reason that I don't know the full extent of even now. And I wouldn't be closing this chapter without the presence of so many people in my life. For much of my Ph.D.,

the only thing that kept me going was the idea of acknowledging these people. And so it is with great pleasure that I am now able to do just that, even if it is in this simple way.

To begin, I need to thank my adviser, Dean Michael J. Solomon. I came to Michigan with the intention of doing something that ultimately fell through before I even arrived. To say I was at a loss for what to do would be an understatement. However, upon Prof. Sharon Glotzer's recommendation, I talked to you and found a sort of haven in your group (as many others have). Though you have had many responsibilities that could have resulted in little interaction with your students, you somehow made the time, and consistently at that. I am extremely grateful for the sacrifices you made to make this possible. In addition, your thoroughness and precision has helped develop me as a scientist beyond what I thought possible. Thank you for supporting not only this development in core group-related research projects but also in my pursuits of a food science research project. Through this pursuit, you have helped me apply our group's expertise in ways that I know have better prepared me for future endeavors. Beyond research, your work to move our university forward will continue to be an inspiration.

I would also like to thank my co-adviser, Prof. Sharon Glotzer. As mentioned before, Sharon is the reason why I found the Solomon group. She continues to be a fabulous role model for what a female in STEM can be. Additionally, many of her amazing students have supported much of this Ph.D. work. I would additionally like to thank my other committee members Prof. Brian Love and Prof. Robert Ziff. Prof. Love has offered invaluable support and perspective through his classes and at particularly challenging times. Through his fractals class, Prof. Ziff has helped deepen my understanding of fractal gels (the system studied in Chapter 2 of this dissertation). He also continually reminds me of the inherent joy of learning. Thank you.

I am also so thankful for my many research collaborators. Dr. Megan Szakasits worked with me in the active colloidal gel space. She not only helped provide a strong foundation and direction for my research after her departure but has also been a role model for navigating STEM as a female. Thank you for all you have taught me. Prof. Mahesh Ganesan worked with me in Chapter 2 of this dissertation, helping bring ideas to (modeling) life and teaching me so much along the way. Aside from his pivotal role in the JoR paper (Chapter 2), he totally transformed our group dynamics. His genuine passion for learning and teaching is contagious. I cannot (and would not want to) imagine the 2019 – 2021 and COVID years without him. Thank you for all you have done for me and our group. Julia Roarty was one of my undergrad researchers whose assistance in experimental setup made Chapter 2 possible. Ryan King helped in the creation of the code used to analyze the colloidal crystals in Chapter 3. I cannot thank you enough for so selflessly offering your help and expertise. I am also grateful to Dr. Sabina Wilkanowicz and Jin Xu for their contributions to Chapter 4 of this dissertation. Without Sabina, this final project would not even exist as an idea. Sabina first introduced me to electrohydrodynamic processing in 2018 which is the foundation of Chapter 4. She has taken me under her wings in more ways than one. I don't know where I'd be without her guidance and perspective on research and life. Thank you for being there for me in ways that you never had. And thank you, Jin, for being open to this new project and for your understanding as we navigated the complexities of an interdisciplinary project. I have learned so much from you about the pharmaceutical science space. This project has been a highlight of my Ph.D. experience.

I also need to thank the numerous members of the Solomon group – Carlos Silvera Batista, Sepdieh Razavi, Yanliang Liu, Maria Ma, Yufei Wei, Megan Szakasits, Ryan Hall, Nina Gasbarro, Rachael Hamilton , Peng-Kai Kao, Tianyu Liu, Joanne Beckwith, Alice Sneha George,

Tianyu Liu, Clémence Abriat, Syahidah Mohd Khairi, and Chih-Mei Young. I consider myself so lucky to have been surrounded by such brilliant and caring people. From the very beginning when Yanliang Liu told me "Your health is more important than this experiment", I knew I was in the right group. I've learned so much from all of you. I want to thank Peng-Kai Kao for countless walks and talks, for being there in the good and bad, and for constantly (and perhaps simply) showing up. You have been the source of so much laughter and fun even when there wasn't much to smile about. Thank you, Nina, for making me feel seen and validated. Thank you, Joanne Beckwith, for being there for my first grad school breakdown and for encouraging me even now from afar in this final stretch. Thank you Tianyu Liu for your positivity and generous heart. Thank you, Yufei Wei, for always being so willing to help me with the rheometer. Thank you, Ryan Hall, for always being eager to share advice and to try new things. Thank you, Alice Sneha George, for always being willing to offer a helping hand. Thank you, Clémence Abriat, for your friendship and encouragement along the final stretch. And thank you, Joanne and Megan, for introducing me to Dom's donuts – grad school simply wouldn't have been as sweet without Dom's.

One former member of the Solomon group who has had a particularly profound impact on me is Prof. Carlos Silvera Batista. I worked with Carlos in my first year of graduate school. In this single year, Carlos prepared me for the Ph.D. in ways that I continue to realize today. Thank you for taking the time to help me truly learn, for setting an example and ideal for the Ph.D. from the start, for seeing me as a person, and for helping me to see others as well. I wouldn't have made it to this point without you and your support. I cherish the mentorship and friendship that has evolved over the years. In addition to all this, you have also introduced me to your wife, the amazing Dean Julianne Vernon. Julie, you came into my life as a more official mentor at one of

my lowest points. However, even before this, you were a role model for me. Thank you for taking time to mentor me and help me navigate this final year. I don't want to imagine what it would have bene like without you. You have empowered me to be a more confident version of myself and to own my decisions. Thank you, both.

Another person I am blessed to have met through this graduate school experience is Dr. Tim Chambers. I had the privilege of GSIing with Tim for two MSE lab courses. First as a mentor and now as a friend, Tim has been there for so much of this Ph.D. journey and so many critical life decisions. Thank you for being there and for keeping me excited about learning in all aspects of life.

I am additionally so incredibly thankful for Ms. Angelica Rose Galvan. You were one of the first people at Michigan who truly inspired me and continues to inspire me every day. Thank you for your contagious and genuine enthusiasm for learning, for your contributions of your unique "interstitial" expertise to the inulin project, for continuing to remind me of the humanity in all of us, and for so much more.

This work was also only possible because of the foundation and continued support I've received from the Park Scholarships program at NC State. Thank you especially to Eva Feucht for always being ready and eager to connect me with someone who had experience in a problem or question I had.

I would also like to thank the many friends who have provided support throughout the Ph.D. Thank you, Emily Cengel, for being there and reminding me that I am an empowered young manifestation of the goodness of God who could do this. Thank you, Emily McGuinness for many Zoom calls as we both navigated this Ph.D. and academic space. Thank you, Anna White, for being my first writing buddy and for your general positivity through so many lows of

grad school. Thank you to Joey Valle for being a writing buddy and for inspiring me to look beyond this work. Thank you to Luisa Barrera for countless baked goods, fruit picking outings, and venting when that's all that could be done. Thank you to Andrea Lupini for reminding me to take a pause and enjoy the amazing people around me. Thank you to Bobby Graham for being a light in my NCRC experience, taking a pause and sharing some caffeine. Thank you to Kathleen Chou for so much encouragement especially in this final stretch. Thank you to Anna Michmerhuizen for encouraging me academically and spiritually. I'm also so grateful for the numerous people I've met and community I've found in GradSWE and GradCru. All these and many more have impacted me in this pursuit more than you know.

I also need to thank my family for their unwavering support through all of this. I am so privileged to have been raised in a household where science and science experiments were "cool" - where the "Mobius strip" *is* a frequent topic at holiday gatherings. I wouldn't be here without this foundation and the example that my parents have set forth for me and all my siblings – thank you, Mom and Dad. More than this, I am also so fortunate to be surrounded by family members who have been there for me emotionally. I can't imagine closing this chapter without you here. Sam and Dylan, thank you for letting me escape to your Royal Oak home, helping me with my own home, and sharing your precious pup. I couldn't have made it through the first few Michigan winters without you also in Michigan. Thank you to my brothers, Denvir and Sean, for lending an ear and reminding me to "Raise it up". And thank you to all my family members (by blood and by marriage, the Saud, Denvir, and Greatwood families) for the countless phone calls and visits which helped remind me that I am not alone.

And last, but certainly not least, I'd like to thank my husband, Colin Greatwood. The significant other of a Ph.D. student takes the brunt of it all. Colin, through this process, you have

seen some of the worst in me, but for some reason you've stuck around and even cooked most of my meals this past year. You've supported me in countless ways: thank you for helping repair various lab equipment; thank you for listening to my ramblings about what my particles were doing on any given day; thank you for bringing me flowers to lab just to cheer me up (even though we both know they'd die in a few days because of the lack of sunlight); and thank you for making this house a home where so many people have been able to come and be in community. There are so many more things I could list off that you've done that I'm grateful for and that have made this Ph.D. possible, but what I believe is the most important is you continuing to remind me of the more important things in life. This perspective is one I too easily forget, and without which, none of this would matter. Thank you for being my rock.

To conclude, no words could ever do justice to all that these and so many others have done for me in this pursuit, and I need to concede that it is impossible for me to acknowledge all the people who have made it possible. As given by the title of this dissertation ("Large impacts of small particles"), I believe that even the "smallest" of encounters can have a profound impact, and in my six years here, there have been countless things, people, and experiences that have encouraged me in this pursuit (and beyond). Though I may not be able to recognize everything and everyone, please know that "I am because you are." Thank you.

Table of Contents

List of Tables

List of Figures

Abstract

In this dissertation, we investigate how colloidal particles affect and interact with their environments. Two colloidal particles are studied: active Janus particles and electrosprayed polyvinyl alcohol (PVA) / inulin microparticles. Inspired by the motion seen in nature, active colloids are self-propulsive and inherently out of equilibrium. We study how active colloids affect nonlinear rheological properties of colloidal gels and interact with defect-rich colloidal crystals. Inulin is a prebiotic fiber commonly used to modify rheological properties of foods and, more recently, to work synergistically with cancer immunotherapies. We study how electrospraying inulin into microparticle form affects its rheological properties and gut retention.

In chapter two, we explore how a small fraction of active particles (active-to-passive particle ratio of ~1:1200) affects the yield stress behavior of colloidal gels. The active particle system used is a platinum Janus colloid whose active motion results from the asymmetric decomposition reaction of hydrogen peroxide. Colloidal gels are prepared by the addition of a divalent salt to a suspension of polystyrene microparticles and Janus particles in water and hydrogen peroxide. We find that active particles cause a significant yield stress reduction (up to a factor of three); however, no change in yield strain is observed. We explain how the small number of active particles can have this rheological effect through modeling. We use a combined theory of how activity changes the spring constant of interparticle bonds in the gel with an argument that the number of active clusters – rather than number of active particles – controls the rheological impact of the activity. The modeling of this theory agrees well with experimental data.

In chapter three, we explore how a small fraction of active particles (active-to-passive particle ratio of ~1:720) interact with and affect defect-rich colloidal crystal monolayers. This study utilizes the same platinum Janus particle as chapter two. The crystal monolayer is made of passive, Brownian particles with diameters four times that of the Janus particles. These larger particles are assembled into a crystal monolayer by an alternating current electric field. We find that active particles cause a reduction in void number (by up to ~50%) but an increase in void size and anisotropy (by up to 190% and 40%, respectively). We examine how these changes may relate to differences in the microdynamics of active particles by region. We specifically compare microdynamics in void, void-adjacent (within three particle diameters of a void), and interstitial regions. At the highest active energy, dynamics are increased in void-adjacent regions, about the same in interstitial regions, and decreased in void regions compared to the ensemble dynamics.

In chapter four, we investigate the relationship between the rheological properties and gut retention of PVA-inulin microparticles. Inulin is a fructan polysaccharide with prebiotic properties which is found in many vegetables. PVA is a biocompatible polymer that can exhibit mucoadhesive properties. Microparticles are created via the electrospraying method which utilizes large electrical potential differences to create nano- and micro-sized features. In suspension, we determine that microparticle form causes shear thinning behavior. Furthermore, the release and dissolution of inulin causes an increase in sample modulus with time. When administered to mice, the PVA-inulin microparticle suspensions exhibit signs of greater gut retention than as-received inulin and mixtures of equivalent concentrations. We hypothesize that gut retention depends on established mucoadhesive properties of PVA and rheological properties of the samples.

Chapter 1 Introduction

The underlying subject of this work is the exploration of the impact of different colloidal particles on their environments, particularly when they are synthesized to perform a function such as locomotion or dissolution. Colloids are a mixture of particles that range in diameter, a, from ~5 nm to ~5 um and are dispersed in a medium. The engineering science research performed here is an interdisciplinary combination of colloidal science, active motion, colloidal assembly, and rheology. Before delving into the specifics of our contributions to these areas (Chapters 2 – 4), in this chapter we first introduce the fundamental concepts from these fields that are critical to the understanding of this work and its impact.

1.1 Colloids

Colloids are ubiquitous: some examples of colloids in everyday life include milk – a colloidal system of fat globules suspended in a water-based solution; paint – a colloidal system where pigment particles are suspended in water or oil-based solutions; and toothpaste – a colloidal system of abrasive particles in a water-based solution. The particles in these systems can vary in shape from spheres to rods and ellipsoids to faceted polyhedral and more. Shape can play an important role in the behavior and interactions of colloidal particles [1], [2]. For the majority of the work in this thesis, we use the simplest shape of a colloid: a sphere. Properties of colloids important to their function that we review here are: their dynamics, their interactions and assembly, and their rheological properties.

1.1.1 Brownian dynamics

A key feature of colloids is that in the dilute case, particle motion is dominated by both Brownian motion and viscous forces. Brownian motion is motion from random particle fluctuations that results from thermal energy. Specifically, thermal energy causes collisions of molecules with the larger colloidal particles which ultimately drive colloidal motion and diffusion. This motion is stochastic. Viscous forces come about from the drag experienced by a particle in a viscous medium described by Stokes' law and from inertia. The diffusive process of a spherical colloidal particle can be described with the Stokes-Einstein equation for the diffusion coefficient, D, given in Equation (1-1)

$$D = \frac{k_B T}{6\pi\eta r} \tag{1-1}$$

Where $k_B T$, is Boltzmann's constant, T is temperature, η is the solvent viscosity, and r is the particle radius [1]. This diffusive process can be observed through many techniques including dynamic light scattering and particle tracking from confocal laser scanning microscopy (CLSM). In this thesis, CLSM and particle tracking are used and will be described in more detail. Particle trajectories that are obtained from particle tracking can be used to calculate a particle's mean-squared-displacement (MSD). For a Brownian particle, referred to as a passive particle in this thesis, the MSD, $< r^2(\Delta t) >$, can be described in the long time limit by the following equation (1-2)

$$< r^2(\Delta t) > = 2dD\Delta t \tag{1-2}$$

Where d is the Euclidean dimension, D is the diffusion coefficient and Δt is the lag time. The brackets indicate an ensemble average over all possible trajectories of the particle. From this equation, it can be seen that the MSD of a Brownian particle vs lag time will produce a linear plot. If the particle is hindered by obstacles or inhibited by some type of confinement, the MSD may be no longer linear; sub-diffusive behavior is observed in such cases [3], [4].

1.1.2 Active colloids and dynamics

A relatively new type of colloid, known as an active colloid, has been shown to defy this typical diffusive process. Active colloids are inspired by the motion observed in nature, for example flocks of birds, swarms of fish, colonies of bacteria. The self-propulsion of active colloids arises from local gradients around individual particles which are produced from asymmetric conversion of external energy [5]. The external energy can come from many sources including light [6]–[9], electric fields [10]–[13], magnetic fields [12], [14], [15], and chemical reactions [16]–[20]. The energy conversion is usually made to be asymmetric through the design of the particle itself, for example, by making the colloids have two different faces (Janus), or by increasing the anisotropy of the particle. The resulting motion is often described as super diffusive. Specifically, the MSD vs lag time plot of active colloids is quadratic at short lag times. The MSD of active colloids for this limiting case at short lag times (Δt << rotational diffusion time, τ_R) is given in equation (1-3) below:

$$< r^2(\Delta t) > = 4D\Delta t + v^2\Delta t^2 \qquad (1\text{-}3)$$

Where D is the diffusion coefficient, Δt is the lag time, and v is the active colloid velocity [21]. From this and the work from Takatori et al., the energy of active colloids can also be calculated and compared to thermal energy, k_BT. Specifically, the active energy of a particle, E_A, follows equation (1-4):

$$E_A = \xi v l \qquad (1\text{-}4)$$

Where ξ is the hydrodynamic drag coefficient, v is the particle velocity, and l is the active particle run length which is equivalent to $l = \tau_R V = 8\pi\mu a^3 V/k_B T$ [22]. Here τ_R is the is a reorientation time, related to the rotational diffusivity of the active colloid.

1.2 Colloidal interactions and assembly

Colloids can assemble into many states depending on the volume fraction of the colloidal particles as well as the strength and direction of the forces present. These forces are a consequence of the potential energy landscape of the colloidal system. If the potential energy is pairwise additive, the contribution of the particle interactions can be characterized by the pair potential between particles, which itself can be scaled on the thermal energy of the system. High temperatures and small pair potentials yield to weakly interacting systems; lower temperatures and large pair potentials indicate strong deviations from ideal behavior. Some of the common assembled states of colloidal systems include stable dispersions, unstable aggregation and liquid-liquid separation, gels, crystals, and glasses [1], [23], [24]. A summary of the relative temperatures, or pair potential interactions, and volume fractions that induce these states is provided in Figure 1-1. In the following sections, we will first describe the typical interactions present at the colloidal scale. We will then describe two of the states on this diagram in further detail: colloidal gels and colloidal crystals. The effect of active colloids on these states will be the focus of Chapters 2 and 3, respectively.

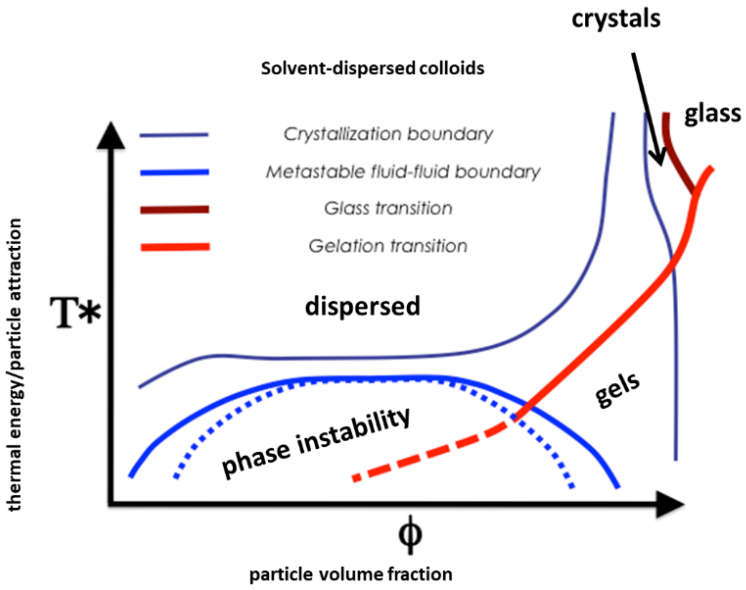

Figure 1-1: Summary of the relative temperatures, or pair potential interactions, and volume fractions and the resulting colloidal states [25]

For colloids, the interface-to-volume ratio is large enough that their behavior is affected by surface properties of the particle [26]. Specifically, colloidal interactions are primarily dominated by repulsive electrostatic forces and attractive van der Waal forces. The former are surface interactions; the latter are volumetric in nature. Electrostatic forces stem from the charge on the surface of particles and can be moderated by ions in the dispersing solvent. Solvated ions determine the system's Debye length, κ^{-1} , which is the characteristic length at which charge interactions between colloidal pairs are screened. Van der Waal forces arise from random, local fluctuations of dipoles within in a single particle. They are less sensitive to ions or electrolyte concentrations in the dispersing solvent, but instead are most strongly related to the frequency-dependent dielectric properties of the interacting particles and the solvent in which they are dispersed [1], [26], [27]. Together, electrostatic and van der Waal forces are frequently referred to as DLVO forces, named after the scientists who developed the theory of their additive nature for colloids: Derjaguin, Landau, Verwey, and Overbeek [26], [27].

The effect of DLVO forces can be quantified and modeled through the calculation of particle pair potentials. Particle pair potentials are a powerful way of predicting colloidal stability and assembly. The total potential, W(D), between two colloidal particles is the sum of the van der Waal's potential, $W_{vdw}(D)$, and the electrostatic potential, $W_{el}(D)$:

$$W(D) = W_{el}(D) + W_{vdw}(D) \quad (1\text{-}5)$$

Here, D is the surface-to-surface separation between the two particles [27]. Both the electrostatic potential and the van der Waal potentials are geometry and material dependent. (Recall that the force a colloid experiences is the gradient of the pairwise additive potential energy.) The electrostatic potential between two spheres of the same size is given by:

$$W_{el}(D) = \frac{R}{2} Z e^{-\kappa D} \quad (1\text{-}6)$$

Where R is the particle radius, Z is an interaction constant related to the electrophoretic mobility of the particle and the dielectric properties of the medium, and κ^{-1} is the Debye length [27]. For two identical spheres with a separation that is smaller than the particle radius, R, the van der Waal's potential follows:

$$W_{vdw}(D) = -\frac{AR}{12D} \quad (1\text{-}7)$$

Where A is the Hamaker constant. The Hamaker constant depends on both the refractive indices and dielectric permittivities of the particle as well as of the suspending medium [27].

Another attractive force that the author would like to highlight (though not a focus of this dissertation) are depletion forces. Depletion forces exist in the presence of a nonadsorbing polymer and originate from a drive to maximize entropy. Specifically, when a solution contains a non-adsorbing polymer, osmotic pressure between the bulk part of a solution containing a non-adsorbing polymer and a polymer-depleted region between two larger particles will push

particles together to maximize the entropy of the polymer [1]. Depletion forces can be a particularly useful tool for colloidal research and implications for depletion forces as it relates to this work will be discussed in Chapter 5.

1.2.1 Colloidal gels

By manipulating these potential interactions, different colloidal states can be achieved, including colloidal gels. Colloidal gels are a non-equilibrium state made of a network of particles arrested in a liquid. The arrest occurs due to strong, short-range interactions between the particles. This network gives the gel its structure and solid-like properties which are relevant in many industries including paints and coatings [28], food [29]–[31], and consumer products [32]. Exact properties can be controlled by parameters such as particle volume fraction, solvent and solute used, and the specific gelation mechanism [33]–[35].

In this thesis, colloidal gels are made using a spinodal decomposition mechanism called diffusion limited cluster aggregation (DLCA). DLCA gelation occurs when electrostatic repulsive forces are shielded – usually by divalent salts [36], [37]. With this shielding, diffusive particles will strongly and irreversibly link when they encounter each other [38]. DLCA gels are well studied both structurally and mechanically [39]–[41]. The structure of DLCA gels can be described using the radial distribution function, g(r). The radial distribution function measures the probability of finding a particle at a distance, r, from particle at the origin. The g(r) for DLCA gels is given below:

$$g(r) = (\frac{c}{a^{d_f}})r^{d_f-3}e^{-(\frac{r}{R_c})^{\gamma}} \quad (1\text{-}8)$$

where c is the prefactor set by the density of particles in a cluster, a is the particle radius, d_f is the fractal dimension, R_c is the average cluster size and γ is a cutoff exponent [42], [43]. The solid-

like properties of DLCA gels can be described by the linear elastic modulus, G'. The relationship between the structure and elastic properties of DLCA gels made with spherical particles follows:

$$G' = \kappa a^{-1} \phi^{(3+d_B)/(3-d_f)} \quad (1\text{-}9)$$

Where κ is the spring constant between two particles (determined using the pair potential), a is the particle diameter, ϕ is the volume fraction, d_B is the elasticity exponent, and d_f is the fractal dimension [35]. This equation assumes fractal cluster structure, typical in DLCA gels for $\phi <$ 0.1. Methods to measure G' will be discussed further in Section 1.3

1.2.2 Colloidal crystals

Colloidal systems can also spontaneously assemble into crystals through control of particle volume fraction and particle interactions. Crystalline phases of colloids have been proposed as templates for membrane [44], [45] and battery [46], [47] applications. Furthermore, when particles fall in a specific size range, colloidal crystals can produce structural color and other useful optical properties due to Bragg diffraction [48]–[52].

Crystallization in colloids can occur with increasing volume fractions as shown in Figure 1-1 and reported experimentally by Pusey and van Megen [53]. However, the high particle concentrations required for these crystals can be challenging to work with. High particle concentrations will often become jammed or glassy before reaching the crystal phase or can simply be difficult and time-consuming to generate [53]–[55]. Instead, crystallization in initially dilute colloidal suspensions can be induced through the application of external fields such as electric fields [51], [56], [57], gravity [58], [59], evaporation [48]–[50], [60], and shear [61], [62]. Application of such fields can ameliorate kinetic effects that retard or prevent crystallization.

In this dissertation, colloidal crystals are formed using coplanar AC electric fields at high frequencies. This method of crystallization has many advantages such as its speed [56], [57], [63], its applicability to many materials [63], [64], and its reversibility [56], [57], [63]. The presence of the AC field in a coplanar configuration induces crystallization through a combination of dielectrophoresis (DEP) and dipole-dipole interactions. DEP results from the interaction of a nonuniform electric field with the induced dipole of a particle. A particle with an induced dipole moves toward or away from strong field regions depending on its dielectric constant relative to the dielectric constant of the solvent. In both cases they act to minimize the system's potential energy [65]. In the device described in Chapter 3, this involves particles moving to the center of the two electrodes, effectively increasing the local volume fraction in those regions. Dipole-dipole interactions arise between two particles with field-induced dipoles. This force is attractive by nature and aligned in the field direction. Particles will again act to minimize their potential energy, but instead by aligning their dipoles; this results in chaining in the direction of the field [65]. Together, these two interactions induce crystallization and the resulting order-disorder transition scales with r^3E^2 where r is the particle radius and E is the electric field strength [63], [65]. Though electric fields rapidly and reversibly crystallize a colloidal system, the resulting crystal quality can be far from perfect. Electric field assisted crystals often are polycrystalline and are embedded with defects such as vacancies and interstitials [56], [57]. Such defects can have profound effects on material properties [48], [49], [60], [66] As such, methods for improving crystal quality are desired and heavily researched [55], [57], [58]. Chapter 3 aims to inform one such way of improving crystal quality with active colloids.

1.2.3 Interactions with Active Colloids

Active colloids have drawn much interest because of their potential to affect the structure and properties these equilibrium states of colloids. For example, Palacci et al. found that one type of active colloid, polystyrene particles with a partially exposed hematite cube, will form "living" and dynamic crystals when in hydrogen peroxide and exposed to blue light [6]. Such dynamics are not possible in equilibrium systems. Active colloids have also been shown to autonomously find and repair cracks in electrical wiring [67] and anneal colloidal crystals at much faster rates than traditional thermal annealing [58]. The self-propulsive behavior has also found use in quicker oil collection for environmental remediation [68], more targeted drug delivery to the stomach tissues of mice [69], as well as alteration of gel structure and rheological properties [20], [70]. Despite these exciting implications of active colloids, much is still unknown about how they interact with and affect their environment [71]. Some studies have reported that active motion can be mediated by surfaces and interfaces [19], [72]–[74] or hindered by the presence of salt [10], [75] and by increases in solvent viscosity [76], [77]. Others have shown that active particles can activate passive particles and can act as cargo transporters [12], [78]–[81]. Chapters 2 and 3 of this thesis aim to elucidate some of the effects of active particles on colloidal gels and colloidal crystal

1.3 Rheological Properties of Colloids

Rheology is the study of how materials flow and deform. Named by the scientist, Eugen Bingham, the word rheology comes from the Greek word rhéos, or ῥέω, meaning "stream" or "flow" [82], [83]. Understanding the rheological properties of a material (or how the material flows) has important implications for many industries including food [84]–[88], paints and coatings [28], [89], [90], consumer products [91], [92] and pharmaceuticals [92]–[95]. For example, rheological properties like viscosity and yield stress relate to the texture and mouthfeel

of a food product. Understanding and controlling these properties can influence consumer experience and enjoyment [84]–[86]. Additionally, the viscosity and elastic modulus are critical for the shelf-life of consumer products and paint [89], [91] as well as for many production processes [85], [96], [97].

The rheology of a material can be measured through several techniques depending on the pertinent timescale and viscoelastic modulus of the material. Some techniques include mechanical rheometry, active microrheology, particle tracking microrheology, and atomic force microscopy [98]. In this dissertation, we use a rheometer to study the rheological properties of colloidal gels with embedded active particles (Chapter 2) and of inulin-based microparticle suspensions (Chapter 4). Shear rheometers generally measure three properties: shear stress (force applied per unit area, σ or τ), shear strain (the displacement or extent of deformation, γ), and time (t). These quantities can be applied either in oscillation or in steady shear flow. Oscillatory rheology involves the sinusoidal application of a stress or strain. Given the geometry parameters and the ratio of the stress to stain, the viscoelastic moduli can be calculated. The elastic (or storage) modulus, G', describes the energy stored when a strain cycle is applied; it is a quantification of how solid-like a material is and is the in-phase component of the stress. The viscous (or loss) modulus, G'' describes the energy that is lost when a strain cycle is applied; it is a quantification of how liquid-like a material is and is the out-of-phase component of the stress [98]. Equation (1-10) (which applies only to a sample in its linear regime – described below), gives the theoretical description of the measured shear stress in terms of these moduli.

$$\tau = G'\gamma_0 \sin(\omega t) + G''\gamma_0 \cos(\omega t) \qquad (1\text{-}10)$$

Here, τ is the measured shear stress, γ_0 is the applied shear strain amplitude, ω is the angular frequency of the applied strain, and t is time.

On the other hand, steady shear rheology involves the continuous application of a stress or strain. Given the instrument geometry parameters and the measurement of the time dependent stress and strain, rheological properties such as the viscosity can be calculated. Equation XX gives the equation for the viscosity of a simple Newtonian fluid:

$$\eta = \frac{\tau}{\dot{\gamma}} \tag{1-11}$$

Where η is the viscosity and $\dot{\gamma}$ is the shear rate.

In addition to oscillatory and steady shear rheology, one can additionally perform stress or strain-controlled experiments depending on the given application. In this dissertation we perform both. A common stress-controlled experiment is a creep experiment. For creep experiments, a fixed shear stress is applied, and the resulting strain is measured over time. These tests can provide information about the viscosity at low shear rates and can be very useful for viscoelastic systems with long relaxation times. Creep is performed and described further in Chapter 2. Common strain-controlled measurements are described in the next section on linear and nonlinear rheology.

1.3.1 Linear and Nonlinear rheology

There are two main categories of rheological measurements: linear and nonlinear. Linear rheological measurements occur at low strains where the strain varies linearly with stress and viscoelastic moduli are independent of the strain or strain amplitude. Linear rheology is useful for probing microstructural information. Nonlinear rheological measurements occur at higher strains where strain deviates from its linear dependance on stress. At these greater strains, the structure of the sample begins to change or yield. The onset of nonlinearity of a sample can be determined by, for example, performing an oscillatory strain amplitude sweep; the nonlinear

regime begins when the viscoelastic moduli is no longer independent of strain. A typical material response with strain will result in either a drop or brief overshoot before a drop [82], [99]. Both measurement types provide useful information about a material and how it will perform in material processing operations. Chapter 2 of this dissertation explores the nonlinear regime of colloidal gels with embedded active particles through three different rheological tests. Chapter 4 explores both the linear and nonlinear regime of inulin-based microparticle suspensions.

1.4 Prebiotics

Through our evolving understanding of the gut, gut health, and gut microbiota, the importance of prebiotic foods has become more apparent. The term prebiotic is currently defined as "a nondigestible compound that, through its metabolization by microorganisms in the gut, modulates the composition and/or activity of the gut microbiota, thus conferring a beneficial physiologic effect on the host." [100] In other words, a prebiotic food is one that is not digested in the stomach or small intestine, but instead by bacteria in the colon. Prebiotics can be found in many foods such as leeks, asparagus, garlic, bananas, and oats. In feeding the gut microbiota, prebiotics provide many health benefits, including improved health of the gut bacteria, metabolite production, improved mineral absorption, and improved immune system defense [100]–[102]. These health benefits have drawn much attention in recent years, but there is still much to be understood about prebiotics and how they impart their effects [101]. We contribute to this space by studying the rheology and gut retention of different physical forms of inulin, a prebiotic fiber found in leeks, asparagus, and chicory root (Chapter 4).

1.5 Research Objectives and Organization of the dissertation

The main objectives of this dissertation are to investigate the rich space of active matter and to better understand how active particles affect and interact with colloidal gels and colloidal crystals. These objectives are the main focus of Chapters 2 and 3, respectively. Another separate objective was to apply the fundamental knowledge of colloidal science and rheology to contribute to food science. Chapter 4 focuses on addressing this goal through the study of inulin (a prebiotic fiber found in many foods) and its rheological and gut retention properties. The results from these studies have a common theme highlighting how small particles (or small changes) can have great impacts on their surroundings.

In Chapter 2, we examine how embedded active particles affect the nonlinear rheology of colloidal gels. We observe significant rheological changes even with extremely small fractions of active particles. We explain this observation through modeling and a hypothesis that active particles can activate the cluster they are embedded in. This finding highlights how active particle interactions can be complex and contribute to greater effects than anticipated.

In Chapter 3, we study how active particles interact with defects in a colloidal crystal. These interactions are important for understanding how active particles may anneal colloidal crystals. We find that the properties of defect-rich void regions change with active motion. Furthermore, the microdynamics of these active particles depend on the microstructural region they are in. These results suggest that the microstructural region is important for annealing.

In Chapter 4, we create PVA-inulin microparticles using the electrospray technique and study their resulting rheological properties in suspension. We find that the microparticle form and the presence of inulin increases the viscoelastic moduli and extent of shear thinning. Moreover, we find that the PVA-inulin microparticles have signs of increased gut retention than

as-received inulin and mixtures of equivalent concentrations of materials. We hypothesize this increased gut retention is the result of the mucoadhesive properties of PVA and the rheological properties of the samples.

We conclude the dissertation with a summary of the contributions as well as suggestions for future work.

Chapter 2 Yield Stress Behavior of Colloidal Gels Embedded with Active Particles

2.1 Abstract

The yield stress behavior of colloidal gels with embedded active particles is studied with three experiments: start-up of steady shear, oscillatory strain amplitude sweep, and creep testing. Activity is generated by Janus particles with a platinum hemisphere; these particles undergo self-diffusiophoretic and self-electrophoretic motion in hydrogen peroxide solutions. The free particle active motion of the Janus colloids is consistent with an active energy of 25 times thermal energy at the highest hydrogen peroxide concentration studied. Consistent with prior work, the gels with embedded active particles display enhanced microdynamics and a reduction in linear viscoelastic moduli. Furthermore, at the activity levels studied, the yield stress decreases by as much as three-fold for gels with an active-to-passive particle ratio of only 1 to 1200. We additionally find the yield strain is independent of activity. The significant reduction in yield stress at a very low active-to-passive particle ratio is modelled by combining theory of how activity changes the spring constant of interparticle bonds in the gel with an argument that the number of active fractal clusters in the gel – rather than the number of active particles – drives the activity-induced softening of rheological properties. We estimate 1 in 40 fractal clusters in the gel is active due to the presence of an active particle. This approach explains how an extremely small fraction of active particles causes a substantial change in both linear and non-linear rheological properties. The results and modeling are potentially useful for the creation of gels with multi-state mechanical properties.

This chapter was adapted from a publication: K. T. Saud, M. Ganesan, and M. J. Solomon, "Yield stress behavior of colloidal gels with embedded active particles," *J. Rheol. (N. Y. N. Y).*, vol. 65, no. 2, pp. 225–239, 2021.Keara T. Saud and Michael J. Solomon conceived this research and designed the experiments. Keara T. Saud conducted the experiments with assistance from Julia Roarty. Keara T. Saud and Mahesh Ganesan conceived the theoretical explanation for the modeling. Mahesh Ganesan performed the modeling.

2.2 Introduction

Colloidal gels are a class of soft matter which are made of a sample-spanning network of particles. The network is generated by short-range attractive forces between the colloids [23]. This network is responsible for the solid-like viscoelastic properties of gels such as their elastic modulus and yield stress [39]–[41]; gels are important in industries such as paints and coatings [28], [103], foods [31], [84], [104], agricultural formulations, and consumer products [32]. One of the well-studied colloidal gel systems is the diffusion-limited cluster aggregation (DLCA) gel. DLCA gels are created through spinodal decomposition brought about by quenching particles in the dispersed state into a state dominated by strong, short-range attractive potential interactions between particles. The gelation mechanism yields the fractal cluster microstructure of DLCA gels. These fractal cluster properties of DLCA gels specify their viscoelastic properties [23], [35].

Under flow, the deformation-induced breaking and reorganization of network bonds in colloidal gels causes a solid to liquid transition, known as yielding [39], [41], [105]–[110]. This yielding and restructuring of colloidal gels is complex, and the structural transitions that generate it are not yet fully understood. The yield stress can be strain-rate dependent [41], [111]. In addition, different measurement techniques report different values of the yield stress for the same system [111], [112]. Common techniques to measure the yield stress include start-up of steady

shear, large amplitude oscillatory strain, and creep experiments [111]. Information available from yield stress measurements can be applied to engineer functional properties of gels, such as their product stability. The design of processing methods such as blending and mixing are also informed by such measurements [104], [111].

One limitation in their formulation and application is that gel mechanical properties are largely static; that is, their control post gelation is very limited. Parameters that determine gel rheology include particle size, solid volume fraction, solvency, salinity, and additive levels [41], [105], [113]. However, in many settings, reconfigurable mechanical properties are desired [28]. For example, in the paints and coating industry, a high product viscosity is desired for storage to maintain homogeneity, while low viscosity is desired upon application to prevent nozzle clogging, streaking, and other non-ideal coating processes [28]. Current technologies to induce such a change in viscosity requires additives such as associative thickeners [89]. However, by exploiting the properties of active matter, such reconfigurable properties are potentially accessible through properties of the gel network itself.

Active matter is comprised of entities which consume energy to self-propel or exert forces. Examples include flocking birds, swarming fish, and run-and-tumble bacteria such as *Escherichia coli*. [5], [114]. Active matter has been studied as a tool for self-assembly, microrobotics, electronics, environmental remediation, and complex fluids [115]–[118]. Colloidal forms of active matter exploit asymmetric conversion of external energy (such as from fuel or fields) around a particle to produce local gradients in electric or concentration fields. These local gradients induce self-phoretic motion of single particles [5]. Light [8], [119], magnetic fields [15], [120], electric fields [10], [121], and chemical reactions [16] are some of the methods available to induce the local gradients needed to generate active motion in colloidal systems. One extensively studied

synthetic active particle system is that of a platinum-coated Janus colloid activated by hydrogen peroxide (H_2O_2) [16], [17], [75], [122]–[124]. In this system, the platinum located on one hemisphere of the Janus particle catalyzes the asymmetric decomposition of H_2O_2 into H_2O and O_2. The specific mechanism of active displacement is a combination of self-diffusiophoresis and self-electrophoresis due to concentration and ion gradients, respectively [75].

Because it is well studied and does not require input of external power, the Janus active particle system is a good candidate to explore how active motion can affect different rheological properties, such as linear viscoelasticity and yielding. Well-established systems, like DLCA gels, are also themselves a good model system to investigate the rheological implications of active matter. Szakasits et al. embedded active particles in DLCA gels to explore the implications of activity on the microdynamics and linear viscoelasticity of colloidal gels [20], [125]. Their experiments found an increase in microdynamics and a decrease in viscoelastic moduli with increasing activity level. In these papers, activity level was controlled through the number of active particles embedded in the gel and the amount of active energy input to each particle via the concentration of the hydrogen peroxide reactant. They explain these findings with two interrelated theoretical approaches: 1) increased microdynamics result from the effect of active energy on direct and indirect vibratory strain fields on the gel network and 2) decreased moduli result from the effect of active energy on the pair bond spring constant [20], [125].

Omar et al. performed a comprehensive examination by simulation of an active gel system similar to that of Szakasits et al. They found that a variety of microstructures can result within a parameter space specified by the level of active and thermal energy relative to the energy of inter-particle interactions. In fact, at higher active energies they found that activity can drastically change and even destroy the structure of colloidal gels [70].

These prior experimental and computational studies have focused on the effect of active energy on gel microstructure and linear rheology. The next question to ask is how non-linear rheological properties vary; this question has yet to receive attention. Consequently, here we address the extent to which activity affects the non-linear rheology and yield stress of colloidal gels. Specifically, we address the following research questions: How does activity mediate the yielding process? Does the yielding behavior help elucidate the mechanism by which activity affects rheological properties? What additional theoretical development is needed to model the yield stress properties of active gels?

In this paper, we explore the non-linear rheology of yielding in fractal cluster gels embedded with active Janus colloids, referred to as active gels, and compare these properties to fractal colloidal gels without active Janus colloids, referred to as passive gels. We characterize yielding by means of three rheological tests: start-up of steady shear at a constant strain rate, large-amplitude strain sweep in oscillatory shear, and creep. We also report auxiliary measurements of the active gel microstructure and microdynamics. We find that all three non-linear rheological tests show a reduction in yield stress with increasing levels of activity. The yield stress reduction is found to be proportional to the reduction in the linear elastic modulus, G'; the effect of activity on the yield strain of gels is not significant. To model the results, we hypothesize that individual Janus colloids activate whole fractal clusters in which they are embedded. The degree of change in the microdynamics, linear elastic modulus, and yield stress are all consistent with a description in which active clusters lead to an increase in the effective temperature of the system that subsequently softens the inter-particle bond spring constants. The activation of fractal clusters by active Janus colloids explains why so few active particles generate such large rheological changes of the gels.

2.3 Experimental Methods

2.3.1 Colloidal and Janus Particles

Monodisperse dyed and undyed polystyrene (PS) colloids are used in this study. Confocal experiments use red (580/605) fluorescent carboxylate-modified PS microspheres purchased from Thermo Fisher Scientific (F8821 lot 2096781, diameter $d = 2a = 1.0 \pm 0.04$ μm, density $\rho = 1.055$ g/mL, zeta potential = -54.3 $\pm$ 3.4 mV). Rheology experiments use undyed carboxyl PS microspheres purchase from Thermo Fisher Scientific (C37274 lots 2124342 and 2145544, diameter $d = 2a = 1.0 \pm 0.05$ μm, density $\rho = 1.055$ g/mL, zeta potentials = -49.8 ± 3 and -61.0 mV, respectively).

Janus colloids used in this study are made by spin coating a monolayer of the fluorescent PS colloids (F8821 lot 2096781, Thermo Fisher Scientific) onto a cleaned glass slide and depositing 10 nm of platinum onto one side of the particle through physical vapor deposition (Enerjet Evaporator). These particles are then recovered from the slide and suspended in 18.2 MΩ Millipore water until used. Three different batches of Janus particles were used in this study. Due to inherent batch-to-batch variability in the catalytically driven active motion, these batches are tracked and identified as B1, B2, and B3 in the data sets.

2.3.2 Preparation of colloidal gels

Each gel consists of 2.9% v/v of PS particles and, in the active gels, an additional 0.0030% v/v of Janus particles. This results in a gel with an active to passive particle ratio of $N_A:N_P = 1:1200$. The gel is prepared by first washing the particles three times and then suspending them in a density-matched mixture of H_2O (49.5%), D_2O (purchased from Sigma Aldrich, 45.5%), and antifoam chemical (Xiameter 1410, Dow Chemical, density = 1 g/cm^3,

0.5%). The antifoam compound was earlier reported to suppress the formation of oxygen bubbles from the decomposition of H_2O_2 [20]. Activity of the Janus colloids is initiated by the addition of hydrogen peroxide (H_2O_2) (30 wt% H_2O_2 in water, purchased from Sigma Aldrich). A diluted hydrogen peroxide solution was added and vortex mixed into suspension just before the addition of $MgCl_2$ (final concentration of 64mM), a divalent salt that causes slow aggregation and gelation at the specified concentration [37], [126]. The final concentrations of H_2O_2 in the gels were 0.025 wt%, 0.05 wt%, 0.1 wt%, 0.15 wt%, 0.2 wt%, or 0.25 wt%. Passive gels, used as controls, included H_2O_2 but lacked Janus particles. This control formulation accommodates the previously reported fact that the addition of hydrogen peroxide stiffens the colloidal gel network, most likely through its effect on the pair potential interaction between colloids [125].

2.3.3 Microstructural characterization of gels

To image the 3D structure of the gels, an inverted confocal laser-scanning microscope (Nikon A1Rsi equipped with NA = 1.4, 100x objective) is used. Particles used for these experiments were fluorescently labeled. We performed limited imaging experiments to confirm that the fluorescence does not affect the final gel structure. After the addition of the $MgCl_2$ solution, the suspension is vortex mixed for homogeneity and immediately loaded into an 8-well chamber (purchased from Thermo Fisher Scientific) mounted on the microscope. The gels are allowed to quiescently form for 1800 s before imaging. This protocol matches the timing of the rheological testing. Following this gelation time, 3D image stacks comprised of ~200 slices are acquired beginning at the coverslip. Two channels are imaged: the platinum layer is imaged in reflection mode with a 488 nm laser and the fluorescent PS of the colloidal volume is imaged with a 561 nm excitation and an emission band extending from 570 to 620 nm. The pixel size and stack spacing

are 83 nm and the image size is 512 x 512 pixels. The particle locations in the resulting image stack are determined using Trackpy [127].

The radial distribution function, g(r), of the gel, is computed from the colloidal positions, using tools available in the Freud Python library [128]. g(r) describes the average number of particles at a distance r from a basis particle, relative to that of an ideal gas. The gels produced here have been modeled as fractal clusters of fractal dimension, d_f, and cluster size, R_c. For the fractal regime of this structure, $g(r) \sim r^{d_f-3}$ [129], [130]. Following this equation, the slope of the log-log plot of the g(r) data is used to calculate the fractal dimension. For r/d > 3 [129], we observe power law scaling and extract the d_f. The average cluster size is then computed using equation (2-1)

$$R_c = a\Phi_o^{-1/(3-d_f)} \qquad (2\text{-}1)$$

where a is the particle radius [35]. The extracted values for d_f and R_c are used to compare the microstructures of the different gels.

To check for the possibility that the active colloids produce micro-bubbles due to platinum catalyzed H_2O_2 decomposition we used confocal microscopy; this method can detect bubbles not visible to the eye. This check involves placing the gel in a sealed 8-well plate immediately after gelation is initiated and observing it on the confocal microscope (40x objective, NA = 0.95) for the duration of the longest rheology experiment (4500 seconds). We continuously scan the well in a spiral pattern and capture images at 0, 300, 900, 1800, 3600, and 4500 seconds. As shown in Figure 2-12 we find that active gels with 0.3 wt% H_2O_2 produced micro-bubbles at 1800 seconds or earlier; gels with 0.25 wt% H_2O_2 added showed no micro-bubbles for the duration of the 4500-

second experiment. For this reason, 0.25% H_2O_2 is the maximum concentration of H_2O_2 used in this study.

2.3.4 Microdynamical comparison of colloidal gel networks

The same particles used for microstructural characterization were used for microdynamical comparison. To confirm the microdynamical difference between passive and active colloidal gel networks as previously reported by Szakasits et al., the same inverted confocal laser-scanning microscope (Nikon A1Rsi equipped with NA = 1.4, 100x objective) is used. Passive and active gels are prepared as for the microstructural characterization and again allowed to quiescently form for 1800 seconds before imaging. Following this gelation time, 30 second videos are taken of the colloidal gels at a rate of 15 frames per second and at a height of approximately 10 μm above the coverslip. The same reflective and fluorescent channels are used to capture the platinum and PS, respectively, in the system. The pixel size is 83 nm and the image size is 512 x 512 pixels. A Python implementation of the Crocker and Grier algorithm known as Trackpy [127] is then used to extract the mean squared displacement, $<\Delta r^2(\Delta t)>$, of the passive and active gels where Δt is the lag time The static error from this method (about 9 x 10^{-4} μm^2), is taken from an earlier study. [125] This error is always at least 3 times less than the measured dynamics, an indication that the $<\Delta r^2(\Delta t)>$ of the gels is resolvable by the imaging system. We use the function $\varepsilon(\Delta t) = < \Delta r^2(\Delta t) >_{active} / < \Delta r^2(\Delta t) >_{passive}$ to describe the enhanced dynamics due to activity. Data are reported until the measured standard deviation of the mean squared displacement exceeds its average value.

2.3.5 Active energy determination by measurement of free particle dynamics

Because the activity of the Janus colloids varies with batch and [H_2O_2], we specify conditions of each experiment by means of the Janus particle active energy, as determined from a direct measurement of the active, free particle dynamics. Active colloids undergo random walks that are expanded relative to passive colloids moving under Brownian motion. These active dynamics occur because the transformation of chemical energy drives locomotion. We determine the active energy of a particle, E_A, at a given hydrogen peroxide concentration from its particle velocity by following Takatori et al. [131]. Specifically, we use $E_A = \xi V l$ where ξ is the hydrodynamic drag coefficient, V is the active particle velocity, and l is the active particle run length which is equivalent to $l = \tau_R V = (8\pi\eta a^3/k_B T)V$ where, η is the solution viscosity. E_A can be scaled relative to energy of passive particles, $E_p = k_B T$, the thermal energy that drives Brownian motion [131]. Here, T = 298 K. These quantities are those of the free particle, as measured at dilute solution conditions.

To measure the active particle velocity needed to assign E_A, dilute Janus colloids are imaged (Nikon A1Rsi, NA = 1.4, 100x objective) and tracked using a Python implementation of the Crocker and Grier algorithm known as Trackpy [127]. Videos, each containing approximately 5-15 Janus colloids, are collected at a rate of 30 fps at 9 locations spaced 200 μm apart in the shape of a cross. The pixel size is 124 nm and the image size is 256 x 512 pixels. The mean squared displacement, $\langle \Delta r^2(\Delta t) \rangle$, is used to characterize the particle velocities, V, by fitting the data to the function $\langle \Delta r^2(\Delta t) \rangle = 4D\Delta t + V^2\Delta t^2$ and limiting the set of data analyzed to short times, as appropriate for this expression [16], [125]. Here, D is the diffusion coefficient, $D = k_B T/(6\pi\eta a)$. Then, using the previously described equation, we compute the active energy, E_A, at each H_2O_2 concentration for batches B1, B2, and B3. For the range of H_2O_2 concentrations added, the free particle active energy ranges from $1.2k_BT$ – $25k_BT$. See

Supplementary material (Section 2.6) Figure 2-13 for all the resulting free particle active energies. For the rest of the paper, we index the active gels as per the free particle active energy of the embedded Janus colloid, so as to allow comparison across different batches and H_2O_2 concentrations.

2.3.6 Rheological characterization of gels

Rheology experiments were performed using undyed PS particles. Oscillatory and steady-shear rheology is performed on a stress-controlled rheometer (Anton Paar MCR 702) at T = 20°C with a 50 mm parallel plate geometry and Peltier temperature-controlled plate and hood. Poly(dimethylsiloxane) (PDMS) films of thickness ~1.5 mm are applied to both of the stainless-steel plates of the rheometer as described in Szakasits et al. [20]. These films suppress oxygen bubble formation that would interfere with the rheological experiments. Specifically, PDMS films are oxygen permeable [132]–[134] and are found to prevent oxygen bubble formation; they are used to act as a sink for oxygen. Stainless steel plates modified with these PDMS films accurately measure the rheology of both standards and gels (See Figure 2-14) [20]. Immediately after adding salt for gelation and vortex mixing for homogeneity, the colloidal suspension is loaded onto the rheometer. The parallel plate fixture is lowered to the gap distance (h = 500 μm) while rotating at ω = 3 rad/s to ensure even spreading of the sample.

We measure time-, frequency-, and strain-dependent viscoelastic moduli at h = 300, 500, and 750 μm and observed that the results at the two larger gaps are comparable, but the moduli at 300 μm gap were lower than the larger gaps (Figure 2-15). We therefore use h = 500 μm for all measurements. To reduce evaporation of the gel sample during experiments a solvent trap is used.

Before probing the yield behavior, a linear oscillatory deformation (γ_0 = 0.003 and ω = 1 rad/s) is performed for 1800 s. This prior measurement is used to probe the kinetics of gelation

and confirm its successful completion. After this linear measurement, the yielding behavior of the gels is characterized in three ways:

1) Start-up of steady shear ($\dot{\gamma}$= 0.02 s^{-1}) was performed for 1800 s to produce a load curve, i.e. the average stress as a function of strain; the peak stress was taken as the yield stress [41], [105] The particular shear rate of the measurement was chosen to allow better temporal resolution of the initial kinetic response while also ensuring that measured stresses were at least 2 times the instrument's lower stress limits, which was determined to be 2.9 x 10^{-3} Pa by measurement of standards (Figure 2-16). Visible signs of flocculation (as shown, for example, in the Figure 2-17: The passive colloidal gel was initially visually homogeneous at t = 0 sec during a steady shear experiment ($\dot{\gamma} = 0.02\, rad/sec$) with a 43mm glass plate. At 130 seconds into the experiment, the beginning of flocculation is visible along the edges of the fixture. By the end of a 2400 second experiment, the sample is fully comprised of flocculated roll cells. Because of this visible flocculation, only data for t < 60s is analyzed.) were first seen 120 seconds after the experiment was initiated. For this reason, we report data acquired up until 60 seconds.

2) Oscillatory strain amplitude sweeps (ω = 1 rad/s) were performed from γ_0 = 0.001 to 10. The yield stress is then the peak stress in the measured elastic stress curve [108], [109]. The specified frequency was chosen to avoid noise, which was observed at lower frequencies, and expulsion of the sample from the gap, which was observed at higher frequencies. The yield stress values obtained are at least two times the lower limit of torque resolution for the instrument, as determined in an earlier study by measurement of the linear viscoelastic moduli of aqueous solutions of poly(ethylene oxide) [20]. In addition, the yield stress estimated from the elastic stress method was checked by comparing results to those of the alternate method of the stress at which G' and G'' crossover (c.f. 2.6.1) [108], [109].

3) The creep compliance, J(t, σ) was measured at a number of values of the imposed stress (σ = 0.0001 to 0.1 Pa). For a yield stress material, at low imposed stress, the linear response is probed; the compliance approaches a nearly constant value in this case, consistent with a material with properties approaching that of an elastic solid. As the imposed stress is increased, the plateau compliance increases, until, above the yield stress, the compliance no longer attains a plateau value. It instead grows steadily, approaching a linear increase with strain at high imposed stress [108]. The yield stress is the imposed stress at which the material transitions from exhibiting a plateau to a steadily growing compliance.

2.4 Results and Discussion

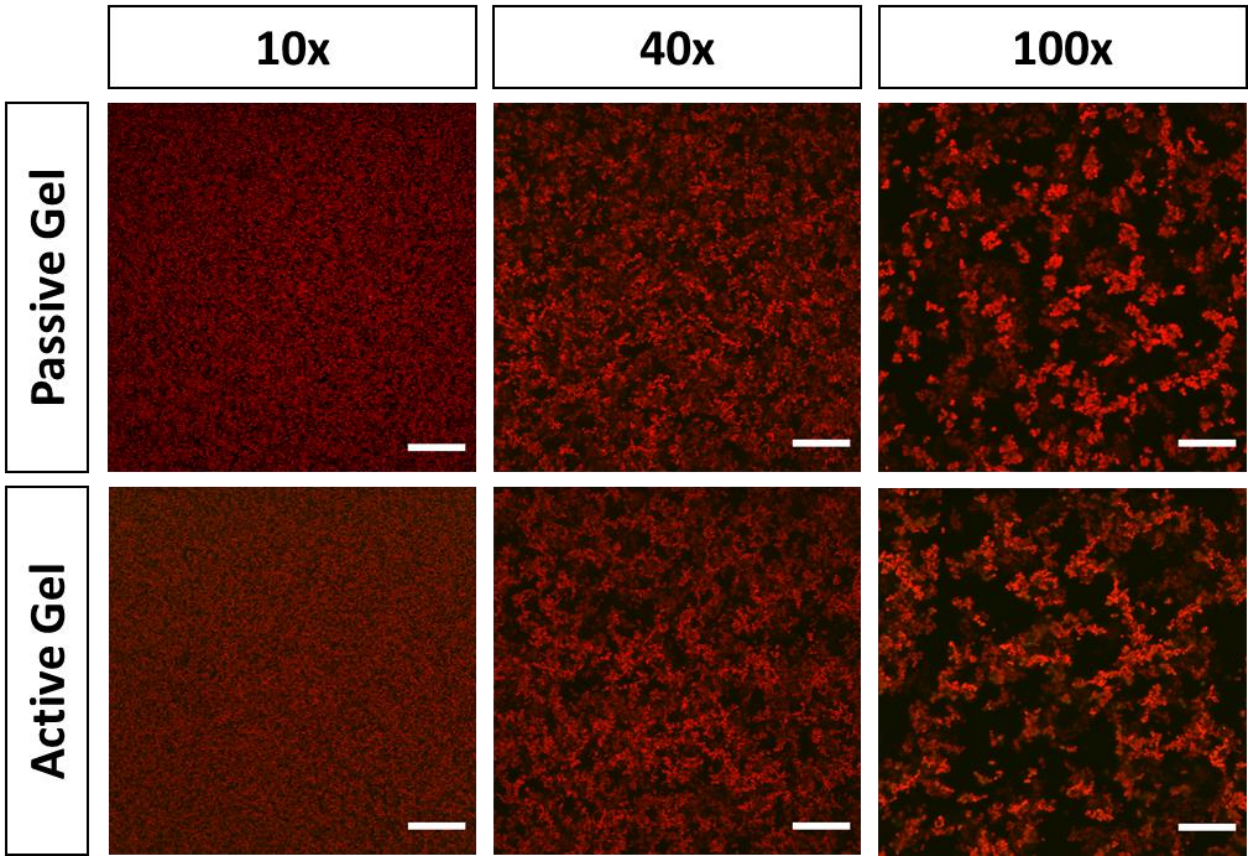

Figure 2-1: Visualization of active and passive gel ($\phi_o = 0.029$) 3D structures across multiple length scales imaged 1800 s after initial gelation. Scale bar of the 10x objective is 200μm; 40x objective is 50μm; 100x objective is 20μm. Active gels have an active to passive particle ratio of 1:1200 and contain Janus particles from batch B1 and 0.25 wt% H_2O_2 producing an $E_A/k_BT = 25$.

Figure 2-1 shows maximum projections of 3D volumes of passive and active gels 1800 seconds after initiation of gelation imaged with the 10x, 40x, and 100x objectives of the CLSM. The active gels in Figure 2-1 contain active colloids whose free particle active energy is $E_A/k_BT = 25$. The fractal structure of the gel is apparent, especially at 100x magnification. As the magnification decreases, the fractal structure on smaller scales gives way to structure that is more uniform and fluid-like, consistent with the larger, cluster scale of the gel [135].

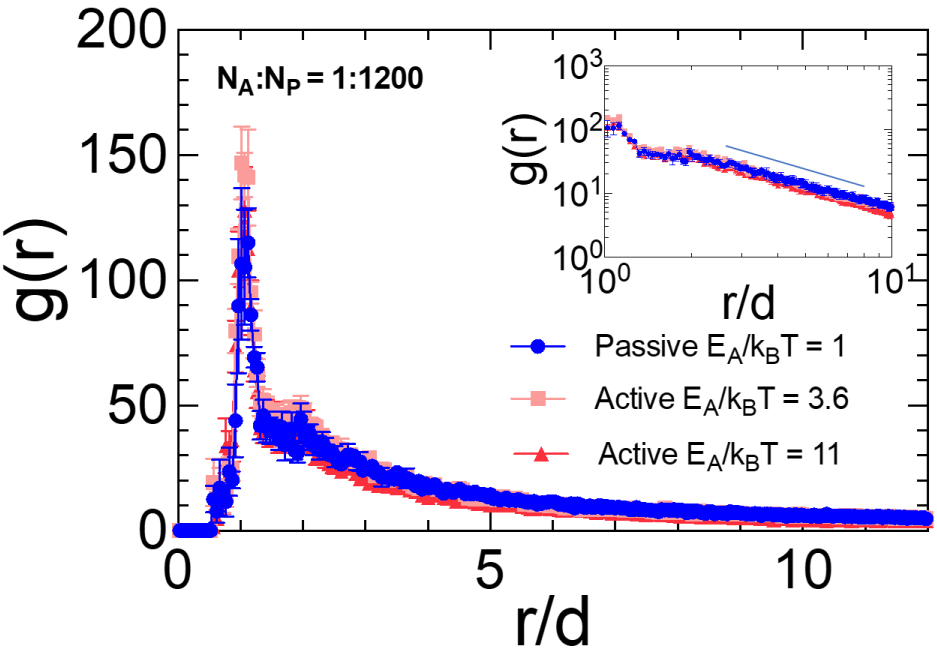

Figure 2-2: The radial distribution functions of passive and active gels. The inset shows the fractal scaling. Active gels at $E_A/k_BT = 3.6$ and $E_A/k_BT = 11$ contain Janus particles from batch B1 and 0.1 wt% and 0.2 wt% H_2O_2, respectively.

To characterize and compare the structures, the radial distribution function g(r), shown in Figure 2-2, is used to calculate the fractal dimension, d_f, and the average cluster size, R_c (see Methods) [35], [125], [129], [130]. The inset shows the regime from which these structural parameters were calculated, as per the methods. The passive gel has a fractal dimension, d_f, of 1.85 ± 0.06 and an average cluster size, R_c, of $11.1 \pm 1.8\ \mu m$. The active gels have a d_f of 1.84 ± 0.11 and 1.78 ± 0.08 and a R_c of 10.8 ± 3.0 and $9.30 \pm 1.5\ \mu m$ for gels containing active particles

with active energy ratios of E_A/k_BT = 3.6 and 11, respectively. These parameters for the active gels are compared to those of the passive gels by using 2-sample t-tests. The difference between the active and passive gel fractal dimension and cluster size is not statistically significant at either level of active energy tested. (For E_A/k_BT = 3.6, p = 0.84 and p = 0.83 for d_f and R_c, respectively. For E_A/k_BT = 11, p = 0.11 and p = 0.11 for d_f and R_c, respectively.) This indicates that activity does not cause a detectable change in the average gel microstructure in the activity regime we probe in this study. Additionally, all three fractal dimensions are consistent with diffusion-limited cluster aggregation for which d_f~ 1.8 [20], [23], [43], [125], [136], [137].

The similarity in the network structure of active and passive gels can be explained by means of the simulation results of Omar et al. [70]. This study reports the microstructure of colloidal gels formed by a system of attractive passive particles in the presence of a small fraction of active particles. The strength of pair interactions is defined by an attractive force as E^a/σ, where E^a is the well depth of the attractive pair potential and σ is the interaction range. The authors find that if the swim Peclet number of the active particles, $Pe_s = \xi V/(k_BT/a)$, is less than a critical value, then an active particle is unable to disrupt bonded particle pairs in the gel. Pe_s determines the ratio of active forces to thermal forces. The critical value, Pe_s^*, specifies conditions where the active forces equal pair attractions. Below Pe_s^* active particles do not change the gel microstructure vis-à-vis a gel formed from passive particles alone. To compare to Omar et al., we compute the ratio Pe_s/Pe_s^* for the samples reported in Figure 3-1.

Interaction between colloidal particles in the gel is described by a pairwise potential, $U(s)$, defined here as the sum of van der Waal's attraction, $U_{vdw}(s)$ and the electrostatic repulsion, $U_{el}(s)$ where, s is the surface-to-surface separation between particles [20]. A plot of the $U(s)$ normalized by thermal energy, k_BT, for the particles with properties described in Methods (Figure 2-18:

Pairwise potentials, Uel(s) (electrostatic repulsion), Uvdw(s) (van der Waal's attraction) and U(s) = Uel + Uvdw as a function of the interparticle separation s normalized by the thermal energy kBT. The horizontal dotted line indicates the well depth, Ea. The horizontal dot-dashed line is drawn at U(s)/kBT = -1. The interaction range, where U(s)/kBT ≤ -1, is σ = 0.13a, where a is the particle radius. Here, T = 298K.) along with complete expressions for the pair potential are provided in the SI. The magnitude of the well depth for this particle system is E_A = 22.5 k_BT and the interaction range where U(*s*)/k_BT ≤ -1 is σ = 0.13a. Together, $Pe_s^* \sim 2 \times 10^2$. From the microdynamical study of single active particle velocities (c.f. Figure 2-13: Microdynamics and energy of free active particles. a) mean squared displacements of active particles from batches 1 and 2 at each hydrogen peroxide concentration. Each condition contains at least 7 measurements. Error bars are standard error of the mean. b) Summary of the particle velocity (V), run length (l), and active energy (EA) at each hydrogen peroxide concentration computed for each condition. Calculations were performed as described in the text. The velocity was calculated by fitting the short time mean squared displacements to the limiting expression, $\langle \Delta r^2(\Delta t) \rangle = 4D\Delta t + V^2\Delta t^2$, described by Howse et al. [16]. Run length was calculated using the velocity extracted from short-time mean squared displacements and the reorientation time computed from the rotational diffusivity as per theory [16]. Errors are standard errors of the fit. Active energies were calculated using per Takatori et al. as described in the text [131]. Additionally, kBT = 4.04e-21 m2kg/(s2K).), we find that for all concentrations of H_2O_2 studied here, $Pe_s / Pe_s^* \sim 5 \times 10^{-3}$ - $3 \times 10^{-2} << 1$. The comparison supports the Figure 3-1 observation of no structural change due to the inclusion of active particles in the gels.

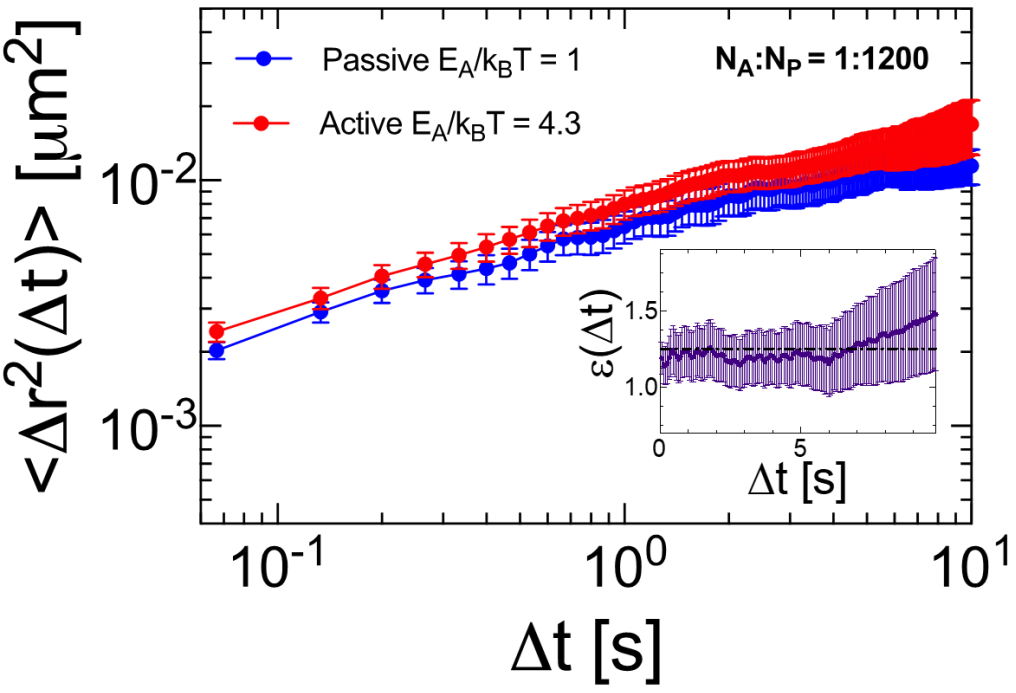

Figure 2-3: Mean squared displacement ($<\Delta r^2(\Delta t)>$) of passive gels and active gels 1800 s after initial gelation. Active gels contain Janus particles from batch B3 and 0.2 wt% H_2O_2. The inset shows $\varepsilon(\Delta t)$ vs lag time. The line indicates the average enhancement across the set of lag times reported. Error bars are standard error of the mean.

To quantify the microdynamical difference between passive and active gels, the ensemble-averaged mean square displacements of particles in the gels were characterized. Figure 2-3 shows these $<\Delta r^2(t)>$ of passive and active gels (the latter containing particles with $E_A/k_BT = 4.3$). The magnitude of $<\Delta r^2(t)>$ is more than two times greater than the static error (as taken from prior work by Szakasits et al.) at all conditions, confirming that the measured active and passive displacements are resolvable. Defining $\varepsilon(\Delta t)$ as the active to passive $<\Delta r^2(t)>$ ratio as per the methods, we see that when plotted against the lag time (inset of Figure 3-3) the microdynamics of active gels are, on average, 25% greater than that of the passive gels across the range of the data set. This level of dynamical enhancement is comparable to that previously reported by Szakasits et al for gels of a somewhat lower volume fraction. The $<\Delta r^2(\Delta t)>$ curves for both passive and active gels show small positive slopes on a log-log scale, suggesting that there is some slow

dynamics of the gels, in addition to localization dynamics. Similar observations have been previously reported for colloidal gels. This time dependence could be the result of slow dynamics, arrested phase separation, or syneresis [125], [138], [139].

2.4.1 Passive gel rheological characterization

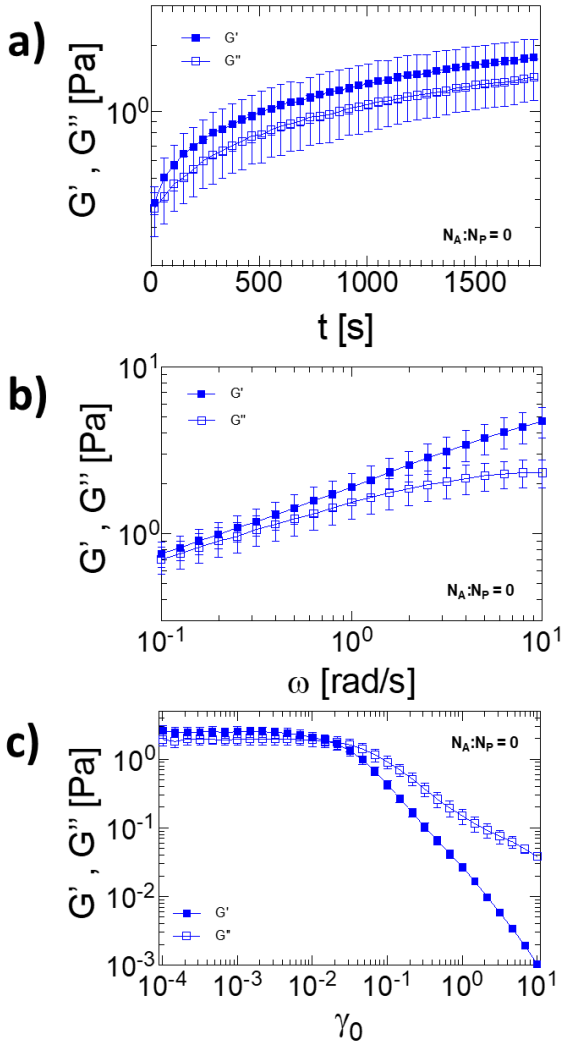

Figure 2-4: Passive gel (E_A/k_BT = 1) storage and loss moduli (G', G'') as a function of a) time at γ_0 = 0.003 and ω = 1 rad/s; b) ω at γ_0= 0.003 and time = 1800 s; and c) γ_0 at ω = 1 rad/s and time = 3300 s. Error bars are standard error of the mean.

Figure 2-4 plots the linear viscoelastic moduli as a function of (a) time, (b) frequency, and (c) strain for a colloidal gel made solely of passive particles. The volume fraction of passive

particles in the gel is 2.9%. At ω = 1 rad/s and γ_0 = 0.003 (Figure 2-4(a)) the time-dependent moduli show an initial rapid increase, consistent with the onset of gelation. For t > 500 s, the moduli continue to increase, but at a much-reduced rate. At 1800 s, G' = 1.8 ± 0.4 Pa and G'' = 1.4 ± 0.3 Pa. Aging is a common feature of colloidal gels; however, our experiments are completed in a short enough time (t = 3600 – 4500 seconds) that aging does not strongly affect the conclusions drawn from the measured viscoelastic moduli [139], [140]. Specifically, all measurements reported in this paper are captured within the bounds of 1800 s to 3000 s after gelation. When the non-linear deformation is initiated at 1800s yielding occurs quickly; in startup tests it takes ~20 seconds; in oscillatory strain tests it takes ~660 seconds; and in creep tests it takes ~1 second to see the onset of yielding at the particular stress probed. Extrapolating from the aging rate of 5.3 x 10^{-4} Pa s^{-1} determined over the interval 1300 s to 1800s in Figure 3-4a, we estimate that the passive gel moduli change by 0.07%, 20%, and 0.03% over the period of each measurement, respectively. Though the estimated gel moduli for the oscillatory strain tests is significant, we note that the test is still a useful tool for comparing yielding behaviors. Additionally, since the aging should occur in both passive and active gels and the effect of aging is in the opposite trend that is expected of activity, the results allow conclusions to be drawn about the effects of activity.

The frequency dependence of the linear viscoelastic moduli (c.f. Figure 2-4 (b)) displays power law behavior that is indicative of a gel past its gel point [141]. The strain amplitude sweep (c.f. Figure 2-4 (c)) shows an onset of nonlinearity at γ_0 ~ 0.01; the strain chosen for the time sweeps, γ_0 = 0.003, is therefore within the linear regime.

2.4.2 Yield stress determined from start-up of steady shear flow

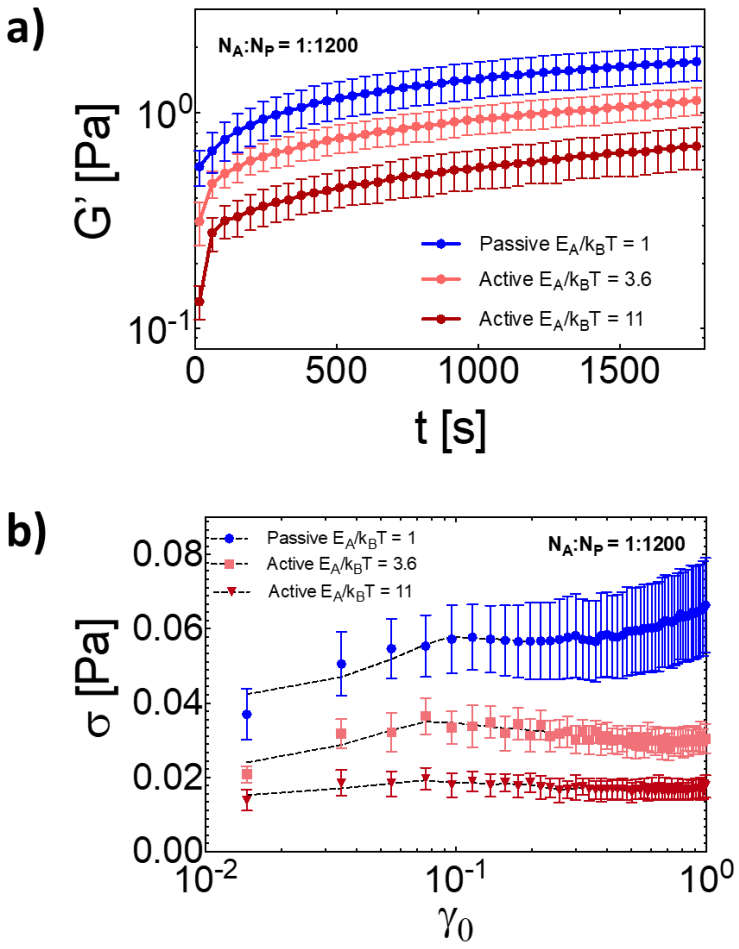

Figure 2-5: Elastic moduli and stress with increasing active energy ratios. (a) Elastic moduli as a function of time (γ_0 = 0.003, ω = 1 rad/s) and (b) subsequent start-up of steady shear flow at a $\dot{\gamma}$ = 0.02 s^{-1} of passive and active gels with increasing hydrogen peroxide concentration. Active gels contain Janus particles from batch B1 and 0.1 wt% and 0.2 wt% H_2O_2, respectively. The initial peak stress value in the curve of b) is taken as the yield stress of the gel. Error bars are standard error of the mean. For clarity of presentation, only two of the seven active gel data sets are plotted; the complete data set is available in Figure 2-19 and Figure 2-19 in the supplementary material.

When active particles are embedded in the gel, the linear viscoelastic response drops significantly, consistent with Szakasits et al. [20]. Figure 2-5 (a) shows these results – specifically G'(t) for passive and active gels. The linear elastic modulus decreases monotonically with increasing activity of the embedded active particles. (See Figure 2-19 in the supplementary material for full data set.) This trend confirms that activity generates change in linear rheological properties.

Following the test in Figure 2-5 (a), the stress response of passive and active gels in startup of steady shear flow is measured. The measured stress is plotted as a function of strain in Figure 2-5 (b); the shear rate of the flow is 0.02 rad/s. At each condition studied the stress initially grows to a maximum value. This maximum occurs by $\gamma_0 \sim 0.1$. After the maximum, the stress decays within less than a unit of strain. As the experiment concludes the stress is once again increasing. The first peak in the stress is taken as the yield stress, consistent with literature. [41] Following this definition, the yield stress for passive gels is 0.058 ± 0.021 Pa while that of active gels here with 0.1 wt% and 0.2 wt% H_2O_2 is 0.038 ± 0.005 Pa and 0.020 ± 0.003 Pa, respectively. As is evident, the yield stress also decreases monotonically with increasing activity (see Figure 2-20 in supplementary material for full data set). The stress peaks from the start-up of steady shear tests do not show as sharp of drops compared to similar tests found in literature. For example, the peaks that Mohraz and Solomon report for similar tests on low volume fraction colloidal gels drop at least 60% after one unit of strain, while the 2.9 vol% gels here drop between 1 and 10% before rising again. [41]

This minimal drop in stress is taken to be a result of shear induced flocculation, a phenomenon common in particle suspensions and dispersions that occurs at low shear rates and is affected by hydrodynamic interactions [142], [143]. Once the sample is yielded, the test occurs at conditions favorable for shear-induced flocculation. Specifically, it contains attractive particles in a Newtonian fluid and it is sheared in a confined geometry at low shear rates. The upturn in the stress suggests a build-up of structure. This is visually confirmed by extending the steady shear test for passive gels to longer times and observing the specimen through a glass plate (43 mm diameter). Figure 2-17 in the supplementary material shows these tests; an initially homogenous gel changes, over time, to a series of flocculated roll cells that are visible to the naked eye. These

flocs are strikingly similar to the shear-induced flocs reported in literature [142], [143]. (Recall that active gel rheology data is only reported up to 60 seconds, which is a regime prior to when the initial flocs are first observed at 120 seconds.)

Swan et al. explain that shear-induced flocculation occurs when the shearing of a homogenous suspension causes aggregates to form, as would take place in the breaking and restructuring during the yielding process. These aggregates (or flocs) grow under continuous shear. The growth generates structure that produces additional stress that ultimately exceeds the stress of the initial, pre-yielded gel. [143] Thus, shear-induced flocculation is the likely explanation for the minimal drop in stress that is observed post-yield in these gels.

2.4.3 Dependence of Rheology on Active Energy

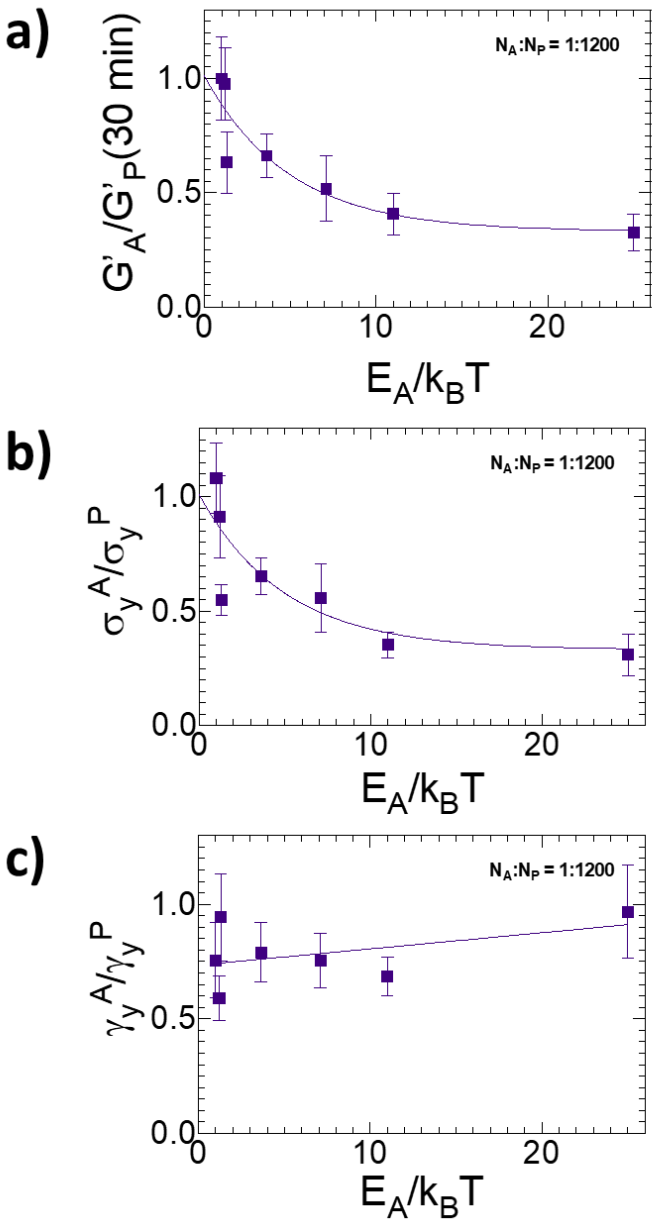

Figure 2-6: Yielding parameters from start-up of steady shear tests of active gels with increasing active energy. (a) Ratio of active to passive gel elastic moduli, characterized at t = 3000 s, (b) ratio of active to passive yield stress from start-up of steady shear, and (c) ratio of active to passive yield strains. The active energy of the embedded particles is normalized relative to k_BT. Lines in (a) and (b) are exponential decay fits intended to guide the eye. The line in (c) is a linear regression. The active gels in this figure contain 0.003% v/v of Janus particles from batch B1 with H_2O_2 concentrations 0.025%, 0.05%, 0.1%, 0.15%, 0.2%, and 0.25%. The passive gels contain no Janus particles and a H_2O_2 concentration of 0.5%. Additionally, $k_BT = 4.04 \times 10^{-21}$ J/K. Error bars are standard error of the mean.

Start-up of steady shear was performed at a total of 7 different concentrations of H_2O_2. The resulting elastic moduli, yield stress, and yield strain are plotted in Figure 2-6 as a function of the

scaled active energy normalized against the passive case. (The mapping between active energy, batch, and H_2O_2 concentration is reported in Figure 2-13 in the supplementary material.) The ordinate scales of G', σ_y, or γ_y are all scaled relative to the passive case.

As the active energy increases, there is a monotonic decrease in elastic modulus (Figure 2-6 (a)), as indicated by the trend line. (The data follow the trend line well except for the datum point at $E_a = 1.3k_BT$, which falls lower than the line, even when its error is considered. The error bars of all the other points, however, support the adoption of the trend line.) At the highest activity level, the elastic modulus is about 60% lower than the that of the passive gel. This reduction is less than that found in 1.5 vol% gels reported in Szakasits et al. This smaller reduction is consistent with the higher volume fraction of the gels studied here with network elasticity that is about 12-fold greater than that characterized by Szakasits et al. (see Equation (2-2) in the theory section). Achieving corresponding levels of material softening therefore requires higher active energy states, precluded here due to onset of bubble formation (see Figure 2-12 in supplementary material). Figure 2-6 (b) shows the dependence of the yield stress of the gel on active energy, which also shows a monotonic decrease. The decrease in yield stress is of a magnitude and trend that is comparable to the decrease in linear elastic modulus. (Consistent with the modulus data the point at $1.3k_BT$ is lower than the trend; however, the other points support the adoption of a trendline.)

The yield strain, or strain at which yielding occurs, is plotted in Figure 2-6 (c). It was determined as the strain of the peak stress in the start-up of steady shear experiments reported. This characterization approach is found in the literature [41]. Mohraz and Solomon suggest the yield strain determined in this way is associated with rupture of the fully extended gel backbone. It is distinguished from the limit of linearity, which is associated with strains leading to non-

harmonic changes in the pair interaction between particles. Distinguishing between these two measures is important when comparing yield behavior from different rheological tests.

A linear regression t-test was performed on these yield strains to determine if there was a statistically significant dependence on active energy. The p-value of 0.32 indicates no significant relationship. These trends in moduli, yield stress, and yield strain show that the reduction in yield stress is completely explained by the proportionate reduction in elastic modulus.

In their work, Mohraz and Solomon proposed that the critical strain of a fractal cluster colloidal gel is related to properties of its fractal clusters through the equation: $1 + 0.6\gamma_c \sim \phi^{(x-1)/(d_f-D)}$ where x is the backbone fractal dimension and D is the Euclidean dimension of the system. The critical strain they define is equivalent to the yield strain measured here. The observation that the critical strain is independent of activity suggests that neither x nor d_f are a function of this quantity. This finding supports the microscopic visualization from which it was concluded that that the colloidal gel microstructure is independent of the energy of the active particles embedded in the gel.

2.4.4 Yield stress from oscillatory shear rheology

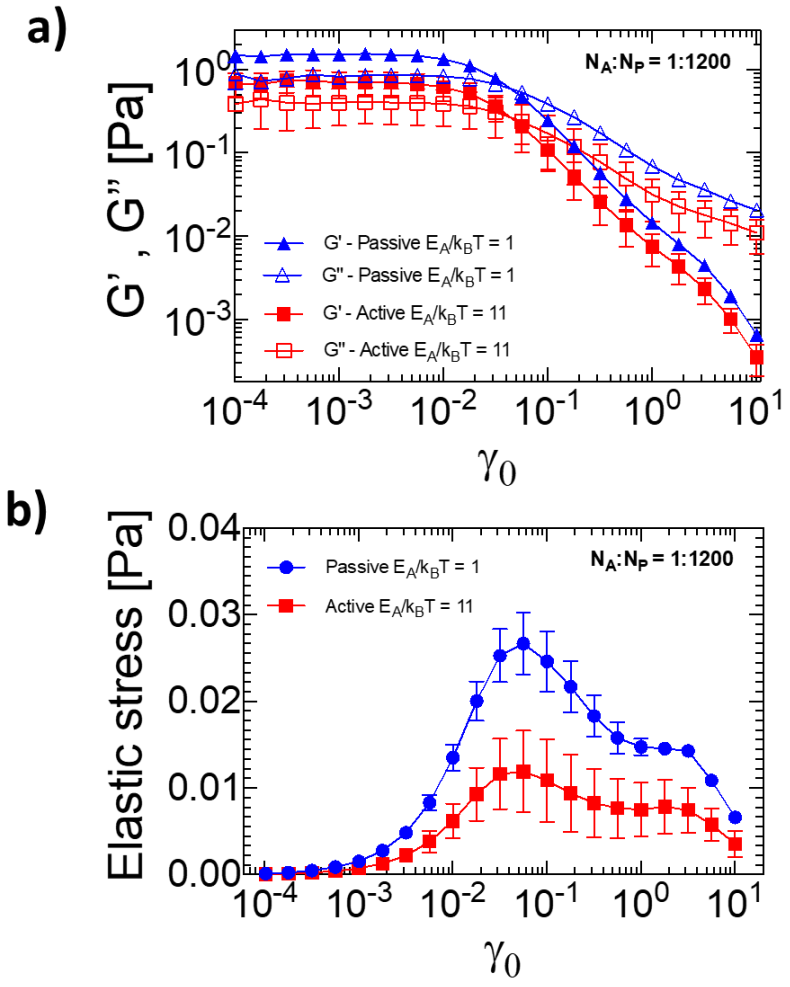

Figure 2-7: Yield behavior from oscillatory strain amplitude sweeps (ω = 1 rad/s and t = 1800 s) of passive and active gels (a) Viscoelastic moduli as a function of strain amplitude. (b) Elastic stress (G' γ_0) plotted as a function of strain amplitude. Active gels contain Janus particles from B1 and 0.2 wt% H_2O_2. The G'-G'' crossover point and the maximum in elastic stress curve are taken as the yield stress in each graph, respectively. Here $k_BT = 4.04 \times 10^{-21}$ J/K.*

Oscillatory strain amplitude sweeps also characterize the yield stress of the active gels. The initial linear elastic modulus is given in the supplementary material Figure 2-22 (a). Figure 2-7 (a) shows G' and G'' as a function of increasing strain amplitude at ω = 1 rad/s. The yield stress is determined from these data as the maximum in the elastic stress, as per the Methods section 2.3.6 [108], [109].

The elastic stress is the product of the elastic modulus G' and the strain amplitude. Figure 2-7 (b) plots the oscillatory shear data in this way. This analysis determines the yield stress to be 0.027 ± 0.004 Pa and 0.012 ± 0.005 Pa, for the passive and active gels, respectively. The yield

strain by this method is 0.051 ± 0.012 for passive gels and 0.038 ± 0.012 for active gels. A 2-sample T-test indicates that the difference in yield strain is not significant (p = 0.18). These results corroborate that activity is causing a drop in yield stress but no significant change in yield strain; it also supports the earlier conclusion that embedding the active Janus particles does not significantly affect the microstructure of the gels [41].

2.4.5 Yield stress from creep measurements

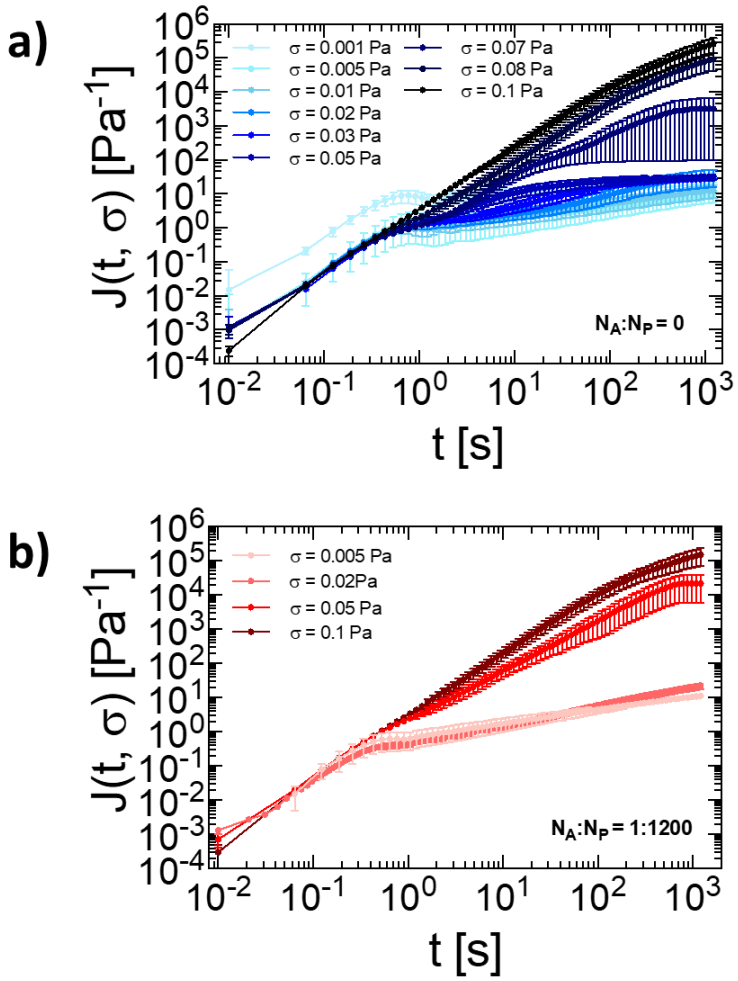

Figure 2-8: Creep compliance, J(t,σ) of (a) passive and (b) active gels beginning at 1800 s after initial gelation. Active gels contain Janus particles from batch B2 and 0.2 wt% H_2O_2 (E_A/k_BT = 5.6). Error bars are standard error of the mean.

Figure 2-8 compares the creep compliance of passive and active gels. After the initial linear elastic measurements (Figure 2-22 (b)), the gels were subjected to progressively greater stresses from 0.001 to 0.1 Pa. In Figure 3-8a, for the passive gel, as the stress is increased from 0.001 to 0.03 Pa, the compliance curves overlap and approach a constant value at long times. This stress independence in the regime 0.001 – 0.03 Pa is indicative of a linear response. For $t < 10^2$ s, representing the elasticity dominated region, this linear compliance relates to an elastic modulus of about 0.81 Pa (obtained by fitting to a single mode Jeffreys model, c.f. Figure 2-21) which is consistent with the linear G' measurements at an equivalent frequency of about $\omega \sim 0.1$ rad/s (Figure 2-4 (a)).

As the stress increases to 0.07 Pa, the compliance deviates from plateau behavior and instead grows monotonically with strain. At stresses of 0.08 and 0.1Pa, the compliance grows nearly linearly with strain. Recall that the yield stress is the imposed stress at which the material transitions from exhibiting a plateau to a steadily growing compliance. The data here shows such a transition between 0.05 and 0.07 Pa, an indication that the yield stress falls between these two values.

The active gel (containing particles with $E_A/k_BT = 5.6$) in Figure 2-8 (b) displays a similar progression from the behavior of a viscoelastic solid to that of a viscous liquid. However, there are quantitative differences; the creep compliance attains a constant, plateau value for stresses at and below 0.02 Pa. Deviation from the compliance plateau value begins at a lower stress of 0.05 Pa instead of 0.07 Pa and a linear response to strain is observed by 0.05 Pa. From this, we take the yield stress for the active gel to be between 0.02 and 0.05 Pa.

2.4.6 Comparison of yield stresses from the three rheological tests

Table 2-1: Summary of yield stresses of passive and active gels from the different rheological tests

	σ_y		
	Start-up of steady shear	**Oscillatory Strain Sweep (from elastic stress curve)**	**Creep**
Passive gel ($\frac{E_A}{k_BT} = 1$)	0.058 ± 0.020 Pa	0.027 ± 0.007 Pa	Between 0.05 and 0.07 Pa
Active gel ($\frac{E_A}{k_BT} = 5.6$)	---	---	Between 0.02 and 0.05 Pa
Active gel ($\frac{E_A}{k_BT} = 7.1$)	0.032 ± 0.009 Pa	---	---
Active gel ($\frac{E_A}{k_BT} = 11$)	0.020 ± 0.001 Pa	0.012 ± 0.009 Pa	---

Table 2-1 summarizes the apparent yield stresses of passive and active gels found from the three rheological tests. The creep and start-up of steady shear methods are in good agreement. The decrease in the yield stress by these characterization methods is approximately 35-50%. On the other hand, the apparent yield stress from the oscillatory strain sweep technique is much lower than the other two methods. Nevertheless, the relative decrease with activity is also about 50%.

The effect of technique on the value of the measured yield stress has been discussed in the literature [111], [112]. Here, all methods show a similar reduction in the magnitude of the yield stress as activity is introduced into the fractal cluster gels. All tests additionally show no significant change in yield strain, which we earlier discussed as consistent with the lack of a microstructural change. These results together indicate that it is the decrease in linear modulus that causes the concomitant drop in yield stress in this colloidal gel system.

We note that even though the yield strain is here found to be independent of activity, this finding may not be general. Specifically, as identified earlier, our system has a very low active particle ratio (1:1200) and Pe_s/Pe_s^* ratio ($\sim 5 \times 10^{-3}$ - 3×10^{-2}). In this low activity regime, the active swim forces do not exceed the attractive forces of the system. However, as per Omar et al.,

in a system containing swim forces greater than Pe_s^* and, therefore great enough to cause a structural change, the yield strain would depend on activity. This dependence would in turn affect the effect of activity on the yield stress.

2.4.7 Hypothesis to explain the activity-induced decrease in storage modulus

Since the activity-induced reduction of yield stress arises due to the concomitant decrease in modulus (Figure 2-6), we focus on modeling the activity-induced decrease in the storage modulus. As shown Figure 2-6a, the gel modulus decreases as the level of active energy input by the Janus particles is increased. The magnitude of the decrease – about 60% – is unexpected given the very low abundance of active particles embedded in the gel. The active to passive particle ratio in the gel is $N_A:N_P = 1:1200$. As free particles, these active colloids undergo locomotion at rates consistent with an active energy that is up to twenty-five times that of thermal energy. That is, $E_A = 25k_BT$, at its largest in the data set.

If the active energy of the Janus particles were to affect linear rheology in proportion to their number and their active energy [20], the modulus change, $\Delta G/G$, would be expected to scale as $\sim (N_AE_A + N_PE_P - k_BT)/(k_BT)$. Here N_A and N_P are the number fraction of active and passive particles, respectively. Although the active energy of each particle is high, their number density is low. The resulting decrease in modulus would be no more than about 2%. Therefore, some other physical mechanism is required to explain the much greater (up to 3x) decrease in elastic modulus that are observed.

To reconcile the modulus decrease, active particle concentration, and energy of the active particles, we hypothesize that a Janus particle activates the fractal cluster in which it is embedded. Enhanced fluctuations of active clusters – rather than active particles – then drive the decrease in rheological properties. Given the measured fractal dimension and size of the clusters, and if each

fractal cluster includes at most one active particle, the active to passive cluster ratio is 1:40 in the gels studied here. Before developing a quantitative model, we first review literature that is supportive of the conjecture that active particles could drive active fluctuations in the fractal clusters in which they are embedded.

The active cluster hypothesis is motivated by dilute solution studies in which Brownian clusters of passive colloids were observed to exhibit stronger than expected self-propulsive dynamics when an active particle was embedded in it [8], [80], [81], [144], [145] and by a study of fractal cluster gels which reported that passive colloids in the gels exhibited enhanced dynamics [125]. First, assemblies of one to six passive colloidal cargo transported by single catalytic [81] and light absorbing [145] active colloids moved with speeds up to 25% of that of the micro-motor. Second, passive clusters containing up to 19 particles attached to a light actuated self-propelled Janus colloid displayed enhanced velocities equal to up to 30% of that of the free active particle and higher than would have been observed under purely Brownian dynamics [8]. Third, recent measurements on fractal cluster gels – containing on average ~ 1000 particles per cluster – showed that embedded active particles cause enhanced displacement of passive colloids [125]. These studies bracket the size of the fractal clusters produced in this paper, which average about 300 particles. They support the conjecture that a Janus particle could activate a cluster in which it is embedded. We note that this activation might well be expected to proceed with some efficiency that is less than ideal. These studies suggests that clusters might be activated with an efficiency of 25-30% (i.e. $E_{A,c} = \chi E_A + (1 - \chi)k_BT$ were $\chi \sim 0.25\text{-}0.3$, where $E_{A,c}$ is the active energy of a cluster and χ is an efficiency).

We model the effect of active clusters on gel mechanics with the following: The elastic modulus of (passive) fractal cluster gels has been previously modeled as [35]:

$$G' = \kappa a^{-1} \phi^{(3+d_B)/(3-d_f)} \quad (2\text{-}2)$$

Where, κ, the spring constant is [20], [130]:

$$\kappa = \frac{k_B T}{\langle s^2 \rangle - \langle s \rangle^2} \quad (2\text{-}3)$$

Where the bracket indicates a Boltzmann-weighted average (c.f. SI) and d_B is the backbone bond dimension (~ 1.1 for DLCA gels [146]). Applying equations (2-2) and (2-3) for the passive gel ($T = 298$ K) gives G' = 1.5 ± 0.6 Pa. This value agrees well (p = 0.70) with the measured value in Figure 2-4a of 1.8 ± 0.4 Pa.

To apply equations 2 and 3 to active gels, T is replaced with an effective temperature, T_{eff}, whereby, $k_B T_{eff}$ is the total energy of the system including energy input by active clusters. From Szakasits et al. [20]:

$$k_B T_{eff} = N_{A,c} E_{A,c} + N_{P,c} E_{P,c} \quad (2\text{-}4)$$

Here, $N_{A,c}$, $N_{P,c}$ and $E_{A,c}$, $E_{P,c}$ are the number fractions and energies of the active and passive clusters, respectively. Each active cluster is assumed to contain one Janus particle embedded in it. Thus, $N_{A,c}$ is calculated as the ratio of number density of Janus colloids (c.f. Methods 2.3.2) to the number density of clusters in the gel. For fractal gels, the number density of clusters of size R_c containing particles of radius a is $\phi_0 R_c^{-d_f} a^{d_f-3}$, where ϕ_0 is the colloid volume fraction [147]. For the active gels studied here, $N_{A,c}$ = 0.024, $N_{P,c}$ = 0.976 and $E_{P,c} = k_B T$. The probability of having more than 1 active colloid per cluster is vanishingly small given the extremely dilute concentration of Janus colloids (1 : 1200) in the gel that results in an active to passive cluster ratio of just 1 : 40.

Finally, two limiting cases for $E_{A,c}$ can be identified based on the level to which clusters are activated: (1) $E_{A,c} = E_A$, for which the active cluster has the same energy as the embedded active particle and (2) $E_{A,c} = k_BT$, for which fluctuations of the active particle are fully damped, and the cluster remains passive. Intermediate values, $k_BT < E_{A,c} < E_A$, represent cases in which the active particle is only partially effective in activating the cluster [8]. Therefore, $E_{A,c} = \chi E_A + (1 - \chi)k_BT$ where, $\chi \in [0 , 1]$ is the degree of cluster activation. As discussed previously, literature references [8] and [81], [145] study might suggest that χ might be in the range 0.25-0.30.

The active clusters affect the elastic modulus in the following way: Increasing levels of activity (i.e. $E_{A,c}$) increase the system energy (equation (2-4)) and result in larger fluctuations in inter-particle separation. Equipartition then generates a decrease in the spring constant (equation 3), which finally results in a decreased elastic modulus (equation (2-2)).

The theory predicts a family of curves, each corresponding to a different degree of cluster activation efficiency, χ. These predictions are plotted in Figure 2-9 as the modulus ratio G'_A/G'_P calculated at each experimental condition of Janus particle active energy, E_A/k_BT. When, $\chi = 0$ ($E_{A,c} = k_BT$), no decrease in gel modulus is predicted. As the degree of cluster activation increases up to $\chi = 1$ ($E_{A,c} = E_A$), the curves progressively shift downwards indicating greater levels of decrease in G'.

The predictions are compared with experimental data and plotted as solid black circles with a trend line. The experimental line falls between the theoretical limits $\chi = 0$ and $\chi = 1$, implying that for the active gel, embedded Janus particles activate the clusters only partially. The best agreement between calculated and measured values, obtained from a regression analysis, is when $\chi = 0.29 \pm 0.04$.

The data point at $E_A/k_BT = 1.3$ (as discussed earlier) is somewhat confounding. In addition, the shape of the experimental curves differs somewhat from the family of model predictions. Specifically, the theory at high active energy predicts a greater drop in modulus than observed. There are a number of factors, each of which could be the subject of future research, which might explain the difference in trend. These factors are: (1) the gel may progressively stiffen upon the addition of H_2O_2 due to this chemical's effect on pair interactions [125]; (2) additional attractive forces between active-passive particles might be induced by local chemical gradients formed during fuel decomposition [148].

Notwithstanding these avenues for future research, Figure 2-9 indicates that the hypothesis of fractal clusters activated by embedded Janus particles is consistent with the reduction in rheological properties for these gels comprised of very few active colloids. The comparison suggests that the energy of active clusters is as great as 8.0 k_BT for the H_2O_2 concentrations studied here. These findings are consistent with prior studies that show fluctuations and motion of indirectly activated passive clusters are 25-30% of the embedded active colloids [8], [125].

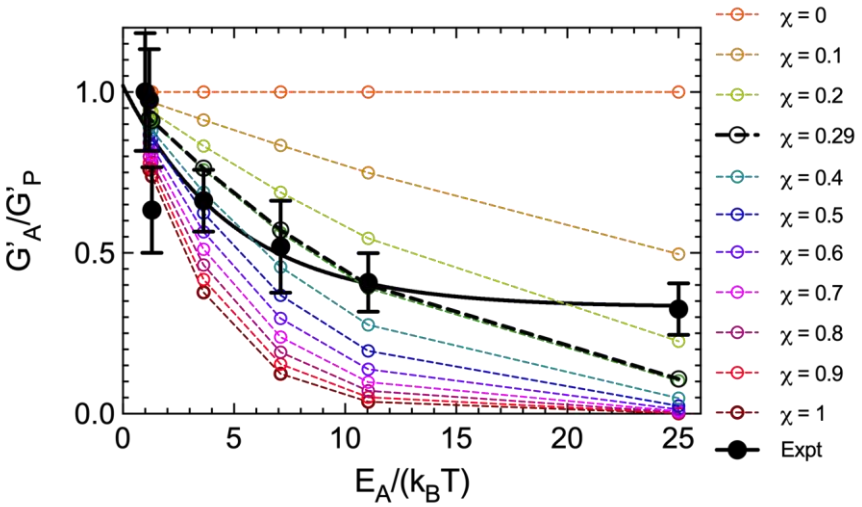

Figure 2-9: Variation of active to passive gel storage modulus with free particle active energy, E_A/k_BT. Experimental values from Figure 6a are plotted as filled circles with a solid trend line. Dashed lines indicate theory predictions calculated pointwise at each experimental condition for different levels of cluster activation from $\chi = 0$ ($E_{A,c} = k_BT$) to $\chi = 1$ ($E_{A,c} = E_A$). The best-fit line is plotted as the heavier dashed line. Generated by Mahesh Ganesan.

2.5 Conclusions

Through three commonly used rheological yield stress tests – steady, oscillatory and step shear – this study has shown that active motion causes a reduction in the yield stress that parallels the reduction in the linear viscoelastic moduli of colloidal gels embedded with active particles. This up to a factor of three reduction in yield stress was achieved at very low amounts of active particles embedded in the gel network. Simultaneously, these embedded particles generate no significant change in the yield strain. Rheological results combined with independent confocal measurements that show no significant change in fractal cluster microstructure of the gels, as quantified through d_f and R_c.

We explain these findings by using a model for the elastic modulus of fractal cluster gels in combination with the activity-induced softening of pair bonds between particles in the gel. We find that the significant reduction in viscoelastic moduli at low particle loading is explained if the theory is applied at the level of active clusters rather than active particles. This hypothesis indicates that active particles embedded in fractal clusters activate the whole cluster, consistent with previous reports for Brownian clusters [8], [80], [81], [144], [145].

By considering varying degrees of coupling between the active particles and the fractal clusters, we find that the gels studied here are best explained by fractal clusters that are activated by the active particle embedded in them with an efficiency of about 30%. While this parsimonious model – with one adjustable parameter – captures both the scale of the rheological effect and the trend at low active particle energies, it over predicts the amount of rheological change at the largest active energies.

The findings and modeling raise additional questions that could be the subject of future research. First, the consistency of our findings with the hypothesis of active clusters motivates

work to characterize – either by simulation or experiment – the correlated microdynamics of colloids in fractal clusters containing Janus inclusions. Such a study could shed light on how the active dynamics of the Janus particles couple to produce active fluctuations of the clusters in which they are embedded. Second, additional modeling or simulation could address the nature of electric and chemical species fields within disordered materials with embedded catalytic Janus particles, including fractal clusters. Such a study would address the fundamental electro-diffusiophoretic origin of the coupling between active and passive colloids in networks such as those created in this study. Further, additional research could also address the level to which added chemicals such as H_2O_2 modulate particle pair potentials, thereby presenting an additional factor needed in modeling. For instance, prior work has suggested that gel stiffening in the presence of H_2O_2 is independent of its concentration; however, such a dependence could explain the trend in activity effects. Third, an unexamined dimension of this study is the potential effects of metallic van der Waals interactions on modeling results through the strong effects of metals on van der Waals interactions. Such a study could proceed by varying the platinum layer thickness and probing effects on rheological properties, since the Hamaker constant of metallodielectric particles depends on the metallic layer thickness [149]. Fourth, it would be interesting to increase activity levels further in the gel so as to produce a material with a variable yield strain, or even, an auto-yielding material. The latter would recapitulate in experiment features identified in the simulation study of Omar et al. Fifth, experimental and modeling work on the dynamics of isolated fractal clusters can address how the degree of cluster activation scales with the size and number of passive and active particles in each fractal cluster. Work in the above directions would further elucidate the way in which interparticle interactions, microstructure, and dynamics mediate the rheological properties of these novel gel materials.

The results from this study create a new kind of functional material with multi-state mechanical properties. By simply "turning on" activity – for example, through the addition of fuel like hydrogen peroxide, light, or other means – a dramatical change in elastic moduli and yield stress could be obtained. These materials can be considered to be functionally similar to stimuli-responsive polymeric materials that change their chemical and physical properties when exposed to different stimuli such as light and mechanical force [150]–[153].

An implication of the present work is that only minute quantities of the active agent (here –Janus particles) need be added to the formulation to affect rheology. The small quantities of material added preserves the structure of the material. This attribute, for instance, results in a material with a reconfigurable yield stress but a constant yield strain.

Finally, much still needs to be researched to support the potential application of active colloidal gels in areas such as consumer products, agriculture, and pharmaceuticals. Active matter constituents – both particle and fuel – that are inexpensive, safe, and environmentally benign are needed, for example. Additionally, larger rheological changes than the three-fold levels observed here would expand the range of utility of this class of material. Finally, even within the class of catalytic Janus particles improvements addressing fuel depletion and reaction product building (with the latter leading to bubbles) would be welcome. Nevertheless, the present work demonstrates that non-linear rheological properties can be manipulated by incorporating dilute concentrations of active matter into colloidal gels.

2.6 Supplementary Material

2.6.1 Yield stress from crossover of G' and G" in oscillatory strain sweeps

The crossover modulus from the oscillatory strain sweep measurements (found in Figure 7 of the main text) is 0.58 ± 0.10 Pa and 0.25 ± 0.18 Pa for the passive ($E_A/k_BT = 0$) and active

(containing Janus colloids with E_A/k_BT = 11) gels, respectively. The strain amplitude of the crossover in both cases is 0.048 ± 0.003 and 0.081 ± 0.030 for passive and active gels, respectively. If this crossover point is taken as the yield point, the resulting yield stresses are 0.027 ± 0.004 Pa and 0.009 ± 0.003 Pa, respectively. A 2-sample T-test for the yield stress data equals 0.0114 indicating that the differences are statistically significant. Both the yield stress measurements and their statistically significant difference are consistent with the results obtained from strain amplitude dependent elastic strain measurements, as reported in the main text Figure 2-7 (b).

2.6.2 Pair-Potentials for particles in the gels

Following [20], the potential interaction between particle pairs in the gel , U(*s*), as a function of their surface-to-surface separation *s*, is the sum of van der Waal's attraction (U_{vdw}) and electrostatic repulsion (U_{el}) potential:

$$U(s) = U_{vdw}(s) + U_{el}(s) \qquad (2\text{-}5)$$

Where, the individual terms are [27]:

$$U_{vdw}(s) = \frac{-A}{6}\left[\frac{2a^2}{s^2+4as} + \frac{2a^2}{s^2+4as+4a^2} + \ln\left(\frac{s^2+4as}{s^2+4as+4a^2}\right)\right] \qquad (2\text{-}6)$$

and:

$$U_{el}(s) = \left(\frac{a}{2}\right) Ze^{-\kappa s} \qquad (2\text{-}7)$$

Here, A is the Hamaker constant (1.26 x 10^{-20} J for polystyrene in water), *a* is the particle radius (0.5 μm) and κ^{-1} is the Debye Length (0.695 nm for [$MgCl_2$] = 64mM) and Z is an interaction constant (Z = 5.9 x 10^{-11} J m^{-1})[27].

Boltzmann averages over thermal fluctuations of surface-to-surface separation were calculated as:

$$\langle s \rangle = \int_0^\infty \left(s e^{-U(s)/k_B T} \right) ds \Big/ \int_0^\infty \left(e^{-U(s)/k_B T} \right) ds \qquad (2\text{-}8)$$

2.6.3 Gel structure comparison of fluorescent vs undyed colloidal gels

To compare the structure of gels made of fluorescent particles (used in confocal experiments) and those made of undyed particles (used in rheology experiments), both gels are imaged in reflection mode with the 488nm laser on the confocal microscope (Nikon A1Rsi equipped with NA = 1.4, 100x objective). Visible structure is possible because of the low volume fraction of the gels. However, in this reflection mode, images are of lower quality and exact particle locations of a 3D image stack with Trackpy is not possible. Therefore, we instead use a 2D image ~ 8um above the coverslip with a MATLAB code that compares the area of connected regions in that image. The connected regions in this case are parts of clusters of the gel. An example of the process is given in Figure 2-10.

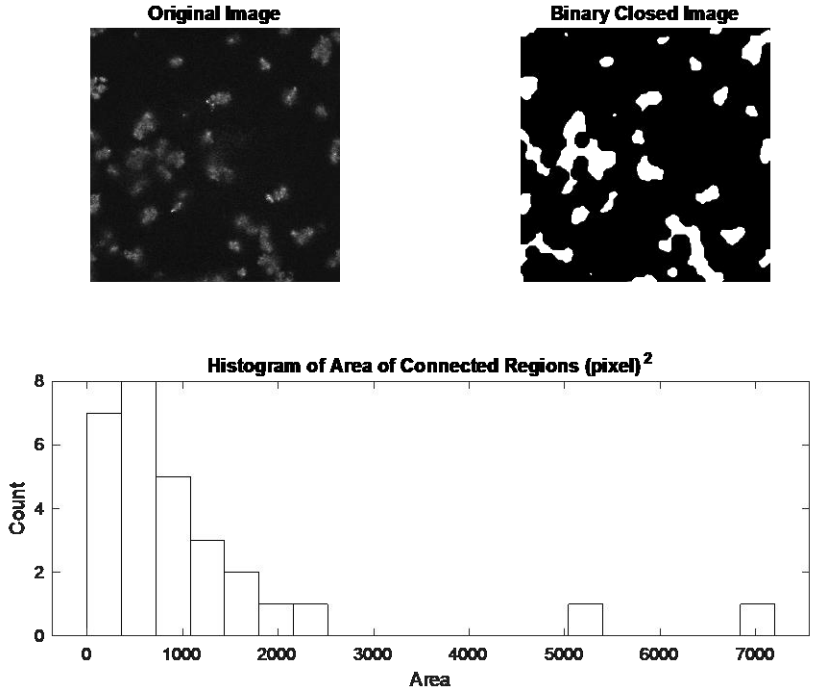

Figure 2-10: Process for extracting the area of connected regions in confocal images in reflection mode of fluorescent and undyed colloidal gels. (a) Raw confocal image, (b) Processed image and (c) cluster size distribution from processed image.

The probabilities of the sizes of the connected regions in the fluorescent and undyed gels (five of each) is evaluated to compare the structures. The results of this comparison are shown in the histogram of Figure 2-11. The histograms of the two gels are very similar, overlaying very well for sizes < 4000 (pixels^2). There are discrepancies for values > 4000 (pixels^2). However, the discrepancies occur for values that have a probability that is on average ~0.01 or less. Therefore, the difference is not as resolvable and could be a result of image acquisition. We therefore conclude that the fluorescence does not affect the gel structure.

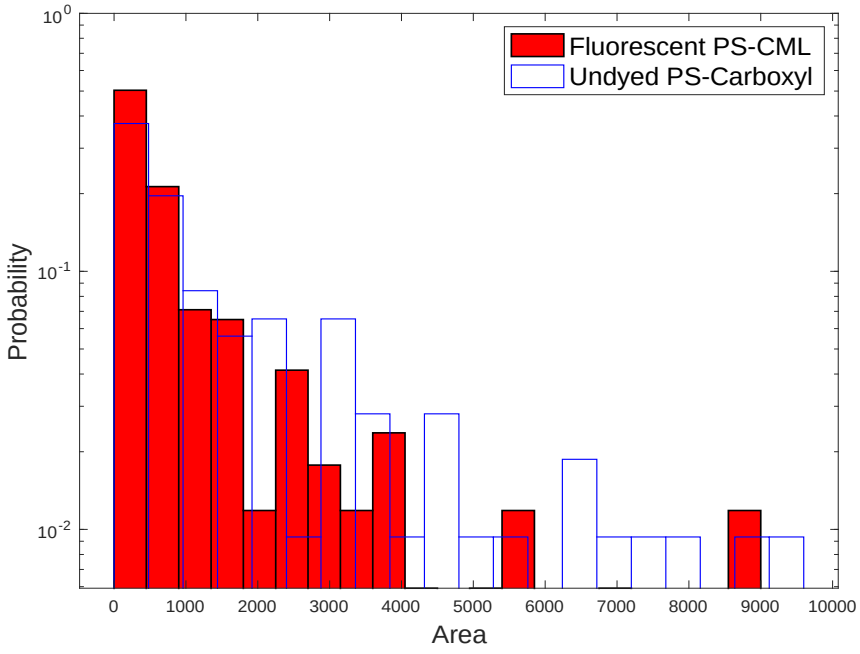

Figure 2-11: Probability histogram of size distribution of connected regions in fluorescent and undyed gels

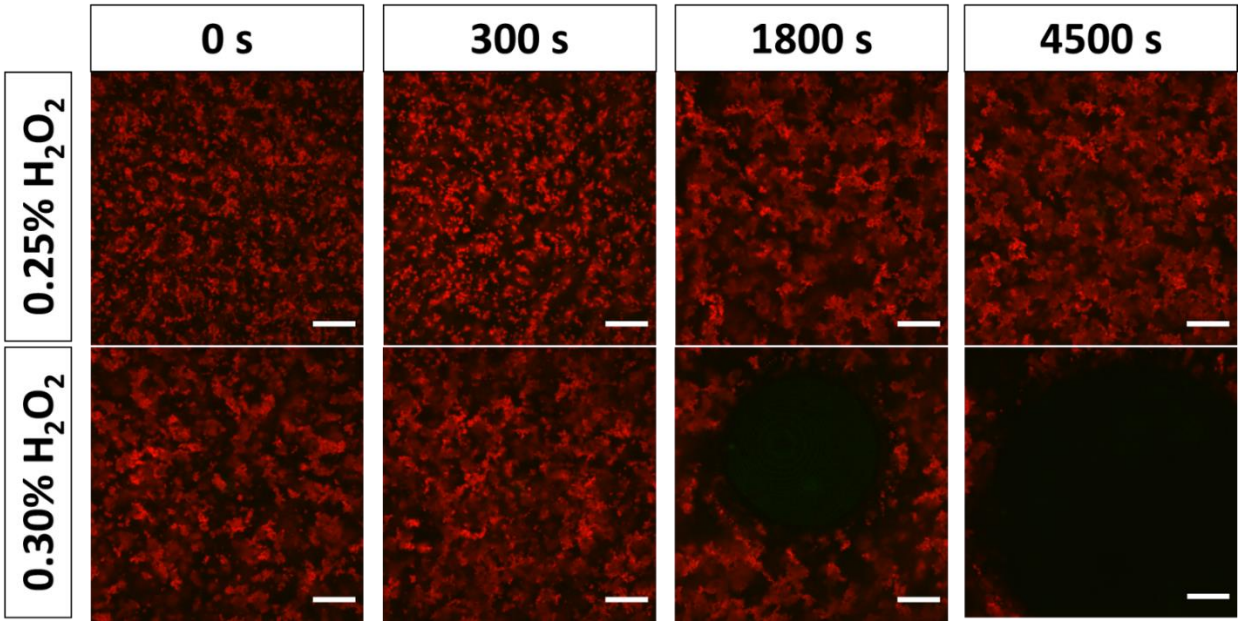

Figure 2-12: Confocal images (40x objective, NA = 0.95) to check for microbubbles in active gel systems containing 0.25 wt% and 0.3 wt% H_2O_2. The scale bar is 50 μm. Gels with 0.30 wt% H_2O_2 displayed micro-bubbles at 1800 seconds or earlier while gels with 0.25 wt% showed no micro-bubbles for the duration of the 4500 seconds experiment. Because of this, the maximum amount of H_2O_2 in rheology experiments was 0.25 wt% H_2O_2. Active gels have an active to passive particle ratio of 1:1200.

a)

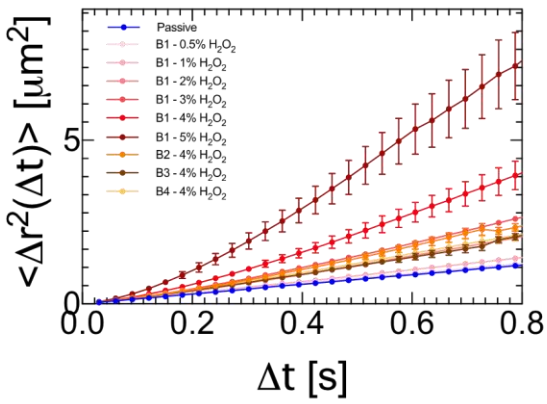

b)

Batch	% H_2O_2	v (μm/s)	l (μm)	E_A $(kg*m^2)/s^2$	E_A/k_BT
1	0.025	0.81 ± 0.03	0.63± 0.02	4.85E-21	1.2
1	0.05	0.85 ± 0.02	0.66 ± 0.01	5.29E-21	1.3
1	0.1	1.42± 0.01	1.10 ± 0.01	1.47E-20	3.6
1	0.15	1.98 ± 0.02	1.54 ± 0.01	2.87E-20	7.1
1	0.2	2.47 ± 0.04	1.92 ± 0.03	4.45E-20	11.0
1	0.25	3.72 ± 0.07	2.89 ± 0.05	1.01E-19	25.0
2	0.2	1.75 ± 0.03	1.36 ± 0.02	2.25E-20	5.6
3	0.2	1.55 ± 0.05	1.20 ± 0.04	1.75E-20	4.3

Figure 2-13: Microdynamics and energy of free active particles. a) mean squared displacements of active particles from batches 1 and 2 at each hydrogen peroxide concentration. Each condition contains at least 7 measurements. Error bars are standard error of the mean. b) Summary of the particle velocity (V), run length (l), and active energy (E_A) at each hydrogen peroxide concentration computed for each condition. Calculations were performed as described in the text. The velocity was calculated by fitting the short time mean squared displacements to the limiting expression, $\langle \Delta r^2(\Delta t) \rangle = 4D\Delta t + V^2\Delta t^2$, described by Howse et al. [16]. *Run length was calculated using the velocity extracted from short-time mean squared displacements and the reorientation time computed from the rotational diffusivity as per theory* [16]. *Errors are standard errors of the fit. Active energies were calculated using per Takatori et al. as described in the text* [131]. *Additionally, k_BT = 4.04e-21 $m^2kg/(s^2K)$.*

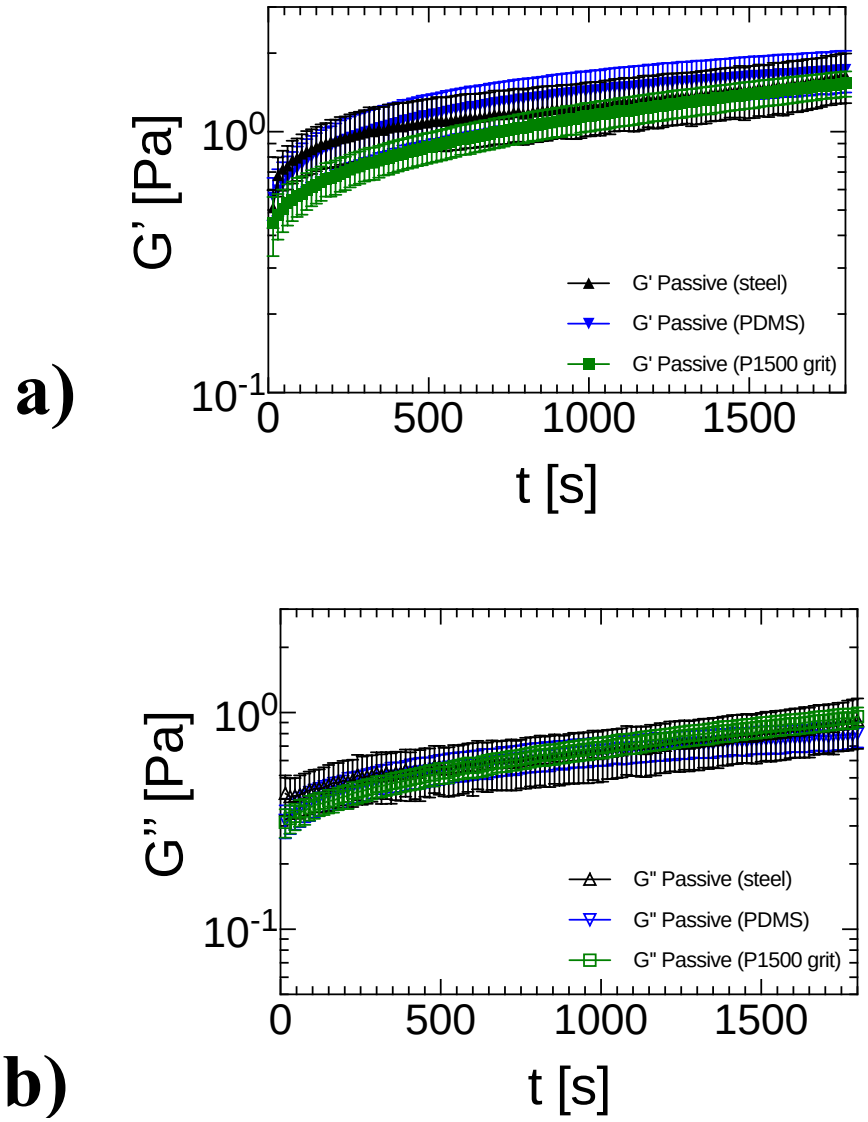

Figure 2-14: Linear viscoelastic moduli, (a) G' and (b) G'' of passive colloidal gels as a function of time (γ_0 = 0.003 and ω = 1 rad/s) with various plate coatings. The results show that PDMS accurately captures the rheology of our colloidal gels because the results for this coating are not distinguishable from those for the smooth plates or rough plates (P1500 grit silicon carbide sandpaper). Szakasits et al. further show the PDMS plates also accurately capture the rheology of a standard PEO solution [20]. *Error bars are standard error of the mean.*

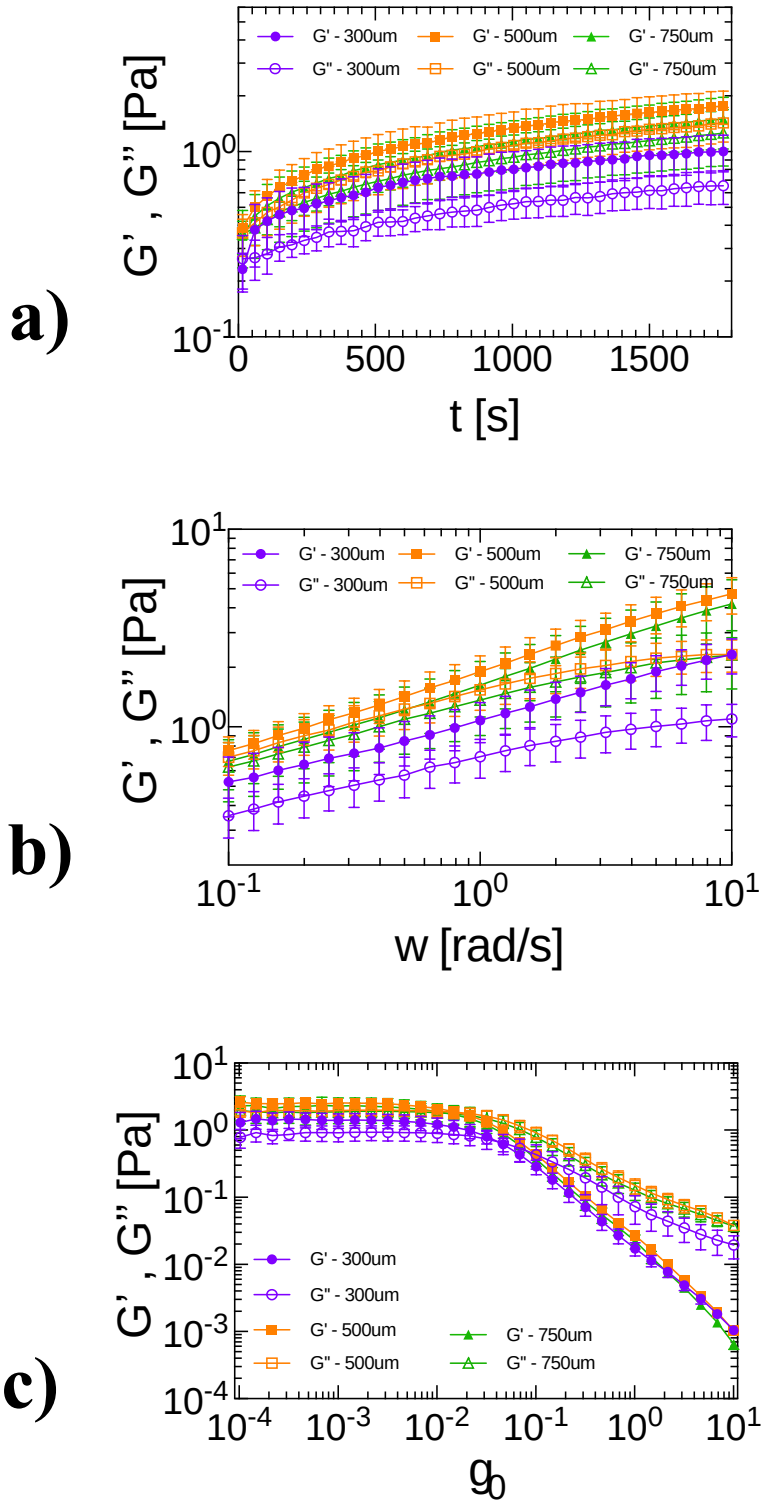

Figure 2-15: Gap study of passive gels at gaps of h = 300, 500, and 750 μm. Storage and loss moduli (G', G'') as a function of (a) time at γ_0 = 0.003 and ω = 1 rad/s; (b) frequency at γ_0 = 0.003 and time = 1800 s; and (c) strain amplitude at ω = 1 rad/s and time = 3300 s.

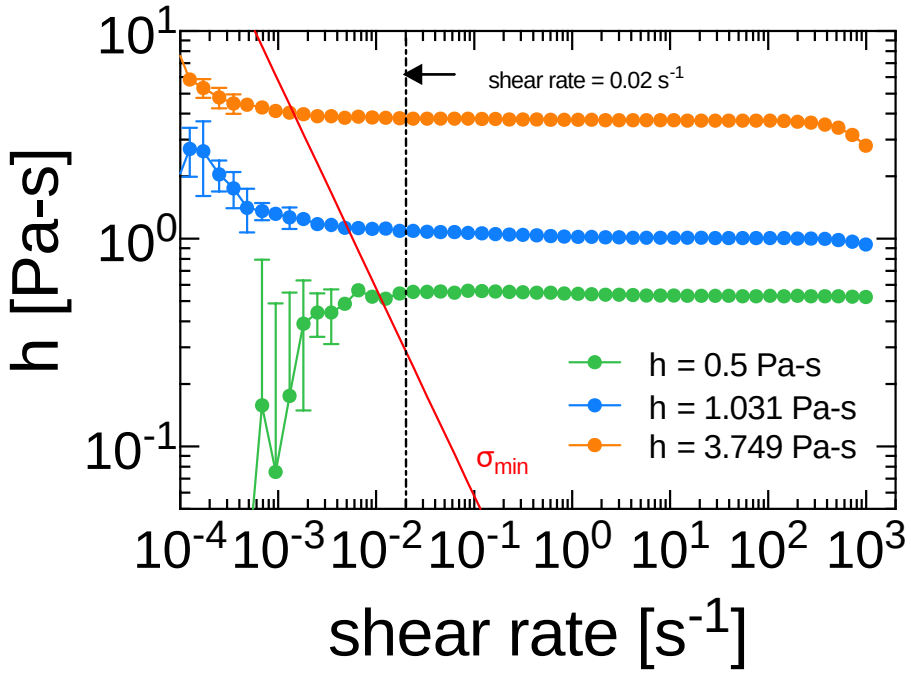

Figure 2-16: The lower stress limit of the rheological instrument used in this study was estimated from flow curve measurements of viscosity standards ($\mu = 500cp,\ 10301cp,\ 3749cp$). Shear rates ($\dot{\gamma}$) at which the viscosities (η) became consistent – having a standard error of the mean less than 2.5% of the reported value – define the lower stress limit as $\sigma = \eta\dot{\gamma} = 2.9 \times 10^{-3}$ Pa, marked here as the red-line. The shear stresses measured in this study are higher by two-fold or more than this lower limit).

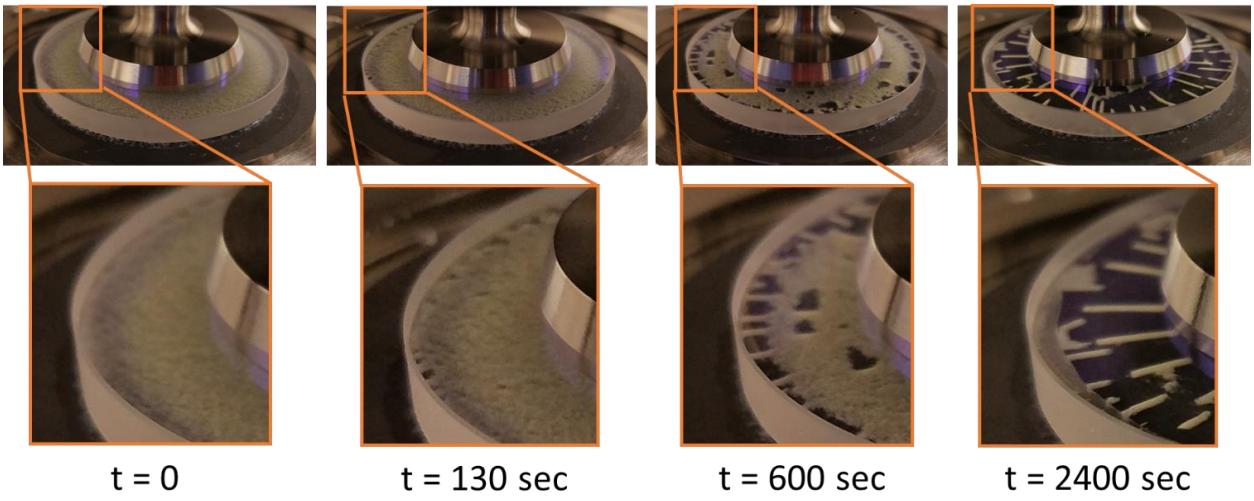

Figure 2-17: The passive colloidal gel was initially visually homogeneous at t = 0 sec during a steady shear experiment ($\dot{\gamma} = 0.02\ rad/sec$) with a 43mm glass plate. At 130 seconds into the experiment, the beginning of flocculation is visible along the edges of the fixture. By the end of a 2400 second experiment, the sample is fully comprised of flocculated roll cells. Because of this visible flocculation, only data for t < 60s is analyzed.

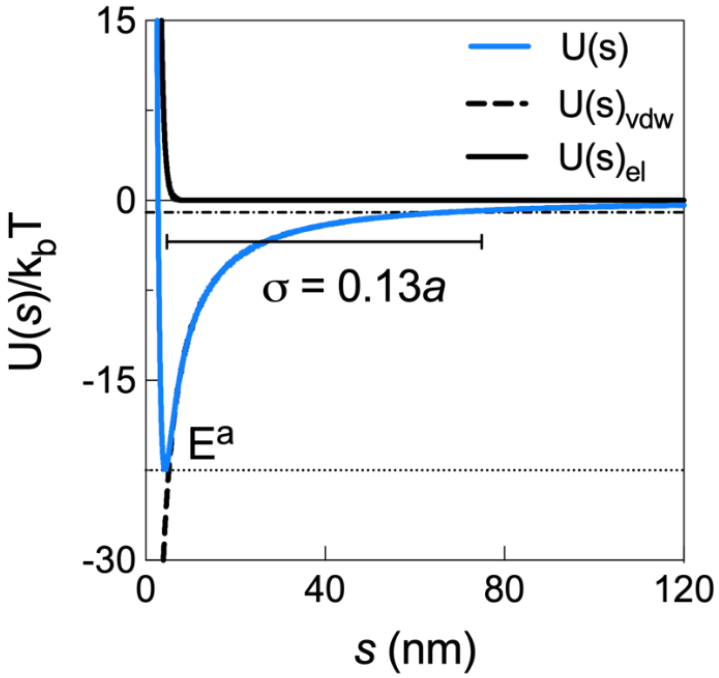

Figure 2-18: Pairwise potentials, $U_{el}(s)$ (electrostatic repulsion), $U_{vdw}(s)$ (van der Waal's attraction) and $U(s) = U_{el} + U_{vdw}$ as a function of the interparticle separation s normalized by the thermal energy k_BT. The horizontal dotted line indicates the well depth, E^a. The horizontal dot-dashed line is drawn at $U(s)/k_BT = -1$. The interaction range, where $U(s)/k_BT \leq -1$, is $\sigma = 0.13a$, where a is the particle radius. Here, T = 298K. Generated by Mahesh Ganesan.

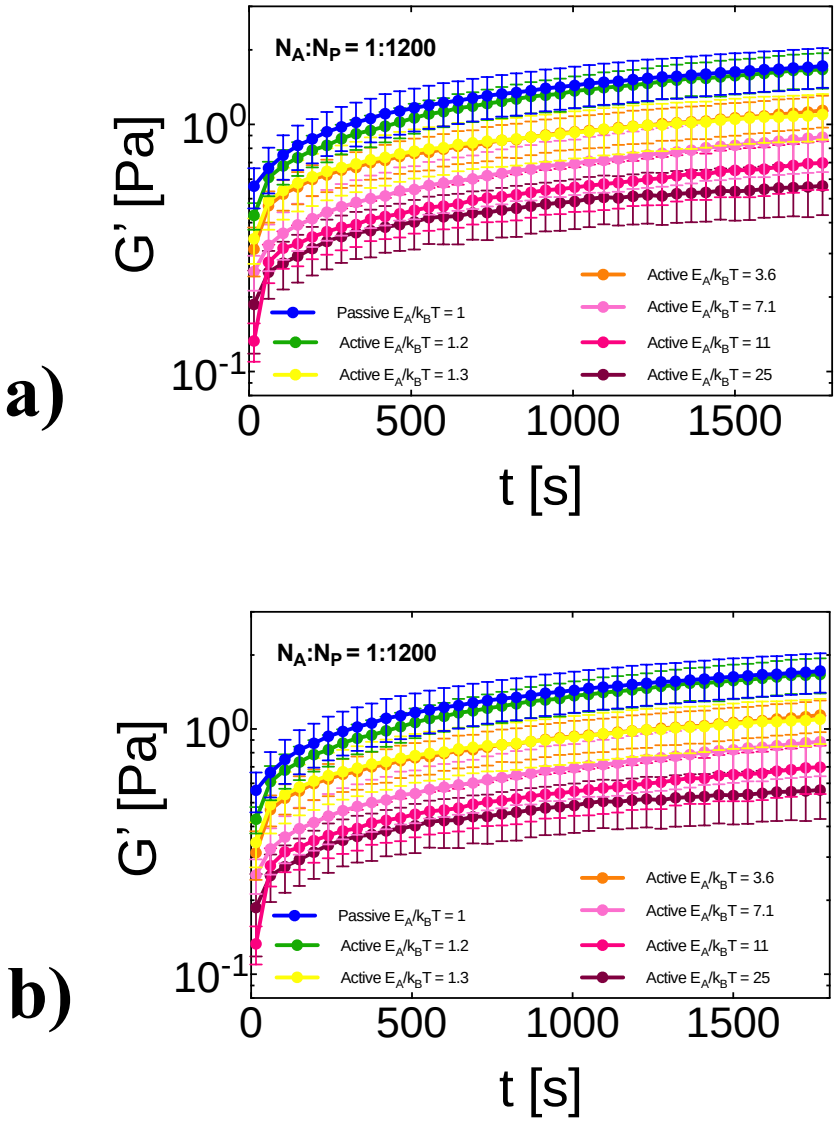

Figure 2-19: Full data set from Figure 2-5 (a) in the text. The (a) elastic and (b) viscous moduli of colloidal gels as a function of time and with increasing H_2O_2 concentration/active energy ratios are plotted ($\gamma_0 = 0.003$ and $\omega = 1$ rad/s). The active gels in this figure contain 0.003% v/v of Janus particles from B1 with H_2O_2 concentrations of 0.025%, 0.05%, 0.1%, 0.15%, 0.2%, and 0.25%. The passive gels contain no Janus particles and a H_2O_2 concentration of 0.5%. Additionally, k_BT = 4.04e-21 $m^2kg/(s^2K)$.

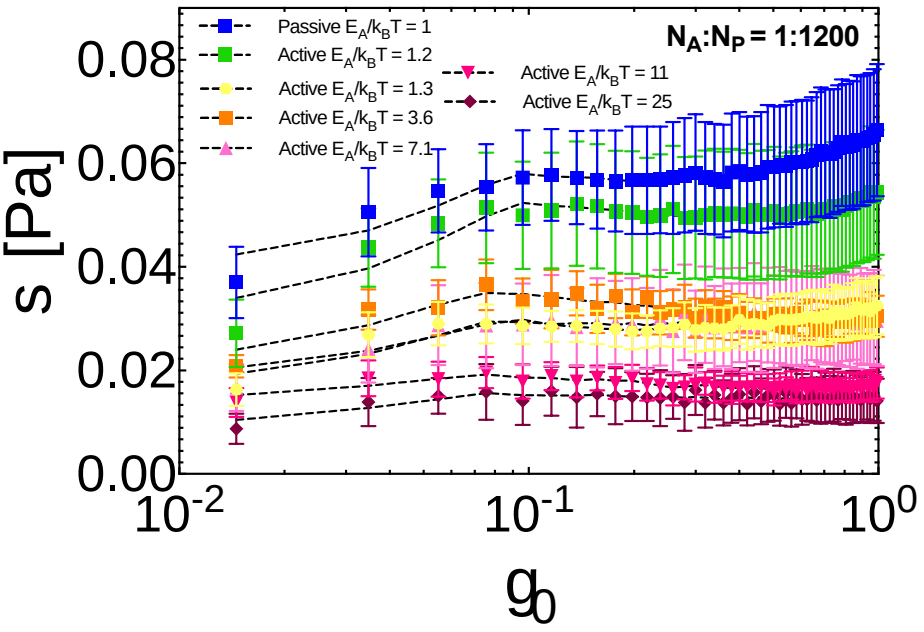

Figure 2-20: Full data from Figure 2-5(b) in the text. The steady shear stress at a shear rate of 0.02 s^{-1} for passive gels and active gels of all active energy ratios are reported after 1800 s of initial gelation. The active gels in this figure contain 0.003% v/v of Janus particles from B1 with H_2O_2 concentrations 0.025%, 0.05%, 0.1%, 0.15%, 0.2%, and 0.25%. The passive gels contain no Janus particles and a H_2O_2 concentration of 0.5%. Additionally, k_BT = 4.04e-21 $m^2kg/(s^2K)$.

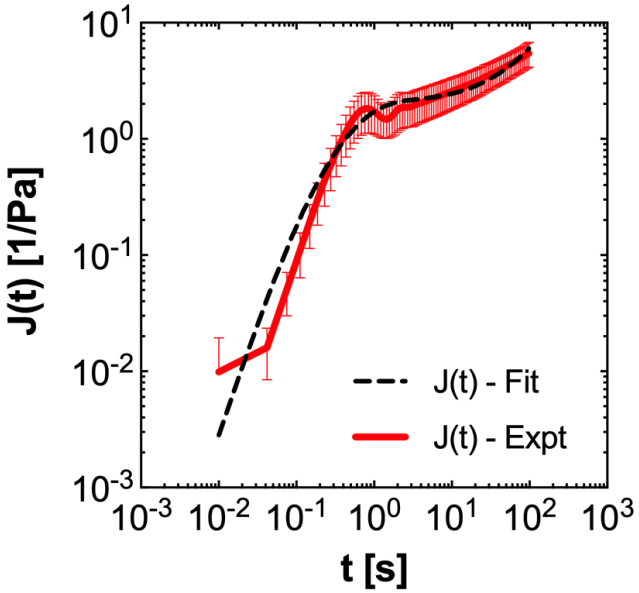

Figure 2-21: Creep compliance, J(t), of passive gels fit with a single mode Jeffreys model. The experimental curve represents the linear region of creep response (stress of 0.001 – 0.03 Pa) from Figure 8(a) of the main text. The error bars are standard error of mean. Equations for creep response of Jeffreys model used here are provided in [154], [155]. *Generated by Mahesh Ganesan.*

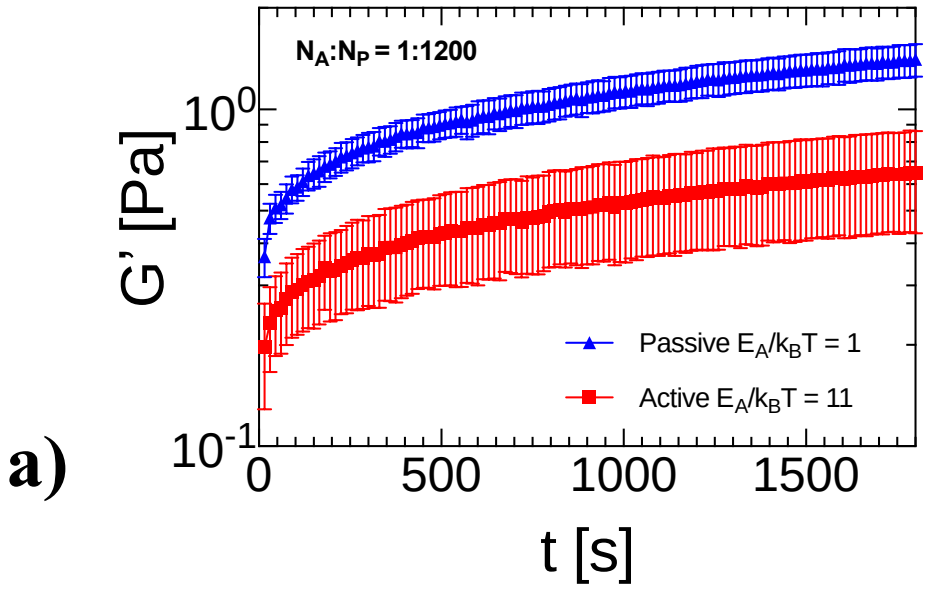

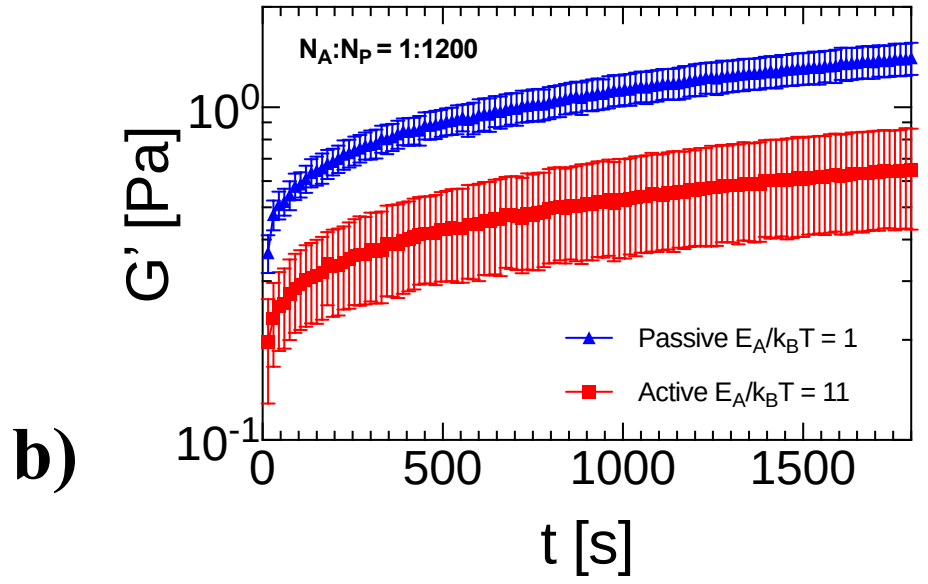

Figure 2-22: Initial 1800 s time sweeps (γ_0 = 0.003 and ω = 1 rad/s) of the passive and active gels (a) before oscillatory strain sweeps and (b) before creep experiments. (a) contains Janus particles from B1 with 0.2 wt% H_2O_2; (b) contains Janus particles from B2 with 0.2 wt% H_2O_2. These data are monitored to confirm the effect of activity and to compare the drop in modulus to that in the start up of shear flow experiments

Chapter 3 Microdynamics of Active Particles in Defect-Rich Colloidal Crystals

3.1 Abstract

Hypothesis

Because they are self-propulsive, active colloidal particles can interact with their environment in ways that differ from passive, Brownian particles. Here, we explore how interactions in different microstructural regions may contribute to colloidal crystal annealing.

Experiments

We investigate active particles propagating in a colloidal crystal monolayer produced by alternating current electric fields (active-to-passive particle ratio ~ 1:720). The active particle is a platinum Janus sphere propelled by asymmetric decomposition of hydrogen peroxide. Crystals are characterized for changes in void properties. The mean-squared-displacement of Janus particles are measured to determine how active microdynamics depend on the local microstructure, which is comprised of void regions, void-adjacent regions (defined as within three particle diameters of a void), and interstitial regions.

Findings

At E_A = 2.55 k_BT, the average void size increases as much as three times and the average void anisotropy increases about 40% relative to the passive case. The overall microdynamical enhancement, <d(t)>, of Janus particles in the crystal relative to an equivalent passive Janus particle is reduced compared to that of a free, active particle (<d(t)> is 1.88 ± 0.04 and 2.66 ± 0.08, respectively). The concentration of active particles is enriched in void and void-adjacent regions. Active particles exhibit the greatest change in dynamics relative to the passive control in

void-adjacent regions (<d(t)> = 2.58 ± 0.06). The results support the conjecture that active particle microdynamical enhancement in crystal lattices is affected by local defect structure.

This chapter was adapted from a publication that is in preparation: K. T. Saud and M. J. Solomon, “Microdynamics of active particles in defect-rich colloidal crystals”. Keara T. Saud and Michael J. Solomon conceived this research and designed the experiments. Keara T. Saud conducted the experiments.

3.2 Introduction

Colloidal crystals are a model system well suited to fundamental study of crystallization and crystal properties [2], [24], [156]. Such crystals are central to the function of structural color materials [48], [49]; they have also been proposed as templates for membranes [44], [45] and for batteries [46], [157]. Because their Brownian motion produces thermodynamic equilibrium, colloids can be self-assembled into crystalline states by a variety of methods including sedimentation [58], evaporation [48]–[50], and the application of electric fields [56], [57]. The quality of the resulting crystal has direct implications for mechanical [158]–[160] and optical properties [48], [49]. As such, control of the crystallinity via methods such as field-induced annealing has been the subject of research [57], [58], [66], [161], [162]. Annealing typically involves the use of thermal processing to evolve kinetically trapped microstructures into more favorable, equilibrium ones. However, other methods, including toggling electric and/or magnetic fields can also improve crystallinity through mechanisms that are similar to thermal processing [57] [163].

One annealing method that has received recent attention involves the incorporation of active particles into the crystal lattice [58], [66], [161], [162]. Active particles are self-propelled objects; they are constituents of active matter that behave differently from their passive,

Brownian counterpart. Active matter has features in common with emergent structures found in nature, such as flocks of birds, swarms of fish, and colonies of bacteria. Colloidal forms of active matter make use of asymmetric energy conversion around individual particles to generate self-propulsion. This energy can come from sources such as chemical reactions [16], light [6], [7], [164], and electric fields [10], [11], [165]. The local gradients of molecules and ions that result from this local energy conversion induce self-propulsive behavior of single particles. For example, platinum Janus particles experience self-propulsive behavior in the presence of hydrogen peroxide (H_2O_2) [16], [17], [75], [122]–[124]. Their self-propulsion stems from the species and ionic concentration gradients that result from asymmetric decomposition of H_2O_2.

Such self-propulsion can contribute to annealing of colloidal crystals produced by self-assembly. Ramananarivo et al. propose the following mechanism for such annealing: propulsion yields increased collisions of active particles with other particles in the crystal lattice. These increased collisions drive fluctuations that can assist in freeing the system from kinetically trapped states. Van der Meer et al. showed by simulation that active particles enhance grain boundary mobility in both 2D and 3D colloidal crystals. This mobility promotes the formation of a single crystal [66], [162]. Ramananarivo et al. furthermore showed that incorporating small fractions of light-activated active particles into a 2D colloidal crystal resulted in accelerated annealing. This annealing could additionally be spatially controlled so that only regions that are exposed to the particle-activating light were annealed [58]. Additional studies have explored how active particles navigate a crystalline surface made of deposited, equally sized colloidal particles [74] and in non-close packed crystals at oil-water interfaces [19]. Computational studies have shown that active particles may also be able to pin crystal dislocations [159].

These studies have shown that active particles can have complex interactions with crystalline environments and even promote annealing of defects in colloidal crystals. However, the interactions and mechanisms involved in this activity-controlled annealing have not been fully elucidated, particularly in crystals that are rich in defect structures. Specifically, studies have yet to address how changes in defect structures are correlated with the microdynamics of the active particles that are proximate to them. We are thus led to address the following question in this study: How do the local properties of the crystal lattice itself, including proximity to defect structures, affect the microdynamics of active particles relative to free solution? Within this same system, we also explore how the defect structures themselves are in turn affected by active particles. Addressing this research question will yield greater understanding of how active matter can promote annealing in crystals. Such understanding could assist in the selection of active particle properties (e.g. the level of active energy and the concentration) for an application requiring a certain level of annealing. Alternatively, if a specific microstructural region of crystal is impacted by active energy to a greater or lesser degree than other regions, this could inform understanding of that region's potential for transformation by annealing.

We thus here pursue a microdynamical analysis of platinum Janus particles in a colloidal crystal produced by AC electric field assisted self-assembly. Confocal laser scanning microscopy (CLSM) is used to visualize the microstructure of the colloidal crystals and the microdynamics of the Janus particles embedded in it. Activity induced microdynamical changes are quantified and the system is also evaluated for changes in microstructure correlated with the introduction of active particles. We resolve the microdynamics of Janus particles by identifying them as residing in one of three regions: voids, void-adjacent regions, and interstitial sites. For the case of active energy about twice the thermal energy, we find that the active Janus particles have the greatest

enhancement in microdynamics in the void-adjacent regions of the colloidal crystal. The results suggest further avenues to study how active particles anneal colloidal crystals.

3.3 Materials and Methods

3.3.1 Colloidal and Janus Particles

Monodisperse polystyrene (PS) colloids are used in this study. Crystal lattices are self-assembled from 3.7 ± 0.04 μm red (580/605) fluorescent sulfate-modified PS microspheres purchased from Thermo Fisher Scientific (F8858, lot 2291491, density $\rho = 1.055$ g/m). Janus colloids used in this study are produced from 1.0 ± 0.03 μm green, fluorescent sulfate-modified PS (F8852, lot 2234961, density $\rho = 1.055$ g/mL). To synthesize Janus particles, the 1.0 μm particles are spin coated as a monolayer onto a cleaned glass slide; 25 nm of platinum is then deposited via physical vapor deposition (Enerjet Evaporator). This deposition covers the surface of one hemisphere of the particle with platinum; the other half is unmodified. The particles are recovered from the slide and suspended in 18.2 MΩ Millipore water until used. The stock concentrations of the self-assembled, passive colloids and the Janus particles are 0.034 vol% and 0.0015 vol% respectively, as determined by hemocytometry (NanoEnTek Inc.).

3.3.2 Characterization of the active particle energy

Active colloids exhibit enhanced random walks relative to their passive counterparts. For Pt Janus colloids in aqueous solutions of hydrogen peroxide (H_2O_2), this enhancement is due to localized chemical reactions, which yield concentration and ion gradients. These species and ionic gradients drive self-diffusiophoretic and self-electrophoretic flow, respectively [75].

Measurements of the expanded random walk of the active particles characterize their active energy relative to what they would experience at thermal equilibrium. Briefly, following

Takatori et al. [131], the active energy of a Janus colloid, $E_A = \xi V l$ where ξ is the hydrodynamic drag coefficient, V is the active particle velocity in free solution, and l is the active particle persistence length which is equivalent to $l = \tau_R V = \left(\frac{8\pi\mu a^3}{k_B T}\right) V$. E_A is scaled relative to the thermal energy of free passive particles, $k_B T$, at T = 298 K.

The self-electrodiffusiophoretic flows that govern locomotion are sensitive to system conditions like solvent, conductivity, and electric field magnitude[11], [13], [71], [166]; this is relevant to the present study because AC electric fields are used to self-assemble the crystal lattice of passive colloids in which the Janus particles are active. We therefore characterized the locomotion of the free active colloids in this environment (V_{rms} = 16 V/mm; frequency = 5 MHz).

The active particle velocity was measured by imaging the dynamics of at least 35 particles per activity level with confocal laser scanning microscopy (Nikon A1Rsi, NA = 1.4, 100x objective). The active trajectories of these particles were determined by image analysis, using Trackpy, a Python implementation of the algorithm discussed in Crocker and Grier [167]. Two channels were used: the platinum layer of the Janus colloid was imaged in reflection mode with a 488 nm laser and the fluorescent PS of the Janus colloid was imaged at 488 nm excitation and for an emission band from 500 to 550 nm. The pixel size was 124 nm and the image size was 256 x 512 pixels. Videos containing 1 – 3 Janus colloids were collected at a frame rate of 20 fps for a duration of 10 s. Particle velocities were calculated by fitting the early-time mean squared displacements (MSD, $< \Delta r^2(\Delta t) >$) to the equation $\Delta r^2 = 4D\Delta t + V^2\Delta t^2$, which is valid for times much less than the reorientation time, $\tau_{R,}$ (0.78 s) which was computed from the rotational diffusivity [16], [42], [131]. The H_2O_2 concentrations studied (1.7 wt% and 3.3 wt% H_2O_2) yielded persistence lengths of 0.59 and 0. 92 μm and scaled free particle active energies of 1.05

k_BT and 2.55 k_BT, respectively. The supplementary material (Figure 3-7) reports the data used for these active energy calculations.

For later comparison with Janus particle dynamics in the self-assembled crystals, the microdynamical enhancement of these free active particles was characterized using the function $\delta(\Delta t) = \frac{<\Delta r^2(\Delta t)>_{active}}{<\Delta r^2(\Delta t)>_{passive}}$ [168]. The average $< \delta(\Delta t) >$ of the range of lag times studied for 1.05 k_BT and 2.55 k_BT were 1.59 ± 0.04 and 2.66 ± 0.08, respectively. Alternatively, this enhancement can be quantified at the characteristic time of τ_R. At this characteristic time, we have $\delta(\tau_R)$ = 1.37 ± 0.19 for the 1.05 k_BT case and $\delta(\tau_R)$ = 2.13 ± 0.24 for the 2.55 k_BT case. The data used for these $\delta(\Delta t)$ values is reported in the supplementary material (Figure 3-8).

3.3.3 Preparation of colloidal crystals and introduction of activity

To generate a colloidal crystal monolayer in which the active particles propagate, the procedure of Kao et al. [56], [57] is used with slight modification. Briefly, the 4.0 μm diameter PS colloids are filtered (Isopore 5.0 μm PC membrane) and suspended in 0.1 mM NaCl. A small amount (<< 1% by number) of the 1.0 μm Janus particles is incorporated in this suspension. The final active to passive particle number ratio was approximately 1:720. Using such a small amount of Janus particles served two purposes. First, it ensured that the Janus particles concentration was dilute. That is, this concentration yields average separations that far exceed the range of interaction of the Janus particles. Second, the low concentration minimized the overall amount of H_2O_2 decomposition in the system. Excessive decomposition generates bubbles that limit measurements.

A small volume (~40 μL) of the particle suspension is introduced into a coplanar AC electric field device of height approximately 1.0 mm, as described by Shah et al. and Kao et al.

[56], [57], [169]. The electrodes are created by depositing 2.5 nm Ti and 22.5 nm Au onto a coverslip (35 x 50 cm, Fisher Scientific). The electrode gap is approximately 500 μm, as generated by a 25-gauge silicone thread that is taped to the center of the slide. Before use, the electrode is cleaned in a base bath (1M KOH in isopropanol) for ~45 minutes and rinsed thoroughly. The particle suspension is allowed to sediment for one hour before applying the AC electric field (RIGOL, DG1022). A square wave with a constant field strength (16 V_{rms}/mm) and frequency of 5.0 MHz is used for all experiments. (These conditions were selected to closely match those of ref [57]). To achieve a steady-state crystal structure [57], the electric field is applied for at least 15 minutes before measurements are performed. Images were acquired as described below. This initial state, prior to the introduction of H_2O_2, functions as a control; it is referred to as the passive case. Following the collection of data for the passive case, H_2O_2 (final concentrations of 1.7 wt% or 3.3 wt%) is added through a hole at the top of the device; this addition activates the Janus colloids. The crystal is allowed to attain steady state for another 15 minutes before data collection for the active case is initiated.

3.3.4 Void analysis of colloidal crystals

The AC electric-field assembled colloidal crystals in this study contain many voids, or defect-rich regions. The statistical properties of these voids were characterized in the following way. First, the colloidal crystals were imaged with confocal laser scanning microscopy (Nikon A1Rsi, NA = 1.4, 100x objective) using the three channels previously described. For these measurements, the pixel dimension was 250 nm and the image size was 512 x 512 pixels. The imaged region was always selected to contain one Janus colloid; this region of interest was observed for 15 minutes, with images acquired at a frame rate of 0.2 fps. Particle locations in each image were identified using Trackpy [167].

Voids in the image were identified according to the following procedure, implemented by means of a python code with packages from pandas and scikit-image [170], [171]. We first binarized the 561 nm channel of the original image using an adaptive threshold from OpenCV [172] and then performed erosion and dilation operations to identify the void regions. Threshold, erosion, and dilation parameters were checked for each image sequence with parameters varying only slightly for each sequence. Functions from scikit-image yield the void number, void area (total area of a given void), void anisotropy (ratio of the major to minor axes of a given void) and the centroid of each void. The void area fraction is also reported. Figure 3-1 below provides an example of the voids extracted from an image of one of the colloidal crystals.

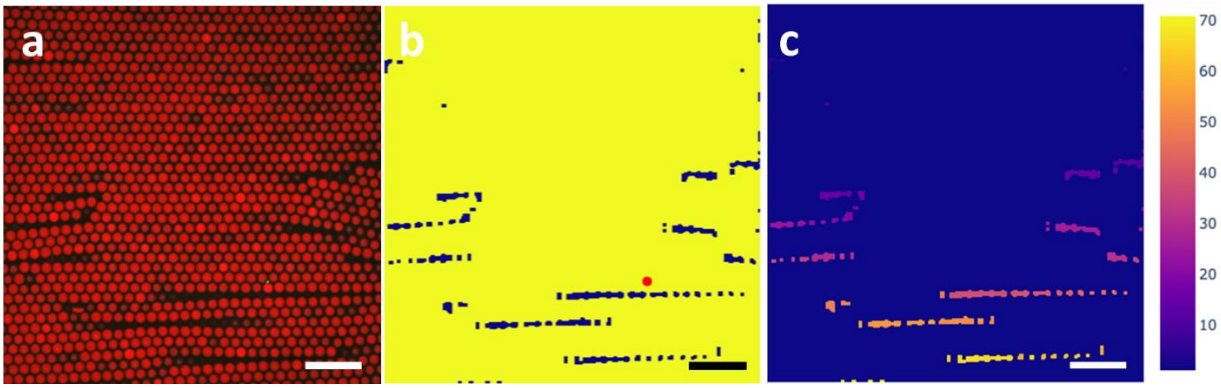

Figure 3-1: Void identification; (a) original CLSM image; (b) image with identified voids in dark blue and identified Janus particle as a red sphere; (c) image with unique voids identified by color – each color represents a different void. Scale bar is 20 μm.

The Janus particle in each frame was categorized as located: 1) within a void; 2) within a void-adjacent region, characterized as residing within three lattice particle diameters of a void; or, 3) in an interstitial site of the crystal, remote from any void. The location determination was made by manually measuring the distance between the Janus particle centroid and the closest point of the closest void. This categorization was done to determine the fraction of Janus particles located in each of these three microstructural regions.

3.3.5 Microdynamical characterization of Janus particles in colloidal crystal lattices

The microdynamics of the Janus particles were characterized with confocal laser scanning microscopy and particle tracking as they underwent active motion in the crystal lattice. The platinum layer of the Janus colloid was imaged in reflection mode with a 488 nm laser and the fluorescent PS of the Janus colloid was imaged in an emission band from 500 to 550 nm with excitation at 488 nm. The pixel size was 83 nm and the image size was 512 x 512 pixels. Videos containing 1 – 2 Janus colloids were collected at a frame rate of 10 fps. The static error in the mean squared displacement, as per an earlier study, is 9 x 10^{-4} μm^2 [125]. This error is at least two orders of magnitude less than the measured dynamics. Data is reported until 25% of particle trajectories have propagated out of the frame.

Like the regional categorization in the void analysis of the crystals, each video for microdynamics was categorized as having a Janus particle located: 1) in a void; 2) within three lattice particle diameters of a void; or, 3) in an interstitial site of the crystal remote from a void. The location determination was made by manually measuring the distance between the Janus particle centroid and closest point of the closest void during the duration of the video. If a Janus particle was present in multiple microstructural regions during the video, it was placed in the category in which it resided the greatest fraction of time.

We report the enhancement of dynamics due to activity using the measure $\delta(\Delta t) = \frac{<\Delta r^2(\Delta t)>_{active}}{<\Delta r^2(\Delta t)>_{passive}}$ [168]. Previous work has shown that this measure is time independent for confined systems such as colloidal gels [168]. Although $\delta(\Delta t)$ is nearly time-independent in the crystal lattices studied here, for a free particle, $\delta(\Delta t)$ is not necessarily time independent. Therefore, to compare between different systems, we either use an average $< \delta(\Delta t) >$, evaluated over the lag time range of the experiment, or evaluated at the characteristic time of τ_R, the rotational reorientation time of the Janus particle, $\delta(\tau_R)$.

3.4 Results and Discussion

3.4.1 Void Defect Properties

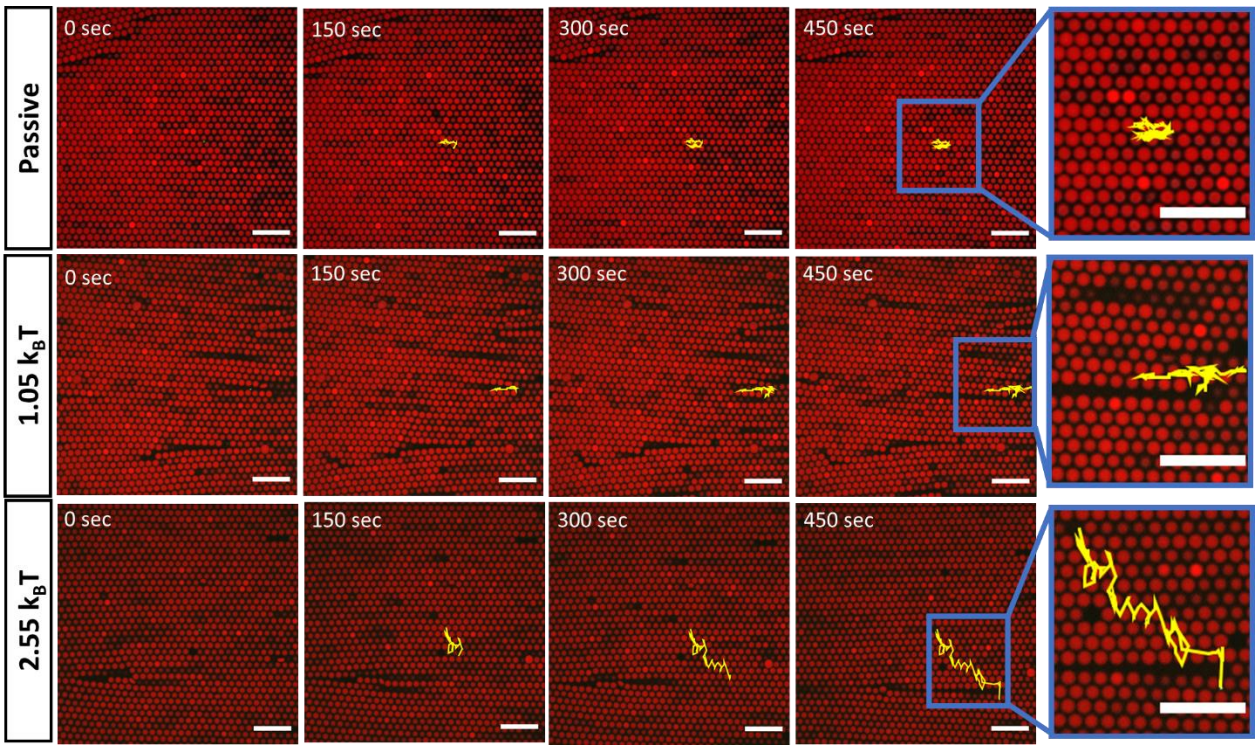

Figure 3-2: Representative CLSM images of colloidal crystal monolayers with trajectories of embedded Janus particles overlaid. The conditions are: first row, passive control; second row, E_A = 1.05 k_BT; and third row, E_A = 2.55 k_BT. The columns display images taken at specific times of the experiment. The column at far right shows the full trajectory in detail. The scale bar is 20 μm in all cases.

Figure 3-2 shows representative images of the colloidal crystal monolayers with embedded Janus particles. The applied electric field generates a crystal lattice through both dipolar and dielectrophoretic interactions, as described in [173]. The action of the field generates a defect rich crystal and prior work has shown that these defects can be resolved by annealing [57]. In Figure 3-2, the trajectories of the Janus particle acquired up to each time point (0 to 450 seconds) are overlaid on each image. The effect of active energy of the Janus particle trajectories is visually apparent. In the passive state, the Janus particle moves the least and remains within three particle diameters of its initial location. At E_A = 1.05 k_BT, the Janus particle performs

significantly greater displacement; in this case it remains in proximity to a void for the entire observation. At the higher active energy (E_A = 2.55 k_BT), the Janus particle travels the farthest; it transitions between different voids in the time shown. These images qualitatively demonstrate that the trajectory of Janus particles in colloidal crystals depends on their active energy.

Table 3-1: Summary of void properties. Error is standard error of the mean

	Passive	1.05 k_BT	2.55 k_BT
Average void size (μm^2)	9.3 ± 0.7	11.5 ± 0.1	27 ± 0.1
Average void anisotropy	2.14 ± 0.01	2.58 ± 0.02	3.00 ± 0.04
Average void number density (per mm²)	2260 ± 50	2200 ± 30	1100 ± 20
Average void area fraction	0.0210 ± 0.0005	0.0250 ± 0.0003	0.0303 ± 0.001

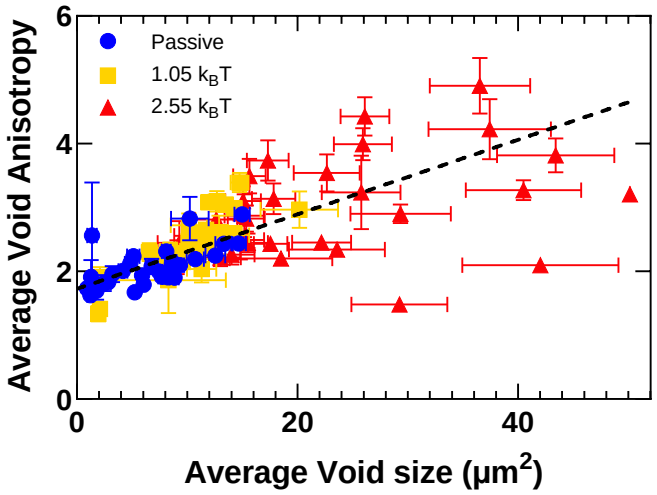

Figure 3-3: Average anisotropy of voids in the colloidal crystal as a function of their average area for the different Janus particle conditions studied. The trendline is a linear regression of the data for all conditions. Error bars are standard error of the mean.

A summary of the void properties of the crystals averaged over the duration of the experiment is shown in Table 3-1. In addition to averaging over the 450 s duration of the experiment; each measurement is also averaged over at least 5 material replicates. The void properties depend on the active energy of the embedded Janus particles. The void properties of average area, total area, and average anisotropy increase with Janus particle activity. The average

void number density decreases with activity. The overall area fraction of voids also increases with activity. All trends in void properties rise to statistical significance ($p < 0.001$).

Figure 3-3 plots the average void anisotropy vs average void area. This figure shows larger voids tend to be more anisotropic, as indicated by the trendline. In addition, the more active system ($E_A = 2.55\ k_BT$) is characterized by voids that tend to be both larger and more anisotropic than either of the two other conditions; this trend is consistent with the average values reported in Table 2-1.

Ramananarivo et al. found that active particles dispersed at concentrations comparable to the present study improved the quality of the crystal monolayers, as quantified by the bond-orientation correlation function [58]. Van der Meer et al. found that – at active particle concentrations slightly greater than this study – activity caused grain dynamics that eventually produced a single crystal from an initially polycrystalline state [66]. Our measurements agree with these reports in the following way: they show that active particles embedded at the concentrations of this study affect crystal properties by changing statistical properties of voids present in the crystals. However, the present study's observation of increased void area fraction differs from these two literature studies. The observation of greater void area fraction indicates that activity here decreases crystal quality rather than increasing it.

These measurements of activity effects on void structure have some limitations. First, the duration of the observation time is limited: The active portion of the present experiments was 15 minutes; longer times are precluded because of the increasing chance of interference from gas bubbles generated by the ongoing chemical decomposition at the catalytic surfaces of the Janus particles. Longer durations might yield clearer trends. Additionally, the range of activity levels studies, as quantified by E_A/k_BT, is limited: although the greatest possible concentration of

hydrogen peroxide concentration was used, the amount of active motion generated is modest because the AC electric field used to self-assemble the crystal also acted to suppress active motion of the Janus particles (c.f. section 3.6).

Albeit these limitations, Table 1 and Figure 3 nevertheless shown that the introduction of active particles is correlated with changes in void properties of the self-assembled crystal. Here we discuss three different hypotheses that might explain the correlation. One potential explanation for these changes is simple random variability; however, we think that unlikely given the extent of change, which rises to the level of statistical significance.

The second hypothesis involves collateral effects of the hydrogen peroxide used to activate the particles. It has previously been shown that hydrogen peroxide can alter the bond strength, or pair potential, between passive particles that form a colloidal gel [42]. Similar H_2O_2-induced change in the particle pair potential could affect the void properties by mediating changes in the particle pair potentials that affect crystallization. Additionally, the simple addition of hydrogen peroxide could disrupt the self-assembled crystal, thereby creating voids. We evaluated these possibilities by measuring the properties of a crystal lattice with no added Janus particles before and after addition of 3.3 wt% H_2O_2, which is the concentration equivalent to the $E_A/k_BT = 2.55$ case reported here. We found that this addition (performed in the absence of Janus particles) did indeed have a modest effect on void properties: void area and anisotropy increased slightly, and void number density decreased slightly (**Error! Reference source not found.**). However, each property change was modest compared to the $E_A/k_BT = 2.55$ case. Specifically, average void size changed by a factor of 4.9 less; average void anisotropy changed by a factor of 2.8 less; void number density changed by a factor of 2.2 less; and void area fraction changed by a factor of 7.2 less than the $E_A/k_BT = 2.55$ case. We therefore conclude that although H_2O_2 may

contribute to void property changes, it does not cause the full extent of changes observed in this study.

The third hypothesis is that the active particles themselves are modifying the properties of the voids in the crystal. This hypothesis is consistent with previous literature reports, particularly Ramananarivo et al. [58] who found that active particles dispersed at concentrations not too different from those studied here do improve crystal quality. The improvement was apparent from changes in the six-fold bond orientational order parameter, Ψ_6, the local orientation θ_6, and the characteristic grain radius R_6. We therefore next consider the possibility of correlation between the observed void property changes and the microdynamics of the active Janus particles in the crystal lattice.

3.4.2 Ensemble microdynamical characterization of embedded Janus particles

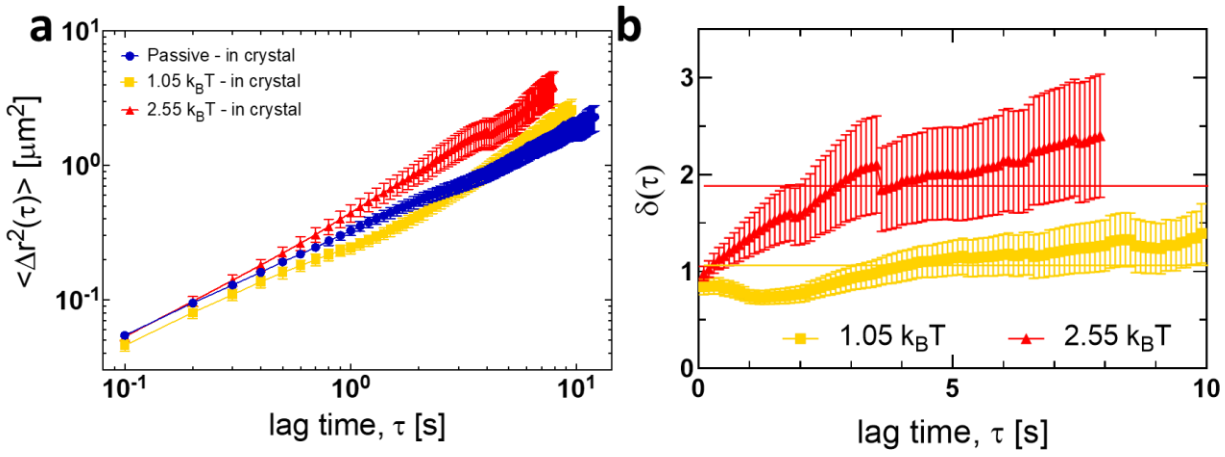

Figure 3-4: (a) Mean squared displacement of passive and active Janus particles in crystals. The data were collected 900 seconds after initiation of the AC field (passive case) or after the addition of H_2O_2 (active cases). (b) $\delta(\tau)$ vs lag time. In (b), the horizontal lines indicate the average enhancement across the set of lag times reported. Error bars are standard error of the mean and standard error of the mean of the MSDs and $\delta(\tau)$ functions, respectively.

Figure 3-4(a) reports the mean squared displacement ($< \Delta r^2(\Delta t) >$) of active particles in the colloidal crystal. $< \Delta r^2(\Delta t) >$ for E_A = 2.55 k_BT is consistently greater than the control case

of a passive Janus particle in the colloidal crystal; this trend agrees with the free particle case (Figure 3-8). For E_A = 1.05 k_BT, $< \Delta r^2(\Delta t) >$ becomes greater than the passive control only at longer lag times; this trend differs from the free particle case as discussed briefly later. The microdynamical enhancement may be quantified by $\delta(\Delta t)$, plotted in the Figure 3-4(b) and defined in the methods section. The average of this quantity $< \delta(\Delta t) >$ is 1.07 ± 0.02 and 1.88 ± 0.04 for 1.05 k_BT and 2.55 k_BT, respectively. Alternatively, at the characteristic time τ_R, $\delta(\tau_R)$ = 0.79 ± 0.08 and 1.28 ± 0.17, respectively. These $\delta(\Delta t)$ values can be compared to those for the free active particles, as reported in the methods. Those measurements found the average $< \delta(\Delta t) >$ = 1.59 ± 0.04 and 2.66 ± 0.08 for 1.05 k_BT and 2.55 k_BT, respectively. At the characteristic time τ_R, $\delta(\tau_R)$ = 1.37 ± 0.19 and 2.13 ± 0.24, for the free particle.

This comparison shows that for both active energies the average dynamical enhancement of Janus particles in the crystal lattice are less than observed for Janus particles in free solution. Two-sample T-tests indicate a significant difference for both average $< \delta(\Delta t) >$ and $\delta(\tau_R)$ between free particles and particles in a crystal lattice ($p < 0.001$ and < 0.001 for average $< \delta(\Delta t) >$ and $p = 0.0016$ and 0.0053 for $\delta(\tau_R)$ for 1.05 k_BT and 2.55 k_BT, respectively).

In addition to simple statistical variability, factors which might affect whether an active particle would locomote differently in a crystal lattice than in free solution are: (a) momentum transfer from active particle to the passive crystal lattice due to collisions [58], [174]; and, (b) interactions of the phoretic field gradients of the active colloids with the crystal lattice [71], [175]. Literature support both mechanisms. To distinguish between factor (a) and (b) we note that: Factor (a) involves direct transfer of momentum from the active particle to the passive (Brownian) colloids in the crystal lattice. Factor (b) encompasses the many ways that the phoretic gradients which drive Janus particle active motion interact with the fluid-phase

boundaries of the particles in the crystal lattice. Reference [71] broadly describes these interactions as phoretic, hydrodynamic, and osmotic in nature and distinguishes them from their passive counterparts. These interactions – which can be modulated by the excluded volume, charge and potential energy of the colloidal lattice – ultimately determine the locomotive force and velocity of the active particles. Through their effect on the velocity, these interactions can affect the amount of momentum that can be transferred in (a).

In support of factor (a), Ramananarivo et al. [58] reported that the effective diffusivity of passive particles in colloidal crystals is enhanced in the presence of small fractions of active particles. Furthermore, they showed that this dynamical enhancement was related to the collision rate and speed of the active particles.

Considering factor (b), active particle motion is indeed very sensitive to local environment [75], [76], [81], [176]–[181]. For example, the speed of various catalytically-driven active particles may alternately increase [180] or decrease [174], [177], [178], [180] under confinement. An increase in speed has been attributed to a strengthening of self-generated electric fields of active particles near a channel wall and an increase in local solute concentrations when confined [180]. On the other hand, speed reduction has been attributed to chemiosmotic flows near a boundary [174], [177], [178], [180]. Different responses to confinement are linked to the specific propulsion mechanism [180]. In the present study, the particles comprising the lattice are stabilized by negative surface charges which will interact with the ion and species gradients that drive the Janus particle's active motion. These two factors support the observation of differences between $< \Delta r^2(\Delta t) >$ of the active particles in the colloidal crystals relative to free solution. We next consider if the properties of the active

particles vary with their location in the crystal lattice, here defined as located in a void, void-adjacent, or interstitial region.

3.4.3 Local variability in Janus particle concentration

Table 3-2: Fraction of Janus particles located within void, void-adjacent, and interstitial regions. The error is standard error of the mean.

	f_{void}	$f_{void\text{-}adjacent}$	$f_{interstital}$
Passive	0.12 ± 0.12	0.20 ± 0.15	0.68 ± 0.21
1.05 k_BT	0.27 ± 0.13	0.26 ± 0.14	0.47 ± 0.18
2.55 k_BT	0.19 ± 0.10	0.59 ± 0.13	0.22 ± 0.16

Table 3-2 reports the fraction of Janus particles that were detected in voids (f_{void}), void-adjacent regions ($f_{void\text{-}adjacent}$), and interstitial regions ($f_{interstitial}$). Recall that void-adjacent regions are locations within three lattice particle diameters of voids; for further details please see the Methods. The fraction of Janus particles located in voids is relatively insensitive to their active energy. Janus particles are enriched in void-adjacent regions, especially at the higher active energy tested. Their fraction changes from 0.20 ± 0.15 in the passive control to 0.59 ± 0.13 at E_A = 2.55 k_BT. On the other hand, the fraction detected in interstitial sites decreases from 0.68 ± 0.21 to 0.22 ± 0.16. Although these trends do not rise to the level of statistical significance ($p = 0.18$ for the void-adjacent case and $p = 0.29$ for the interstitial case), they do suggest that active Janus particles to some degree congregate in defect-rich areas (i.e. the void-adjacent region) rather than defect-poor areas (i.e. the interstitial region).

The small active particles of this study are effectively mobile, interstitial defects; that is, they reside in the off-lattice positions of the self-assembled colloidal crystal and can easily translate between interstitial sites because of active locomotion. Given that grain boundaries can

act as barriers to the propagation of force-driven interstitial defects, interstitial defects accumulate at grain boundaries [182]. We therefore hypothesize that void-adjacent regions accumulate active particles because they represent barriers to continued translation.

Moreover, Ramananarivo et al. [58] showed by simulation and experiment that active particles preferentially congregate at grain boundaries and other defects if the run (persistence) length of the active trajectory is less than the lattice spacing of the crystal. On the other hand, active particles with high persistence length freely propagate throughout the crystal; they do not congregate at grain boundaries. In the present study, the run lengths are 0.56 μm and 0.92 μm for 1.05 k_BT and 2.55 k_BT, respectively. They are much smaller than the lattice spacing (3.7 μm). This work, in the classification of ref [10], is therefore in the low persistence length limit. Thus, this study finds that Janus particles preferentially segregate to void-adjacent regions for low-persistence length conditions. The results are furthermore consistent with the van der Meer et al. [66] finding that active particles are attracted to defects such as voids, interstitials, and grain boundaries.

3.4.4 Local variability of embedded Janus particle microdynamics

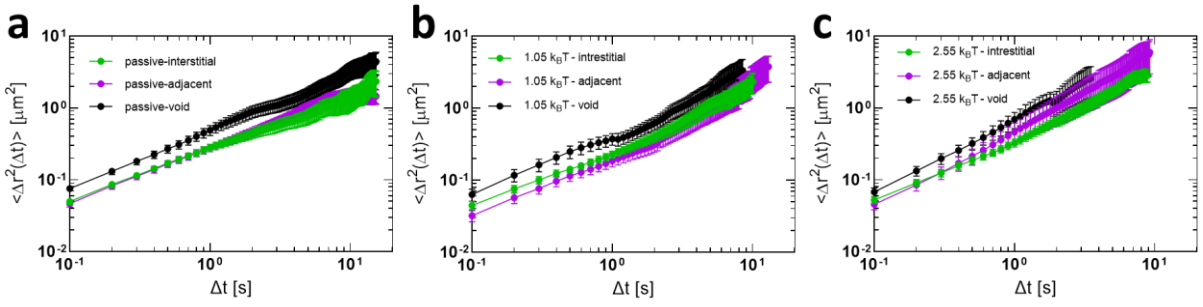

Figure 3-5: Mean squared displacements of passive and active Janus particles in crystals 900 seconds after initiating the AC field and after addition of H_2O_2, respectively. Results in (a) are for passive Janus particles in void regions, (b) are for Janus particles with E_A = 1.05 k_BT, and (c) are for Janus particles with E_A = 2.55 k_BT. Error bars are standard error of the mean.

The microstructural identification of void, void adjacent, and interstitial regions was further used to resolve the active particle microdynamics by location. Figure 3-5 reports the $< \Delta r^2(\Delta t) >$ of colloids in these regions for the three conditions of the study (passive (a), 1.05 k_BT (b), and 2.55 k_BT (c)). Janus particles in void regions display the greatest $< \Delta r^2(\Delta t) >$ in each case. In addition, in the passive case, Janus particle microdynamics in void-adjacent and interstitial regions are indistinguishable. Interestingly, as the Janus particle active energy is increased, the $< \Delta r^2(\Delta t) >$ of these two regions becomes more distinguishable. At the higher active energy (E_A =2.55 k_BT), Janus particles in void-adjacent regions are intermediate between the $< \Delta r^2(\Delta t) >$ of the void and interstitial regions.

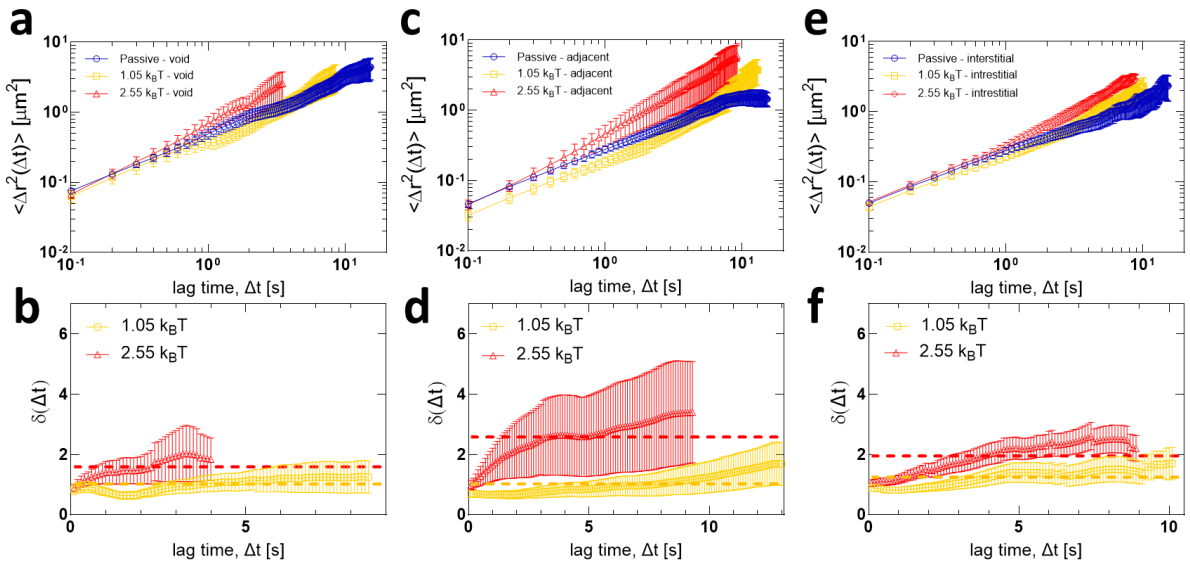

Figure 3-6: Mean squared displacements of passive and active Janus particles in crystals 900 seconds after initiating the AC field and after addition of H_2O_2, respectively. Results in (a) are for Janus particles in void regions, (c) are for void adjacent regions and (e) are for interstitial sites. Microdynamical enhancement, $\delta(\tau)$, vs lag time is in (b) voids, (d) adjacent to voids, and (f) in interstitial sites. The dashed horizontal line indicates the average enhancement across the set of lag times reported. Error bars are standard error of the mean.

To better understand this change, Figure 3-6 compares the $< \Delta r^2(\Delta t) >$ by microstructural region (voids (a), void-adjacent (c), and interstitial (e)). The accompanying $\delta(\Delta t)$ measurements are reported in Figure 3-6b, d, and f. Examining first the data for E_A = 1.05

k_BT, $< \delta(\Delta t) >$ are 1.02 ± 0.02, 1.02 ± 0.03, and 1.25 ± 0.03 for void, void-adjacent, and interstitial regions, respectively. For E_A = 2.55 k_BT, $< \delta(\Delta t) >$ are 1.59 ± 0.05, 2.58 ± 0.06, and 1.95 ± 0.05 for void, void-adjacent, and interstitial regions, respectively. A summary of measurements can be found in Table 3-3.

Of the samples with E_A = 1.05 k_BT, the statistical significance of $< \delta(\Delta t) >$ measured for each population relative to the ensemble average ($< \delta(\Delta t) >$ = 1.07 ± 0.02) is the following: p = 0.46 for the void region; p = 0.49 for the void-adjacent region; p = 0.0016 for the interstitial region.

For E_A = 2.55 k_BT, the statistical significance of $< \delta(\Delta t) >$ measured for each population relative to the ensemble average ($< \delta(\Delta t) >$ = 1.88 ± 0.04) is the following: p = 0.021 for void regions; p < 0.001 for void adjacent regions; p = 0.48 for the interstitial region.

Table 3-3: Summary of microdynamical enhancement descriptors for different activity levels. Error is standard error of the mean.

	1.05 k_BT	**2.55 k_BT**
$<\delta(\Delta t)>_{void}$	1.02 ± 0.02	1.59 ± 0.05
$<\delta(\Delta t)>_{void\text{-}adjacent}$	1.02 ± 0.03	2.58 ± 0.06
$<\delta(\Delta t)>_{interstitial}$	1.25 ± 0.03	1.95 ± 0.05
$<\delta(\Delta t)>_{ensemble}$	1.07 ± 0.02	1.88 ± 0.04
$\Sigma\ [<\delta(\Delta t)>_{region} * f_{region}]$	1.13 ± 0.3	2.25 ± 0.5

As a consistency check of these measurements, we weight the dynamical enhancement of each region by the fraction of Janus particles that occupy it and compare to the average enhancement of the whole system, as reported in Figure 3-4. Results are reported in Table 3-3. Although the errors in the average enhancement generated by weighting the three local measurements is large, no inconsistency between the local measurements and the average measurement is detected.

When E_A = 1.05 k_BT, Table 3-3 shows that the enhancements are relatively modest. That is, the dynamical enhancement of the active particles in the crystal lattice is not much greater than for passive, Brownian particles. Evidently, the collisional and chemiosmotic mechanisms described earlier are sufficient to damp the active particle trajectories so they are hardly distinguishable from the dynamics of equivalent passive particles. Given this lack of resolving power, we do not search for local effects of defect structure on active particle dynamics at this condition.

However, there is greater opportunity to resolve trends for the E_A = 2.55 k_BT condition, because the microdynamical enhancement relative to the passive control is greater. At this active energy, Janus particles experience the greatest microdynamical enhancement in the void-adjacent regions and the least enhancement in the void regions. The differences between these regions (relative to each other) are statistically significant ($p < 0.001$). Janus particles in interstitial sites have microdynamical enhancements that are intermediate between of the void and void-adjacent regions and differences are again statistically significant relative to these two regions ($p = 0.022$ and $p < 0.001$, respectively). These results show that the local crystal environment of the Janus particle influences its microdynamical enhancement relative to the passive control. Returning to Figure 3-5, the key result is that while active particles show enhanced $< \Delta r^2(\Delta t) >$ relative to the passive control in each of the three regions, the comparative effect is the greatest in the void-adjacent regions. In this region, passive particles undergo displacements that are indistinguishable from interstitial regions. However, at E_A = 2.55 k_BT, active Janus particles undergo displacements in void adjacent regions that are significantly greater than interstitial regions.

To conclude the discussion of the results, we briefly discuss possible explanations for this observation, and suggest avenues for future work. We earlier described the modes of interaction between the crystal lattice and active particles as being due to collisions and the effects of confinement on the electrodiffusiophoretic flows that drive active motion. How might these two effects lead to enhanced active particle dynamics in void-adjacent regions? First, confinement – such as an active particle with a suspension or lattice – is capable of either enhancing or dampening active motion [180]. Void-adjacent regions – because of their proximity to voids – display interstitial properties that differ from the bulk crystal, and it is these interstitial properties that determine the degree of confinement. Second, active particles in void-adjacent regions likely face reduced barriers to displacement because of their proximity to voids; the dynamics of active particles are more susceptible to these reduced barriers than less energetic passive particles. Finally, the more open structure of void-adjacent regions – with greater free volume due to their void proximity – may reduce the effect of collisions on active particle microdynamics. Fewer collisions serve to enhance active particle microdynamics relative to a greater degree than the other two microstructural regions.

3.5 Conclusions

This study demonstrated the following: (1) Void properties in self-assembled colloidal crystal monolayers are affected by the presence of dilute concentration of active Janus particles, and the degree of change is correlated with the active energy of those particles. Specifically, we find that average void area and anisotropy increase, and void number density decreases with increasing Janus particle active energy; (2) Active particles in the crystal lattice experience enhanced microdynamics relative to passive particles diffusing in the lattice. The degree of microdynamical enhancement of the Janus particles is slightly dampened in the crystals relative

to that of the active particles in free solution; (3) The fraction of active particles is increased in void adjacent regions and decreased in interstitial regions relative to passive control; (4) The microdynamics of the active Janus particles varies by location; at $E_A = 2.55k_BT$, Janus particles in void adjacent regions experience greater than the average enhancement.

Literature has demonstrated that active particles are attracted to defect regions; furthermore, the crystal lattice and the active colloids interact through collisions and the coupling of the electrodiffuisophoretic flows that drive active particle locomotion. The present observations extend these earlier demonstrations by showing that the regions adjacent to voids change active particle properties in two significant ways. First, like grain boundaries, active particles preferentially accumulate in these void-adjacent regions relative to the passive control. Second, void-adjacent regions are more conducive to active particle dynamics than other regions of the crystal. Relative to the passive control, active particles undergo enhanced displacement relative to either void or interstitial regions. Future work can assess the degree to which collisions and phoretic interactions generate these interesting properties of void-adjacent regions in colloidal crystals. Furthermore, it would be interesting to consider if there is feedback between the active microdynamics and Janus particle induced changes in void structure reported in this paper.

These findings have implications for the use of active particles to promote the annealing of crystals. For example, given the correlation of the defect structure of the passive crystal structure with the enhanced microdynamics of the active particles, it is possible that changes in void properties are mediated by the dynamical interactions that occur in void-adjacent regions. Methods to target active matter to these regions would thus promote changes in crystal defect structure. These results show that the local crystal environment of the Janus particle influences

its microdynamical enhancement relative to the passive control and that these crystal environments are themselves susceptible to microstructural change by active particles. These correlative observations suggest that mechanistic studies to understand the coupling between active particle trajectories and defect structural change in colloidal crystals are warranted.

3.6 Supplementary Material

a

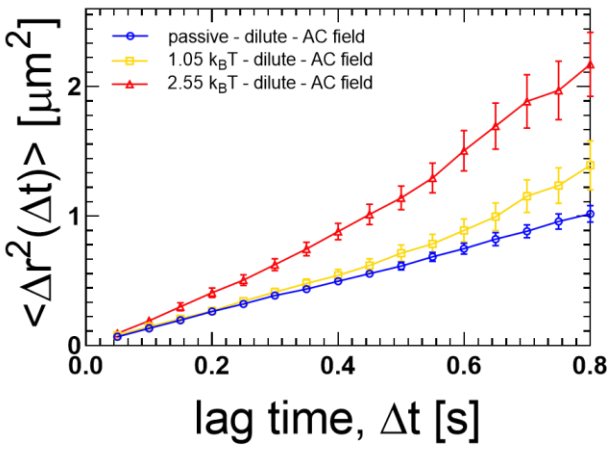

b

% H_2O_2	v (μm/s)	l (μm)	E_a $(kg*m^2)/s^2$	E_a/k_BT
1.7	0.76	0.59	4.26E-21	1.05
3.3	1.19	0.92	1.03E-20	2.55

Figure 3-7: (a) The region of the mean squared displacements of dilute passive and active Janus particles in an AC electric field (16Vrms/mm, 5MHz) used to determine the (b) velocity, run length, and active energy, E_A, inputted to the colloidal crystals at each hydrogen peroxide concentration. Error bars are standard error of the mean.

Figure 3-7 shows the microdynamics of dilute Janus particles subjected to the AC electric fields used to induce crystallization of the passive 4.0 μm colloids (16V rms/mm, 5MHz, square wave). The Janus colloid mean squared displacement $<r^2(\Delta t)>$ increases with the hydrogen peroxide concentration (Figure 3-7(a)). The amount of enhancement is quantified by fitting the mean squared displacements at short lag times [16], [125], [131] as discussed in the main text. At 1.7% H_2O_2 and 3.3% H_2O_2, Janus colloids in an AC field exhibit enhanced dynamics with an active energy, E_A, equal to 1.05 and 2.55 times that of a Brownian colloid, respectively (Fig. XX (b)), as per the analysis of Takatori et al.

The magnitude of enhancement is less than half that of previously reported values for similar particles and equivalent amounts of hydrogen peroxide [16], [42], [168], [183], but under conditions that were free of the effects of an AC electric field. This ameliorated enhancement is likely the effect of the AC electric field on the self-electrodiffusiophoretic motion of the active particle [75]. This hypothesis is plausible because the mechanism for active motion of the platinum Janus particles involves catalytically generated concentration and ionic gradients around the particle. AC electric fields can themselves induce active motion of metallodielectric particles via induced-charge electrophoresis (ICEP) or self-dielectrophoresis (sDEP, also referred to as reversed ICEP) [10], [11], [165]. At low frequencies (< ~70 kHz), particles move with the dielectric side forward via ICEP. This motion is a result of the difference in electroosmotic flow produced by the polarizability difference of the two sides [10]. At high frequencies (> ~70 kHz), particles move with the metallic side forward via sDEP (or reversed ICEP). This change in direction results because at high frequencies, the ICEP decays to zero and motion is instead dominated by the response of the particle dipole to local gradients between the substrate and wall [11], [165]. Similar mechanisms could impact the measured active velocity in the present case.

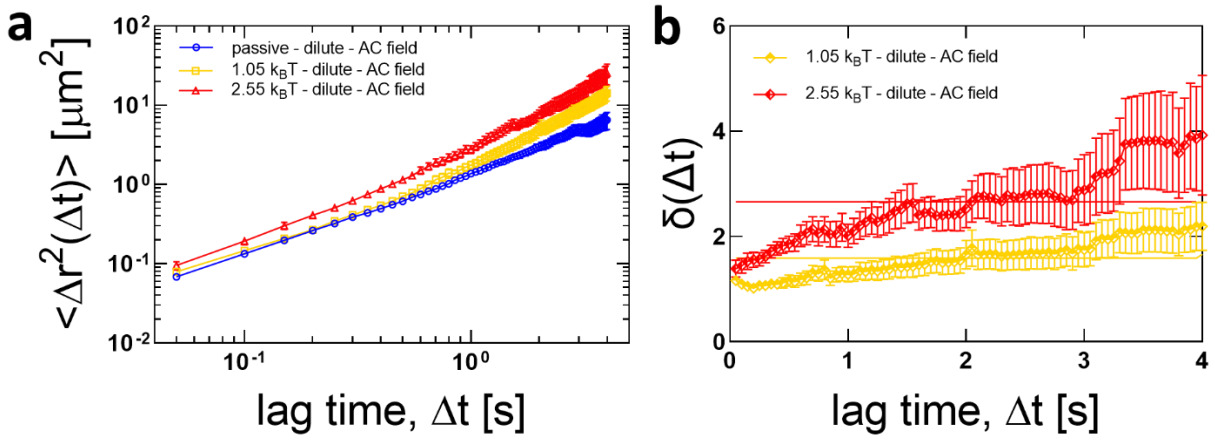

Figure 3-8: (a) The same mean squared displacements (<$r^2(\Delta t)$>, MSD) of dilute passive and active Janus particles in an AC electric field (16 Vrms/mm, 5 MHz) from Figure 3-7 but reported to longer lag times. Data are reported until the measured standard deviation of the mean squared displacement exceeds approximately 20% of the average values. (b) $\delta(\tau)$ vs lag time. In (b), the horizontal line indicates the average enhancement across the set of lag times reported which are 1.59 ± 0.04 and 2.66 ± 0.08 for 1.05 k_BT and 2.55 k_BT, respectively. Taking the rotational reorientation time ($\tau_R = 0.78\ s$) as the characteristic time, we find $\delta(\tau_R)$ = 1.37 ± 0.19 for the 1.05 k_BT case and $\delta(\tau_R)$ = 2.13 ± 0.24 for the 2.55 k_BT case. Error bars are standard error of the mean of the MSDs and $\delta(\tau)$ functions.

Table 3-4: Summary of void properties in an AC electric field assisted colloidal crystal without Janus particles before and after the addition of 3.3wt% H_2O_2 (the amount of H_2O_2 used to activate Janus particles with E_A = 2.55 k_BT).

	AC field assisted colloidal crystal (no Janus particles)	**AC field assisted colloidal crystal (no Janus particles) + 3.3 wt% H_2O_2**
Average void size (μm^2)	7.9 ± 0.07	11.0 ± 0.2
Average Void anisotropy	2.19 ± 0.03	2.51 ± 0.02
Average void number density (per mm^2)	2080 ± 50	1590 ± 40
Average void area fraction	0.0163 ± 0.0004	0.0173 ± 0.0006

Chapter 4 Electrosprayed Microparticles from Inulin and Poly(vinyl) Alcohol for Colon Targeted Delivery of Prebiotics

4.1 Abstract

Recent studies have highlighted the prebiotic effect of inulin through selective promotion of colon residing bacteria, modulation of the composition of gut microbiome, and consequent generation of beneficial effects on gastrointestinal inflammation, diabetes, and cancer. However, as a water-soluble polysaccharide, the prebiotic effect of inulin is limited by low delivery efficiency and short retention time within the colon. In this study, inulin microparticles (MPs) were produced by the electrospray method and their material properties and bioavailability were evaluated. Inulin was electrosprayed with poly(vinyl) alcohol (PVA) (MW = 89,000 – 98,000 g/mol) to improve its processability and for its mucoadhesive properties. MPs produced at PVA:Inulin mass ratio 1:3 were of diameter 0.42 ± 0.46 μm. FTIR and confocal laser scanning microscopy confirmed the presence and colocalization of the PVA and inulin in the particles. Rheologically, MP suspensions exhibited a time dependent viscoelastic response that trended toward the rheology of inulin suspensions with time. Additionally, MP suspensions exhibited greater viscosity and shear thinning behavior than their individual components and two-component mixtures. The gut retention of inulin in mice was prolonged with these MP suspensions relative to inulin suspensions and PVA-inulin two-component mixtures. The increased retention is hypothesized to be a result of the rheological change and mucoadhesive properties of PVA. The increased retention of inulin leads to improved availability of inulin for gut microbiota which can support applications in drug delivery and food.

This chapter was adapted from a publication that is in preparation: K. T. Saud, J. Xu, S. Wilkanowicz, Yue He, J. J. Moon, and M. J. Solomon, “Electrosprayed microparticles from inulin and poly(vinyl) alcohol for colon targeted delivery of prebiotics,” Keara T. Saud, Jin Xu, Sabina Wilkanowicz, and Michael J. Solomon conceived this research and designed the experiments. Keara T. Saud conducted the experiments for rheological characterization. Keara T. Saud and Jin Xu performed further materials characterization. Jin Xu and Yue He conducted the animal studies.

4.2 Introduction

Inulin is a fructan polysaccharide that occurs naturally in many foods such as leeks, asparagus, onion, garlic, and chicory [101]. It is commonly used in the food industry to replace sugar or fat and to modify rheological properties [184]–[188]. Inulin is a dietary fiber which is not digested in the stomach and small intestine, but instead is metabolized by commensal bacteria in the colon. Consuming prebiotics such as inulin has been associated with a number of health benefits including stimulation of the immune system, production of beneficial metabolites, and reduced allergy risks [101], [102], [189], [190].

Recent studies suggest that the formulation of inulin affects its prebiotic efficacy. Specifically, when administered in a gel form inulin exerts synergistic effect (as compared to inulin suspensions) with immune checkpoint blockade therapy in various murine tumor models [94]. The effect is generated through modulation of the gut commensal microorganisms and was explained by the increased inulin retention in the colon when gelled and the resulting increased probiotic bacteria and short chain fatty acid (SCFA) production [94]. Wahbi et al. also show that the formulation of inulin affects its properties. They electrospun inulin into composite nanofibers with polyvinyl alcohol (PVA) and found that the nanofibers increased the prebiotic activity by

38% compared to their suspension counterparts. Here inulin suspensions, inulin gels, and inulin nanofibers primarily differ in the physical forms: specifically, the microstructures and surface area-to-volume ratios. Inulin suspensions lack any network microstructure and have a small surface area-to-volume ratio relative to nanosized samples. In contrast, inulin gels have a microstructure responsible for their modified and more solid-like rheological properties; and inulin nanofibers have a much larger surface area to volume ratio.

In addition to gel, nanofiber, and suspension formulations, inulin can also be made into microparticles (MPs) via several techniques including electrospraying, spray drying, and solvent-precipitation [191]–[194]. Inulin in particle form has been studied for targeting of the colon [191], [194]. This form has additionally been studied for the encapsulation of bioactive molecules as well as in conjunction with bioactive molecules to improve molecule stability and viability [192], [195], [196]. However, how this particle form affects inulin's gut retention properties has not been the subject of systematic study. Understanding how particle form affects its gut retention would provide further insights into how we may improve bioavailability and prebiotic benefits of inulin.

The first portion of this paper describes the creation and characterization of the material properties of inulin MPs while the second portion of the paper examines inulin gut retention *in vivo* when delivered as a MP formulation. The MPs are prepared via electrospraying with PVA. Electrospraying is a form of electrohydrodynamic processing (EHDP) that is inexpensive and scalable; it also produces MPs reproducibly and under benign processing conditions. Because inulin is not electrosprayable as a pure component [194], inulin has been blended with PVA for successful spraying. PVA is biocompatible, of low toxicity, and used in FDA-approved medical products. It additionally exhibits mucoadhesive properties when highly hydrolyzed [197] and

readily dissolves in solvents that are non-hazardous. It is also well-studied and commonly used for electrospraying, including inulin [190], [198]–[202]. To simulate the oral dosage form for *in vivo* studies in mice, the resulting inulin MPs are characterized in the following ways: 1) morphology and size distribution in dry and hydrated states; 2) chemical composition and the localization of these components; 3) transient and steady-state rheology when suspended in water, and 4) inulin release profile. We correlate these properties with the results of inulin gut retention studies *in vivo* to better understand bioavailability in the gut.

4.3 Experimental section

4.3.1 Materials

PVA (Mw = 89,000 – 98,000 g mol^{-1}, 99% hydrolyzed), inulin from chicory, FITC-inulin, ethanol, glacial acetic acid (AA), and fluorescein isothiocyanate (FITC) were purchased from Sigma Aldrich. Cyanine5 (Cy5) and Cyanine7 (Cy7) amine were purchased from Lumiprobe. Fructan assay kit was from Megazyme.

4.3.2 Fluorescence conjugation of inulin and PVA

PVA was labeled with FITC following the procedure published by [203]. Briefly, PVA (2.5 g) was dissolved in DMSO (66.6 mL) and pyridine (416.6 μL) under stirring at 80 ˚C for 24 h. FITC (83 mg) and dibutiltin dilaurate (31 μL) were added to the PVA solution and the reaction was carried out for 2 h at 95 ˚C in darkness. The crude product was precipitated and washed with IPA, followed by dialysis against DEMI water and lyophilization.

Cy5-inulin or Cy7-inulin conjugates were synthesized using the method described by [204]. In brief, Carboxymethyl inulin (CMI) was first produced by dissolving 500 mg inulin in 2M NaOH, added with 276 mg chloroacetic acid, and heating to 70˚C for 75 min. The solution

was neutralized with acetic acid after cooling and CMI was precipitated by cold ethanol. Resulted CMI (40-50mg) was activated in 10mL 1M equivalent of NHS and EDC for 1.5 h. The activated CMI solution was subsequently added dropwise to Cy5/Cy7-amine (Lumiprobe) (10-15 mg, 12.2-18.3 μM), dissolved in dimethyl sulfoxide (DMSO). The conjugation of the dye to CMI was allowed to proceed for 24 h at room temperature, in the dark with shaking. Dialysis was carried out (Float-a-Lyzer, Spectrum Labs, Phoenix, AZ) against water, and the resulted solution was lyophilized until dry powder was obtained.

4.3.3 Preparation of mixtures for electrospraying

A stock solution of 5.0 wt% PVA in H_2O/AA/Ethanol (84/6/10 by volume [199]) was weighed and dissolved in a 70 $^{\circ}$C oven overnight. Inulin suspensions made with 15 wt% inulin in ultrapure H_2O were prepared and left in a 40 $^{\circ}$C water bath for 20 minutes. For confocal laser scanning microscopy (CLSM) and IVIS imaging (described below), PVA solutions and inulin suspensions were prepared by adding FITC-PVA and Cy7-inulin in the ratios of 1:9 and 1:19 to the unconjugated forms, respectively.

Following dissolution, equal parts PVA solution and inulin suspension were combined resulting in a final mixture concentration of 2.5 wt% PVA and 7.5 wt% inulin in H_2O/AA/Ethanol (91/3.4/5.6 by volume [199]). This was the minimum concentration of PVA that resulted in sustained, successful MP production. For pure PVA particles, 6.0 wt% PVA in H_2O/AA/Ethanol (84/6/10 by volume [199]) was combined with equal parts ultrapure water. Each newly combined sample was well mixed before further characterization or use in EHDP.

4.3.4 Characterization of mixtures for electrospraying

The conductivity of PVA solutions and PVA-inulin mixtures used for electrospraying was measured using a compact conductivity meter (EC 11, Horiba). Rheological properties were measured using an Anton Paar MCR 702 rheometer at 20 °C. PVA solutions were measured in a cone and plate configuration ($\theta = 2^{o}$, 50 mm in diameter). PVA-inulin mixtures were measured in a parallel plate configuration (50 mm in diameter) with 600 grit sandpaper adhered to the rheometer tooling to mitigate any potential for wall slip. The viscosity is measured and reported at the high shear limit of $\dot{\gamma} = 100\ s^{-1}$ [205], [206]. Data points were log spaced. Measurements at a given shear rate were performed until the viscosity was constant with an allowance of 1% and the signal was averaged for the last 0.5 s. PVA-inulin mixtures were allowed to rest quiescently for 1 hr to achieve a steady state (Figure 4-10). The surface tension of the prepared mixtures was measured using an optical goniometer (Rame-hart Instrument Co., Drop Image Advanced software). All measurements were performed in triplicate at a minimum.

4.3.5 Microparticle production via electrospraying

The EHDP equipment was assembled in a horizontal configuration with a high voltage power supply (P030HP2M, Acopian) and a digital syringe pump (KDS100, KD Scientific). This equipment is contained in a covered plastic box to reduce photo bleaching and to minimize changes in relative humidity. After the polymeric mixture was prepared, it was loaded into a disposable syringe (Becton Dickinson) with an 18-gauge stainless steel needle. The syringe was attached to the pump so that the tip-to-collector distance was approximately 12 cm. The steel collector plate is covered with standard aluminum foil. One electrode is attached to the needle and the other attached to the collector plate. The pump is set to a flow rate of 0.5 mL/hr for PVA-inulin mixtures, 0.4 mL/hr for fluorescently labeled PVA-inulin mixtures, and 0.4 mL/hr for

pure-PVA solutions. The voltage was adjusted between 21-25 kV to achieve a stable Taylor cone. The collection time varied between 3 hrs – 18 hrs.

4.3.6 Fluorescence conjugation of inulin and PVA

Morphological characterization of MPs

Scanning electron microscopy (SEM; Tescan MIRA3) was used to characterize the size and morphology of electrosprayed MPs. Specimens were sputter-coated with gold. An operating voltage of 5 kV and an average working distance of 9.7 mm were used. Images for morphological analysis of dry MPs were captured at 35kx magnification. Images for size analysis of dry MPs were captured at 20kx magnification. Particle size analysis of the electrosprayed inulin-PVA MPs was performed by measuring the particle diameter with ImageJ. If the particle was not perfectly spherical, the largest diameter measurement was taken. In all cases, a minimum of 900 particles from three random parts of the sample were analyzed to determine size distributions.

Hydrated size distribution

A Malvern Mastersizer 2000 with Hydro 2000S wet dispersion unit was used to measure the hydrated particle size distribution of the MPs. Samples were dispersed in water with equivalent inulin concentrations of 180 mg/mL and gently mixed. After 30min, samples were added to the chamber, with the stirring speed at 1750 rpm and sonication on. Data were analyzed using the following parameters: particle refractive index was set equal to 1.50 and the dispersant was taken as pure water.

Fourier transform infrared (FTIR) spectroscopy

FTIR spectroscopy (Jasco FTIR-4100) was used for chemical composition analysis and comparison of the prepared MPs with their pure components. Samples were prepared by filling the instrument well with powders of pure PVA, pure inulin, or PVA-inulin MPs. Spectra were collected with 1 cm^{-1} resolution and an average of 64 scans over a spectral range of 4000 - 500 cm^{-1}. Spectra were normalized and examined by Spectra Manager software.

Confocal Laser Scanning Microscopy (CLSM)

An inverted confocal laser-scanning microscope (CLSM) (Nikon A1Rsi equipped with NA = 1.4, 100x objective) was used to examine the dry and hydrated MPs as well as the hydrated inulin suspension. The MPs to be imaged were prepared with FITC-PVA and Cy5-inulin as described in section 2.3. The inulin suspensions to be imaged were prepared with FITC-inulin (Sigma Aldrich) at a ratio of 1:9 to the unconjugated form of inulin. Two channels were used: the Cy5-inulin was imaged with a 641 nm excitation and an emission band from 663 to 738 nm and the FITC-PVA and FITC-inulin were imaged with a 488 nm excitation and an emission band from 500 to 550 nm.

Samples of dry PVA-inulin MPs were imaged in an 8-well plate (Thermo Fisher Scientific). For studies of hydration kinetics, inulin as-received or PVA-inulin MPs were suspended in ultrapure water at a concentration equivalent to those used in the rheological characterization, as described in Section 2.8. Specifically, 180 mg/mL and 240 mg/mL were used, respectively. After combining material with water, samples were vortexed mixed briefly for homogeneity. Immediately following, they were added to their respective imaging containers and mounted onto the microscope. Inulin suspensions were imaged in a sealed 8-well plate and

PVA-inulin MP suspensions were imaged in a smaller device to conserve sample. The smaller device was made with a silicone spacer (1 mm thick and 4.5 mm in diameter, Grace Biolabs) adhered on a glass slide, and sealed. Images were taken at approximately t = 0 s, 1800 s, 3600 s, 7200 s, and 14400 s at a constant height of 5 μm above the coverslip. Swelling, aggregation, and any evolution with time were examined.

4.3.7 Inulin release study

120 mg PVA-inulin MPs were weighed and dispersed in 5 mL simulated intestinal fluid (SIF without Pancreatin, USP 26). The dispersion was incubated at 37˚C, 400 rpm. 100 μL samples were collected at the desired time point and 100 μL fresh buffer was replenished immediately. Samples were centrifuged at 20,000g for 5 min to remove undissolved particles. Supernatants were collected, and inulin concentration was measured by the Fructan Assay Kit (Megazyme, K-FRUC).

4.3.8 Rheological characterization of MP suspensions and PVA-inulin mixtures

Characterization of the transient and steady state rheology of PVA-inulin MP suspensions was performed and compared to that of four controls: PVA MP suspensions, PVA solutions, inulin suspensions, and two-component mixtures all made with equivalent concentrations of PVA and inulin. All samples were prepared as for gut retention studies, and as described in section 2.9. Briefly, MPs and control mixtures were prepared in ultrapure water at a fixed concentration of 180 mg/mL inulin and 60 mg/mL PVA. For PVA-inulin MPs, this corresponded to 240 mg MPs/mL. For PVA MPs, this corresponded to 60 mg/mL. For inulin suspensions, this corresponded to 180 mg/mL of inulin. For PVA solutions, preparation was conducted by dissolving PVA in water (60 mg/mL) at 70°C. For the two-component mixture, the following

was performed: first, the required amount of PVA (60 mg/mL PVA) was dissolved in water at 70°C. Then the required amount of inulin (180 mg/mL) was added to the PVA solution. After preparation, all samples were well vortexed and left in a 37°C water bath for 30 minutes to fully disperse either the MPs, the inulin, the PVA, or the two-component mixture. Samples were allowed to rest at room temperature for approximately 10 minutes before loading in the rheometer.

An Anton Paar MCR 702 rheometer was used with Peltier temperature-controlled plate and hood at 20˚C. A smooth 50 mm cone and plate geometry ($\theta = 2^{o}$) was used for PVA solutions. 25 mm and 50 mm parallel plate geometries were used for MP suspensions and two-component mixtures, respectively. 600 grit sandpaper was adhered to the parallel plate fixtures to address wall slip and a solvent trap was used to minimize sample evaporation. A study of the effect of gap at h = 500, 750, and 1000 μm was performed with the PVA-inulin MPs; it revealed no gap dependence of the rheological properties (Figure 4-12). A 500 μm gap was used for all rheological measurements.

We measured the time-dependent linear viscoelastic moduli ($\omega = 1$ rad/s, $\gamma = 0.04\%$) of samples for a duration of four hours (Figure 4-11 shows linear regime). Following these four-hour time sweeps, two rheological tests were performed. First, the frequency-dependent linear viscoelastic moduli were measured from $\omega = 0.1 – 100$ rad/s ($\gamma = 0.04\%$). Next, the steady-state viscosity was measured as a function of shear rate over the range 0.1 to 300 s^{-1}. Data points were log spaced. To achieve steady-state, measurements at a given shear rate were performed until the viscosity was constant with an allowance of 1% and the signal was averaged for the last 0.5 s. All data is collected with at least 3 replicates.

4.3.9 Gut retention studies

For the *in vivo* imaging of gut retention, Cy-7 labeled inulin was added in the PVA-inulin MPs as described in Section 4.3.5 or was added to inulin suspensions in 1:19 for the other control groups. MPs, inulin, and PVA-inulin mixtures were orally administered to BALB/c mice at the dose of 36 mg inulin per mouse, five mice in each group, and images were taken every two hours under anesthesia. Fecal pellets were collected every 2.5 hours. Images were acquired and analyzed using IVIS Lumina Living Image Software (v.4.5.5).

For fecal inulin quantification, mice were fed on alfalfa-free diet (AIN-93M) 24 hours before experiment to minimize interference of fructose derived from food. Then PVA-inulin MPs and equal amounts of inulin or inulin with PVA were suspended in water and administered to BALB/c mice by oral gavage. Fecal pellets were collected every 2.5 hours and homogenized in water. The resulting fecal slurry was boiled for 10 min and centrifuged at 20,000×g for 10 min at 4˚C, subsequently. The supernatants were collected and measured for inulin concentration by the Fructan Assay Kit (Megazyme, K-FRUC) according to the manufacturer's instructions.

4.4 Results and Discussion

4.4.1 Properties of mixtures for electrospraying

Table 4-1: Conductivity, viscosity, and surface tension, of electrosprayed material mixtures

	Conductivity (µS/cm)	Viscosity (cP)	Surface tension (mN/m)
PVA	709 ± 0.7	37.8 ± 2	57.3 ± 0.06
PVA:Inulin	620 ± 1	198 ± 5	52.5 ± 0.04

The mixtures electrosprayed are described in section 2.3. To summarize, the final materials were 3.0 wt% PVA and, separately, 2.5 wt% PVA and 7.5 wt% inulin in H_2O/AA/Ethanol (91/3.4/5.6 by volume). These concentrations and solvents were optimized for

MP production rather than beaded fiber or fiber production. From Table 4-1, the addition of inulin to the mixture caused an increase in the viscosity, reduction of conductivity, and slight reduction of surface tension. How these differences in properties may affect the particles produced will be discussed in section 4.4.2

4.4.2 Particle size, size distribution, and morphology

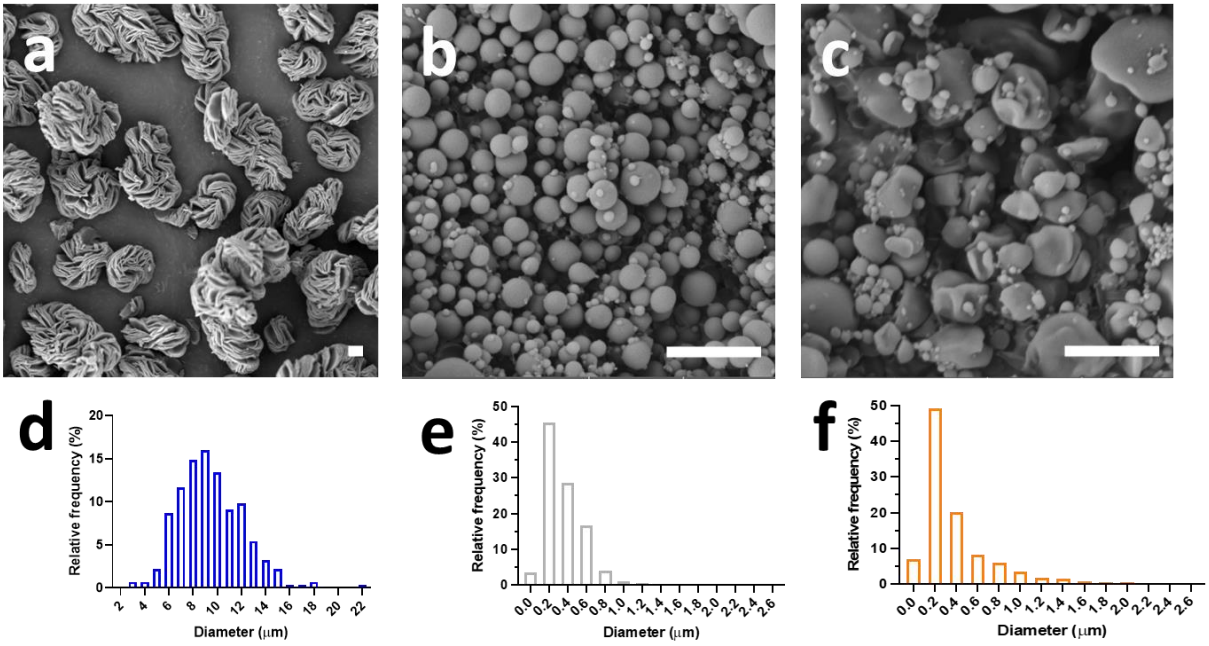

Figure 4-1: Scanning Electron Microscopy and size distributions of dry inulin as-received (a & d), electrosprayed MPs made of pure PVA (MW = 89,000-98,000 g/mol) (b & e), and electrosprayed MPs made of PVA (MW = 89,000-98,000 g/mol) and inulin at a ratio of 1:3 (c & f). All micrographs were taken with a voltage of 5.0 kV, a working distance of ~10 mm, beam intensity of 8.00. The scale bars are 2 μm.

The SEM images in Figure 4-1 show the as-received inulin and the production of MPs with varying diameter and shape. The as-received inulin (Figure 4-1(a)) has an average diameter of 9.5 ± 2.7 μm and layered surfaces leading to a less spherical shape. MPs made of PVA (Figure 4-1(b)) had an average diameter of 0.35 ± 0.22 μm (error is standard deviation) and were the most spherical. MPs made of 1:3 PVA-inulin (Figure 4-1(c)) had an average diameter of 0.42 ± 0.46 μm, respectively (error is standard deviation), and were more non-spherical than the pure

PVA MPs. The presence of inulin in the microparticles correlated with a significant increase in average diameter, as evidenced by the 2-sample t-test ($\alpha = 0.05$, $p = 0.000012$). However, the PVA-inulin MPs are still an order of magnitude smaller than the as-received inulin.

The particle size dispersity is compared using the coefficient of variation, $Cv = \sigma/\mu$, where σ is the standard deviation and μ is the average particle size [199]. The Cv is 0.29, 0.63, and 1.10 for the as-received inulin, pure PVA MPs, and PVA-inulin MPs, respectively. The presence of inulin in the MPs is correlated with an increase in the size dispersity. This increased MP size dispersity can also be demonstrated by the maximum diameters of MPs. The maximum observed diameter for the PVA-inulin MPs was 5.2 μm, while that of the pure PVA MPs was 2.1 μm.

We hypothesize that the incorporation of inulin generates several effects. First, the PVA-inulin mixtures had a lower conductivity and a higher viscosity than the pure PVA solutions. Both these characteristics can contribute to greater particle sizes and size dispersity [199], [207], [208]. Indeed, we observe such a correlation given the observed average particle size of the two different materials.

Flow rate is another parameter that can influence the particle size and size distribution. Greater flow rates typically result in larger particles and increased size distribution [209], [210]. Although only a modest change (25%), the greater flow rate used for PVA-inulin mixtures (0.5 mL/hr) compared to the pure PVA solutions (0.4 mL/hr) could also be contributing to the greater size distributions.

The PVA MPs made here are about half the average size and 50% more polydisperse than a prior report in the literature [199]. The operating conditions of the present study relative to this study are the following: the flow rate is higher (0.4 mL/hr vs 0.3 mL/hr or less); the needle

diameter is larger (18 gauge vs 24-25 gauge); and the voltages are higher (21-25 kV compared to ~10 kV). The smaller size is consistent with the larger voltages used in this study. Larger voltages can lead to smaller particles because of the greater strength of the drawing force relative to the surface tension [199], [210]. Moreover, the polydispersity has been reported to increase with increased flow rate and increased needle diameter because of the increased presence of multiple jets, yielding multiple particle production sites at the outlet rather than a single site as associated with just one jet [209]–[212]. High voltages can also lead to broader size distributions because of destabilization of the electrospray jet [199].

4.4.3 Chemical composition by FTIR

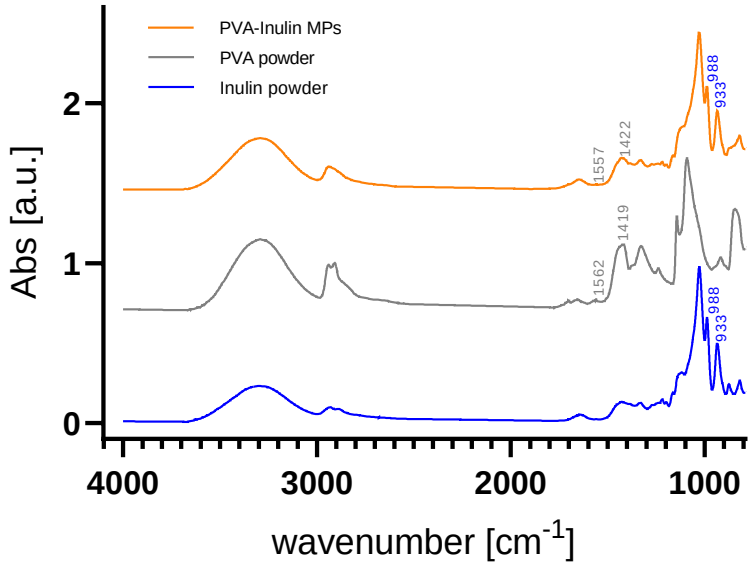

Figure 4-2: FTIR spectra for PVA-inulin microparticles compared to their primary components: PVA powder and inulin powder

As reported in Figure 4-2, the FTIR spectrum of inulin shows two peaks at 988 and 934 cm^{-1}. These peaks are associated with the C-C and C-O stretching as well as C-O-H and C-O-C

deformation modes of oligo- and polysaccharides, as previously discussed in [213] and [214]. These peaks are not present in the as received PVA powder but are present in the PVA-inulin MP spectrum, confirming the presence of inulin in the MPs. The spectrum of the PVA powder shows peaks at ~1420 and ~1560 cm^{-1}, representing O-H and C-H bending, respectively. These peaks are not apparent in the as-received inulin powder but are present in the PVA-inulin MP spectra. These results therefore confirm the presence of PVA in the MPs.

4.4.4 Confocal laser scanning microscopy (CLSM) assesses colocalization of PVA and inulin

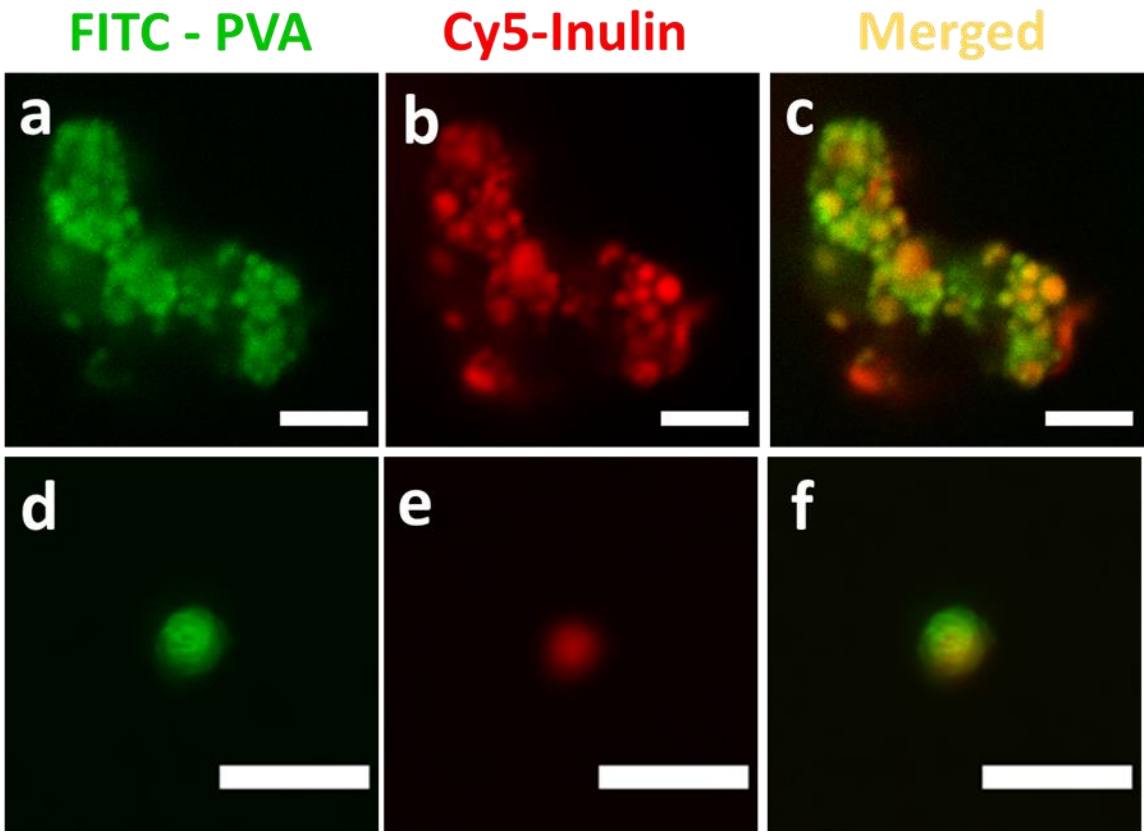

Figure 4-3: Confocal laser scanning microscopy images of dry electrosprayed FITC-PVA:Cy5-Inulin MPs. (a) & (d) shows the FITC channel only; (b) & (e) shows the Cy5 channel only; (c) & (f) shows combined FITC and Cy5 channels. The scale bar for (a) - (c) is 5 μm while that of (d) - (f) is 2 μm.

PVA/inulin MP size and sphericity, as assessed from confocal microscopy images of the fluorescently labeled MPs (Figure 4-3) are similar to the SEM micrographs of Figure 4-1. We

observed colocalization of PVA (green, Figure 4-3 a and d) and inulin (red, b and e) within each particle, rather than sequestration of materials into separate particles. When observing a single MP (Figure 4-3(d-f)), this colocalization is apparent. From these confocal microscopy images and FTIR data, we conclude that both inulin and PVA are co-dispersed within the individual particles.

4.4.5 Microparticle Hydration

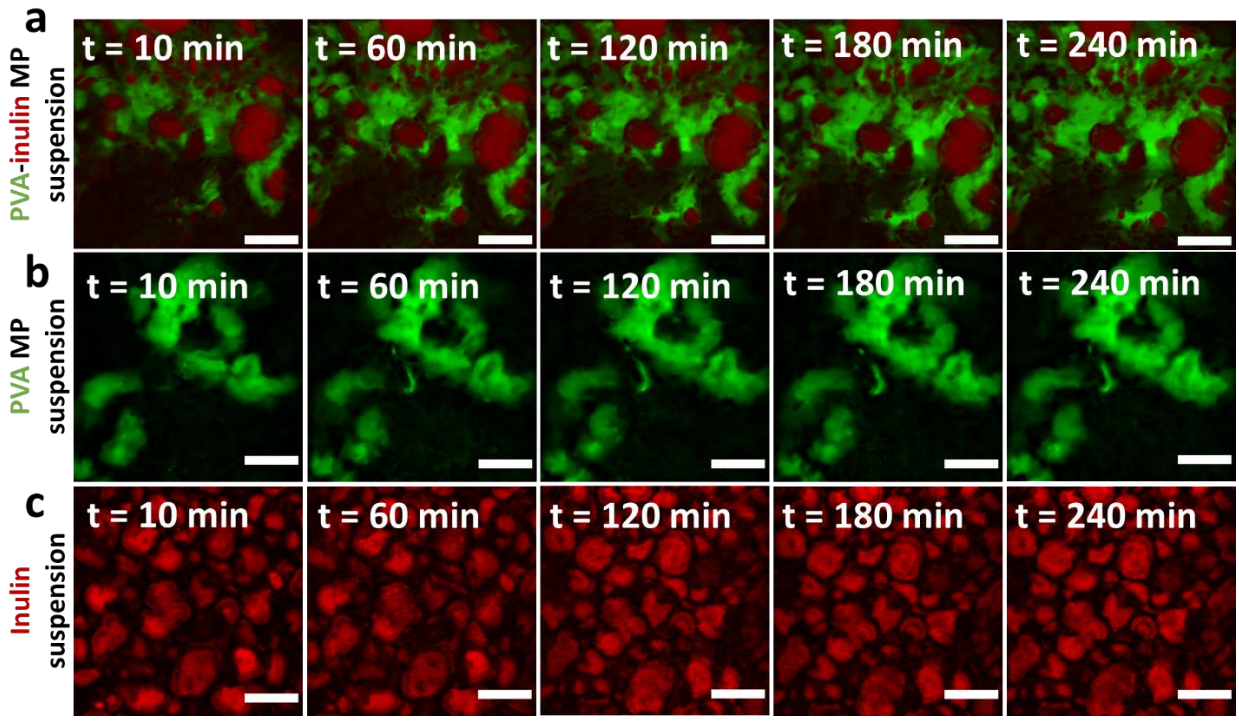

Figure 4-4: Confocal laser scanning microscopy images of the time evolution of (a) an electrosprayed FITC-PVA:Cy5-Inulin MP suspension, (b) an electrosprayed FITC-PVA MP suspension, and (c) a FITC-inulin suspension. PVA and inulin are displayed in green and red, respectively. Images were taken at the same location at different times after mixing with water, scale bar = 10 μm.

Confocal microscopy images were acquired to characterize the hydration of the particulate microstructure of inulin, PVA MP, and PVA-inulin MP suspensions. The duration of the measurements is comparable to the typical GI transit time in mice, as given in the IVIS imaging study below and by [215] and to the rheological measurements discussed subsequently.

The initial few minutes of the time evolution of these concentrated samples could not be captured due to experimental set up time which included sample mixing, loading, and sealing of the device.

The images reveal the following. For the PVA-inulin MPs (Figure 4-4(a)), we observe particle swelling and aggregation as well as some PVA dissolution. In this hydrated state, inulin and PVA appear to have sequestered: the particles are mostly inulin (red) and are dispersed in and around a PVA (green) matrix. The PVA matrix here appears to be partially dissolved and spread throughout the sample in this hydrated state. Furthermore, these swelled, aggregated particles remain stable for longer than 4 hours as shown here.

The control sample of PVA MPs in Figure 4-4(b) additionally shows partial dissolution and swelling of the PVA. Spherical particles are not distinct. However, the remaining undissolved PVA remains stable for longer than four hours. In comparison, the other control, the as-received inulin suspension (Figure 4-4(a)), exhibits little to no swelling or aggregation of the inulin particles. Nevertheless, these particles are still slightly larger and more dispersed through the sample than the those in PVA-inulin MP suspension. This inulin suspension sample also remains stable for longer than the four hours.

It is interesting to compare these measurements to the characterization of the single, dry MPs as reported in Figure 4-1. The colocalized PVA and inulin observed in the dry state becomes sequestered in the hydrated state. Additionally, the MP form of the PVA is no longer distinct in the hydrated state. Through these transitions, we learn that the PVA is likely encapsulating the inulin. Furthermore, Figure 4-4 suggests that any rheological change that occurs in the sample in this time period is occurring on the molecular or polymeric level because very little microstructural change is visible with confocal microscopy.

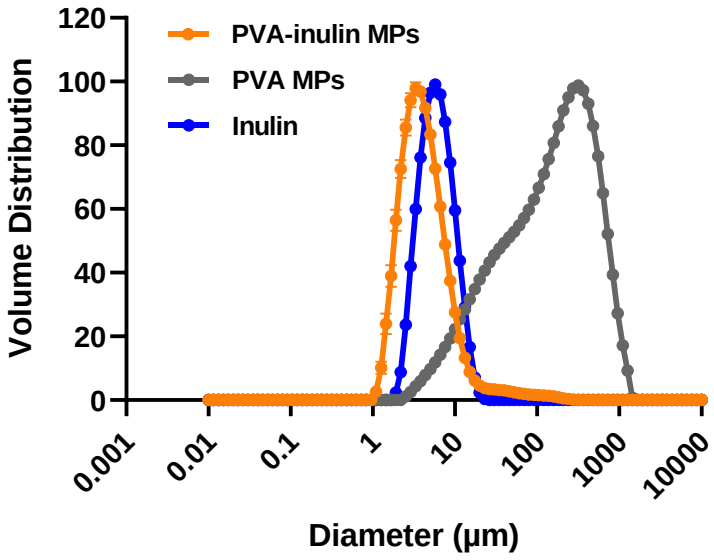

Figure 4-5: Size distributions of as-received inulin, PVA MPs, and PVA-Inulin MPs in their hydrated state after 30 minutes of exposure to water in the dilute regime. Generated by Jin Xu.

The diameter of the PVA and PVA-inulin MPs and the as-received inulin were measured after exposure to water for 30 minutes in the dilute regime (Figure 4-5). The dilute condition is expected to exaggerate the swelling effects relative to the confocal images shown above due to increased solvation. Under these hydration conditions, an increase in particle size is observed for the MPs relative to the dry particle sizes, as reported in Figure 4-1. Specifically, the most probable diameter of the PVA MP increases by three orders of magnitude to 316 µm; the most probable diameter of the PVA/inulin MPs increases by one order of magnitude to 3.3 µm. On the other hand, the as-received inulin does not experience a significant change in particle size when hydrated (most probable diameter ~ 7.8 µm). These data confirm the size difference between hydrated inulin and hydrated PVA-inulin MPs observed in the confocal images in Figure 4-4.

We thus observe that the particle whose size increases contain PVA. That is, the observed greater swelling for the PVA MPs here and lack of significant swelling of inulin suggest PVA controls the size change with hydration. This difference in swelling is likely related to the

difference in hydrophilicity of the two polymers. PVA is very hydrophilic and will swell more in water [216] while inulin is known to be more hydrophobic and will swell less or not at all [188], [217].

MP agglomeration may contribute to the greater size, as described in other systems [218]. Partially dissolved PVA could be contributing to the larger measured sizes of PVA MPs and PVA-inulin MPs. There is some evidence for such partial dissolution in the confocal microscopy images of Figure 4-4.

4.4.6 Rheological characterization of microparticle suspensions

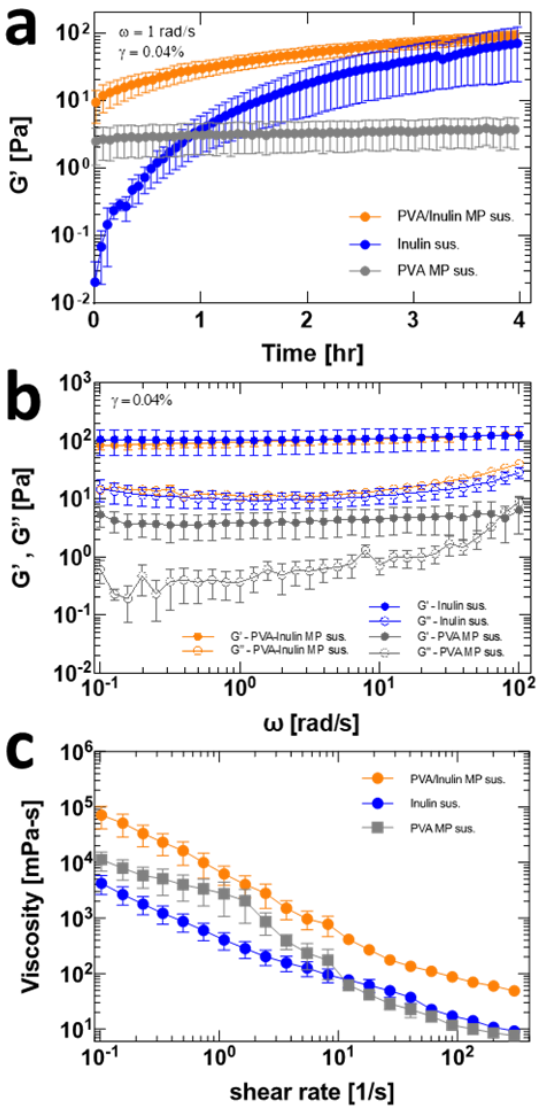

Figure 4-6: (a) Time dependent linear elastic modulus over 4 hrs (γ = 0.04% and ω = 1 rad/sec); (b) Frequency dependence of linear viscoelastic moduli (t = 4 hr, γ= 0.04%) and (c) Shear-rate dependent viscosity (t = 4 hr, $\dot{\gamma}$ = 0.1 to 300 s-1) of PVA-inulin MP suspensions and pure inulin suspensions.

Rheological properties of the PVA/inulin MP suspensions as administered in the *in vivo* studies are compared to that of PVA MP and as received inulin suspensions in Figure 4-6. For this study, t = 0 s is after 30 minutes of incubation. This incubation time was used to conform to timing in the mice experiments discussed later.

The duration of the transient measurements shown in (a) is comparable to the typical GI transit time in mice, as given in the IVIS imaging study below and by [215]. The linear elastic

modulus of the PVA/inulin MP suspension increases by about a factor of ten over the duration of the experiment. The elastic modulus of the inulin suspension control grows over a time comparable to the PVA-inulin MPs; however, the level of increase is much greater; the elastic modulus of this material grows by a factor of about one thousand. In contrast, the PVA MP suspensions have an elastic modulus that is nearly independent of time. Moreover, with time, the elastic modulus of the PVA-inulin MP suspensions tends towards that of the as received inulin suspensions rather than that of the PVA MP suspensions.

The frequency-dependent linear viscoelastic moduli reported in Figure 4-6(b) were collected at the conclusion of the kinetic measurements reported in Figure 4-6 (a). The results are consistent with convergent rheological properties of the PVA/inulin MPs and the inulin control. That is, the linear viscoelastic moduli of these two materials are indistinguishable from each other. The moduli of the PVA-MPs are lower than the other two samples.

The shear-rate dependent viscosity of the three specimens shows shear thinning behavior (Figure 4-6 (c)). There is no evidence of a plateau viscosity at either high or low shear rates. Generally speaking, typical shear rates found in the digestive tract are between 0.1 s^{-1} and 10 s^{-1} [93], [219], [220]. The PVA-inulin MP suspensions display the greatest viscosity for this entire physiologically relevant range of shear rates. Inulin suspensions on average display the lowest viscosities and pure PVA MP suspensions display viscosities in between the other two samples. The shear thinning character of the PVA-inulin MP and inulin control are similar. The PVA MP curve differs; there are two regimes of shear thinning behavior.

A scenario that explains these data is the following: the elastic modulus is most sensitive to the release and hydration of inulin while the shear rate dependent viscosity is sensitive to both MP form and the presence of inulin. Here MP form refers to physical form and structure that

results from this form in the suspended state. The sensitivity of the elastic modulus to inulin is most apparent from Figure 4-6 (a) where the pure inulin suspension experiences the greatest modulus increase with time. Furthermore, the convergence of the moduli of the pure inulin suspensions with PVA-inulin MP suspensions suggests that inulin is the common feature that dominates the viscoelastic response.

To investigate this further, we first compared the rheology of PVA-inulin MP suspensions to that of PVA-inulin two-component mixtures (shown in Figure 4-13). These data show that the PVA-inulin MP suspension initially has a greater modulus than the equivalent two-component mixture. However, with time, these two samples evolve towards the same behavior which, again, converges to the pure inulin suspension (Figure 4-6 (b)).

Next, we evaluate the effect of the MP form alone on rheological behavior by looking at pure PVA solutions and pure PVA MP suspensions. Figure 4-14, shows that the MP form does in fact cause an increase in the viscoelastic moduli of the PVA in both the transient and frequency-dependent response. However, this modulus remains about constant with time and frequency, suggesting that the elastic modulus is not dominated by the MP form. Together, these data indicate that the MP form initially dominates the transient viscoelastic behavior, but this influence lessens with time and a transition occurs to a long-time regime that is dominated by the inulin contribution.

The features that dominate the strain rate dependent viscosity can be similarly evaluated from Figure 4-6 and from Figure 4-13 and Figure 4-14. First, Figure 4-6 (c) shows that all samples have non-Newtonian shear thinning behavior where the magnitude of the viscosities of the PVA-inulin MP suspensions is almost additive of that of the pure PVA MP and inulin suspensions. These results suggest that both inulin and MP form influences this behavior.

Inspecting this further, instead of the Newtonian shear rate independent viscosity that is typical of PVA solutions (Figure 4-14), the pure PVA MP suspensions have non-Newtonian shear thinning behavior. This result suggests that despite the lessening effect on the viscoelastic behavior, the MP form contributes to the shear thinning behavior of the sample. PVA-inulin two-component mixtures and PVA-MP suspensions both show shear thinning behavior. However, PVA-inulin MP suspensions show greater shear thinning. Therefore, inulin affects the strain dependent viscosity but to a lesser extent than the MP form.

Summarizing these rheological results, the rheological response of the PVA-inulin MP suspensions shows the effects of both MP form and the presence of inulin. The inulin was observed to be more influential for the viscoelastic behavior at long times. The MP form contributed more to the short time viscoelastic behavior as well as the increased viscosity and shear thinning behavior. As we try to connect the rheological properties with their microscopic behaviors, discrepancies can be found and reveal more information about the samples. Rheologically, all inulin-containing suspensions change over the 4-hour measurement. However, from confocal microscopy, none of the suspensions show visual changes in this time period. It is worth noting that the many small particles observed in the dry state from SEM are not found in the hydrated state. The hydrated size distributions (Figure 4-5) confirm the lack of these smaller particles suggesting that they are likely dissolved. Because only the inulin-containing samples show the increasing rheological trends and inulin suspensions are visually observed to gel over four hours, we hypothesize that the interactions of dissolved inulin led to the gelling of inulin and is responsible for the rheological changes.

4.4.7 Inulin release profile

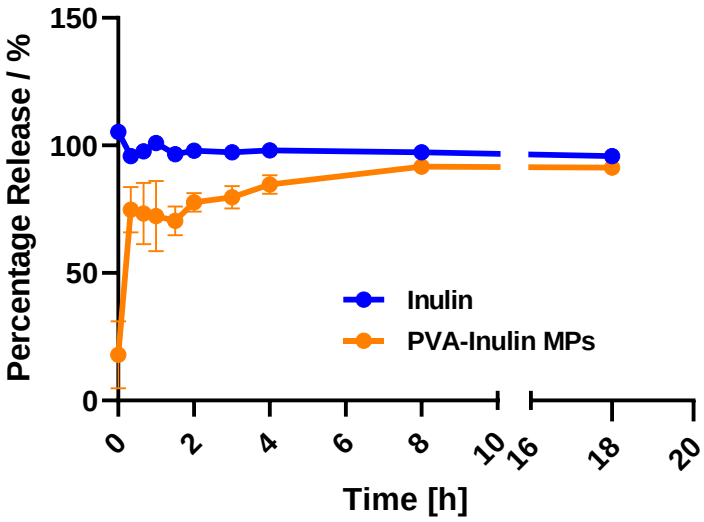

Figure 4-7: Release profile of inulin from the microparticles compared to inulin as-received. Generated by Jin Xu.

The inulin release profile in the simulated intestinal fluid (SIF) of the PVA-inulin MPs is compared to inulin as-received in Figure 4-7. This figure indicates that the MPs follows a burst release profile of inulin. More specifically, in the first two hours, ~70% of inulin is released from the PVA-inulin MP suspensions. Additionally, the PVA-inulin MP suspensions attain steady-state after approximately 500 min. Even though this *in vitro* assay is expected to display faster release of inulin than the rheological experiments (Figure 4-6) because of the different environments (diluted in SIF compared to constant concentration in DI water, respectively), the release profile shows a time scale that is comparable to the kinetics in the transient rheological response of Figure 4-6 (a). This correspondence suggests that the release of inulin may be impacting the kinetics of the transient rheological response of the PVA-inulin MP suspension.

4.4.8 Gut retention study

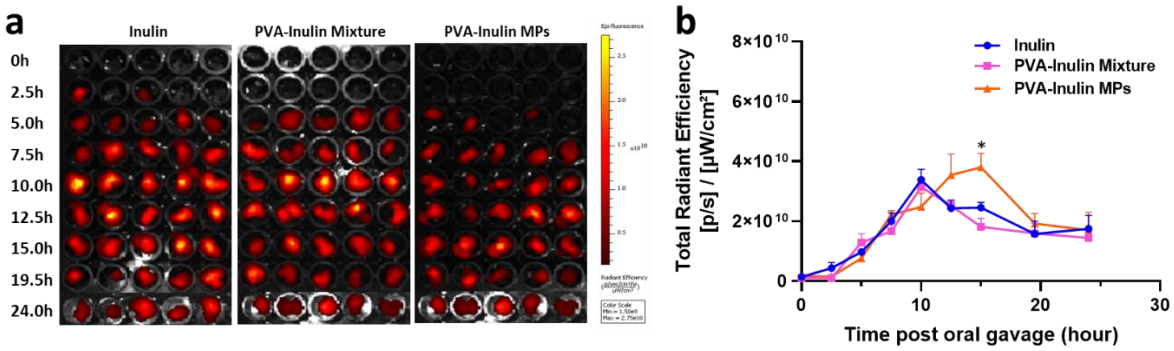

Figure 4-8: Gut retention study of PVA-inulin MPs. Mice were orally gavaged with Cy7-labelled inulin, PVA-Cy7-Inulin mixture or Cy7-MPs, and fecal samples were collected at indicated time points (a) Images of fecal pellets collected and (b) normalized fluorescence intensity of the feces, quantified from (c) (N=5). Generated by Jin Xu.

Retention of inulin in the gastrointestinal tracts of mice was first evaluated by live animal imaging (Figure 4-17). Cyanine 7-conjugated inulin was added to the PVA-inulin MPs, PVA-inulin mixture, and inulin as-received in the 1:19 ratio to native inulin. The fluorescence-labeled formulations were fed to mice via oral gavage, and fecal samples were collected and imaged to measure the Cy7-inulin signals (Figure 4-8). The onset of inulin excretion was at 5.0 hours for most mice. This suggests an overall GI transit time of 5 hours, consistent with the literature [215] and the conditions in the rheological characterizations. The fluorescent intensity reached the peak at 10 hours for inulin and PVA-inulin mixture. In comparison, the maximum signal for the PVA-inulin MPs was seen after 15 hours (Figure 4-8). This remarkable delay indicates that the formulation of microparticles travels slower in the GI tract than free inulin and the simple PVA-inulin mixture, which could essentially improve the availability of inulin for gut residing microbes, as is evidenced by measuring the area under the curve of the Total Radiant Efficiency from fecal samples (Figure 4-16). It needs to be noted that this extended gut retention was not identified in the live imaging of the mouse abdomen region because the method cannot differentiate the various segments of GI tract when the stomach and intestines are naturally

arranged in mice. Furthermore, the delay in colon transit may be overwhelmed by the overall fluorescence signals along the GI tract, leading to negligible difference.

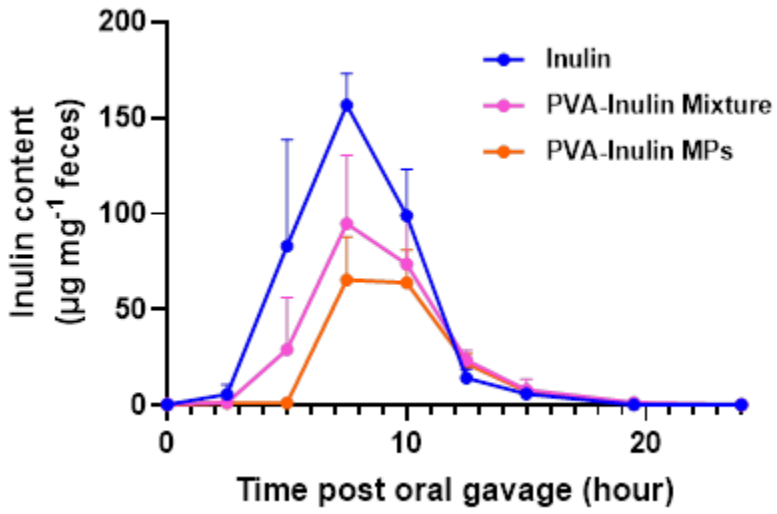

Figure 4-9: Fecal inulin content of mice over 24 hours after oral administration of as-received inulin, PVA-inulin mixture, and PVA-inulin MPs. Generated by Jin Xu.

In order to confirm the prolonged colon retention of MPs, the inulin excretion kinetics in the feces was also evaluated, shown in Figure 4-9. The inulin content measured is the total amount of long-chain inulin remaining in the feces and excludes degraded fructose from inulin. We first note that the as-received inulin and PVA-inulin mixture reached the highest fecal concentration by ~7.5 hours while the PVA-inulin MPs reached its maximum by around 10 hours. This delayed peak for the PVA-inulin MPS further supports the enhancement of colon retention by the microparticles. These data also show a reduction of the total amount of inulin present in the feces for the PVA-inulin mixture and PVA-inulin MPs - the greatest reduction being for the MPs. This reduction can be explained by the inulin assay kit used and the fact that it only measures long-chain inulin remaining in the feces. The colon fermentation is expected to break down the polysaccharide and generate fructose from inulin, therefore reducing the amount of long-chain inulin present [221]. Consequently, the lower inulin content detected in the fecal

samples from PVA-inulin mixture and MPs treated mice can be attributed to the extended transit times that allows more sufficient fermentation.

Comparing the feces quantification from these two studies (Figure 4-8 and Figure 4-9), some similarities and differences can be seen. Both quantifications show later appearance of peak inulin content for the MPs suggesting enhanced colon retention. However, there is an approximate 2.5 hours delay in the transit time in the live animal imaging (Figure 4-8b) compared to the direct measurement of inulin (Figure 4-9). This delay may be ascribed to the frequent anesthesia performed in mice when acquiring the live images. It has been reported that inhalation anesthesia may disrupt the normal gastrointestinal motility [221], [222]. Additionally, the reduction of inulin content for PVA-inulin mixture and MPs in Figure 4-9 suggests more of the inulin in these samples are being fermented, further supporting the enhanced colon retention. This reduction is not observed from the fluorescence quantification in Figure 4-8, where the fluorophore persists even when the conjugated inulin is degraded.

These results can be explained by the mucoadhesive properties of the highly hydrolyzed PVA [197], [223] and the increased viscosity/moduli of the sample described in section 4.4.6 and 4.6. Essentially, these two features of the MP suspensions could be contributing to an increase in bioavailability of the inulin fermentation by colon residing bacteria (Figure 4-9 and Figure 4-16). It is interesting to note that the trends in gut retention between these three samples align with the trends in viscosity at the physiological shear rates (0.1 s^{-1} and 10 s^{-1}) [93], [219], [220]. Specifically, the greatest gut retention of inulin, as quantified here, occurred with the sample with the greatest viscosity at shear rates = 0.1 s^{-1} - 10 s^{-1} (PVA-inulin MP suspension); the least gut retention of inulin occurred with the sample with the lowest viscosity in this regime (inulin suspension). A direct comparison of these samples is given in the SI. Further animal studies

could investigate the gut microbiome composition and changes in the levels of metabolites such as SCFAs, which could provide more insights into specific prebiotic effects of these modified inulin. Nonetheless, this colon targeting and sustained formulation is a promising strategy to modulate host microbiome in multiple diseases applications.

4.5 Conclusions

In conclusion, inulin was successfully electrosprayed into microparticles by blending it with a PVA solution at a ratio of 1:3 PVA-inulin by weight. The MP form and presence of inulin had significant effects on rheological properties when suspended in water. The rheological differences between samples were seen in both oscillatory shear and steady shear tests: inulin containing samples had greater viscoelastic moduli and greater viscosities. When administered to mice and compared to inulin as-received and PVA-inulin mixtures, PVA-inulin MP suspensions resulted in greater colon retention as given by fecal quantification and IVIS imaging. We conclude that this response is correlated with the modified rheological properties of microparticles and mucoadhesive properties of the PVA used. These results can be useful for the design of colon targeted products in both food and biomedical applications, especially for the gut microbiome modulation through prebiotics.

4.6 Supplementary information

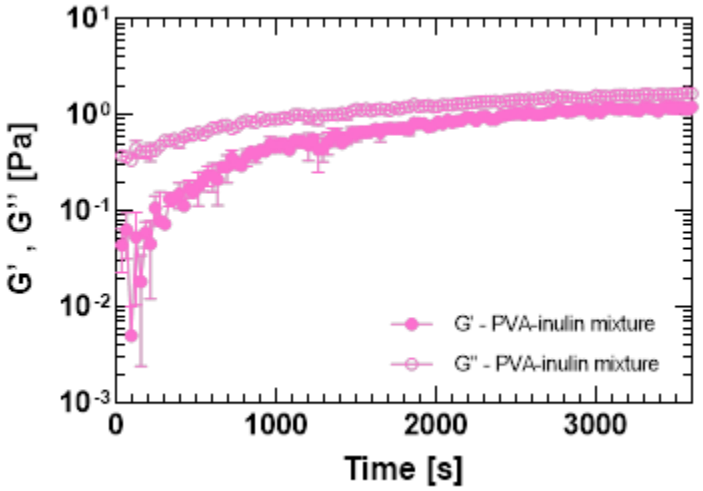

Figure 4-10: Electrosprayed PVA-inulin mixtures are allowed to rest for 1 hr before measuring viscosity because of the time needed to reach steady state behavior as shown in this figure. Frequency is 1 rad/s.

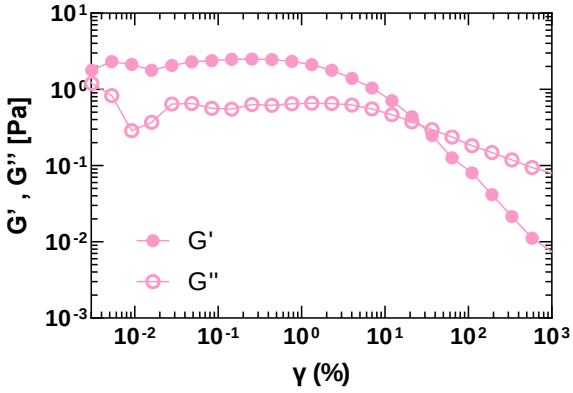

Figure 4-11: Oscillatory strain amplitude sweep of microparticle suspensions (frequency = 1 rad/s). A strain amplitude of 0.04% is shown to be in the linear regime.

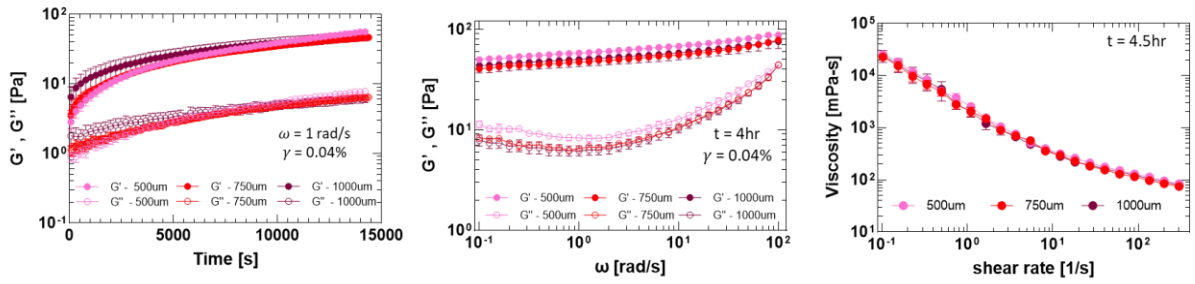

Figure 4-12: A rheological study to determine the presence of any gap effects with the microparticle suspensions. Time sweeps, frequency sweeps, and flow curves at 500um, 750um, and 1000um show no significant gap effects and so 500um gap was used to conserve sample.

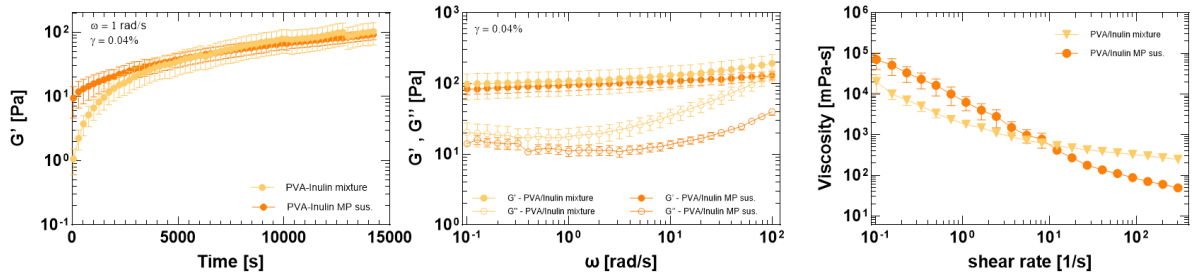

Figure 4-13: Time dependent linear elastic modulus over 4hrs (γ = 0.04% and ω = 1 rad/sec); Frequency dependence of linear viscoelastic moduli (t = 4 hr, γ= 0.04%); and shear-rate dependent viscosity (t = 4 hr, $\dot{\gamma}$ = 0.1 to 300 s-1) of PVA-inulin MP suspensions and PVA-inulin mixtures. Mixtures begin with higher viscoelastic moduli, but values converge with those of the MP suspensions in less than an hour. Both samples are shear thinning but MP suspensions display greater shear thinning. At most physiologically relevant shear rates (0.1 s^{-1} and 10 s^{-1}) [93], [219], [220], *MP suspensions have a greater viscosity than mixtures.*

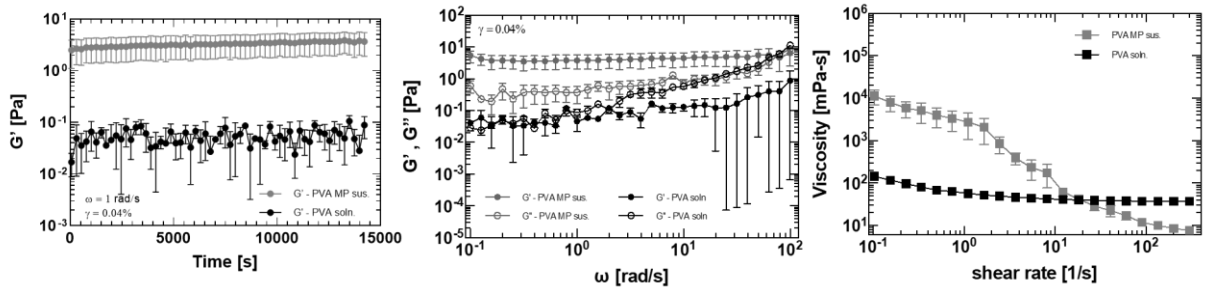

Figure 4-14: Time dependent linear elastic modulus over 4hrs (γ = 0.04% and ω = 1 rad/sec); Frequency dependence of linear viscoelastic moduli (t = 4 hr, γ= 0.04%); and shear-rate dependent viscosity (t = 4 hr, $\dot{\gamma}$ = 0.1 to 300 s-1) of PVA MP suspensions and PVA solutions. MP suspensions have greater viscoelastic moduli than PVA solutions. However, no time dependence of these moduli are observed for either MP suspensions or solutions. PVA solutions are Newtonian and do not show shear rate dependence. However, PVA MP suspensions show shear thinning behavior.

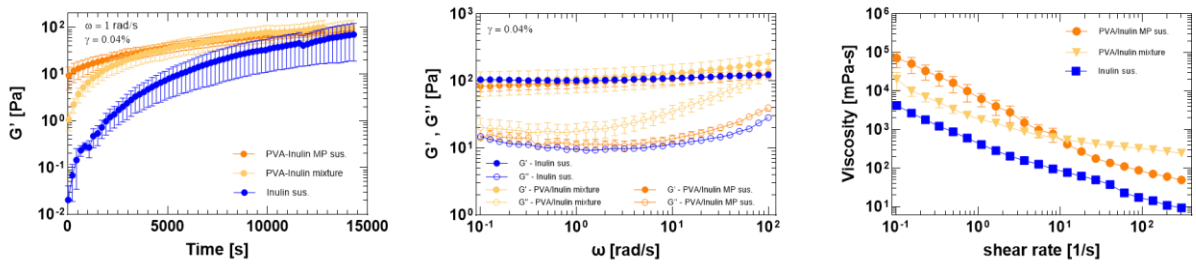

Figure 4-15: Time dependent linear elastic modulus over 4hrs (γ = 0.04% and ω = 1 rad/sec); Frequency dependence of linear viscoelastic moduli (t = 4 hr, γ= 0.04%); and shear-rate dependent viscosity (t = 4 hr, $\dot{\gamma}$ = 0.1 to 300 s-1) of PVA-inulin MP suspensions, PVA-inulin mixtures, and inulin suspensions. This figure shows the convergence of the viscoelastic moduli of these three samples. However, shear rate ramps show a difference in their viscosities. All samples are shear thinning. Inulin suspensions have the lowest viscosities at all shear rates. At most physiologically relevant shear rates (0.1 s^{-1} and 10 s^{-1}) [93], [219], [220], *PVA-inulinMP suspensions have a greater viscosity than mixtures of equivalent concentrations.*

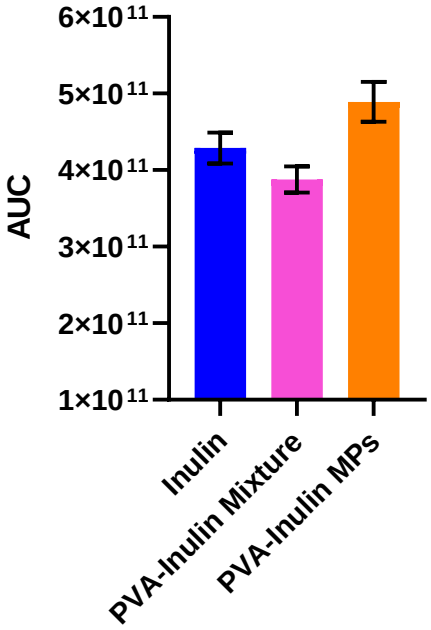

Figure 4-16: Area under the curve of the Figure XX in the main text. These data show PVA-inulin MPs have the greatest area. Generated by Jin Xu.

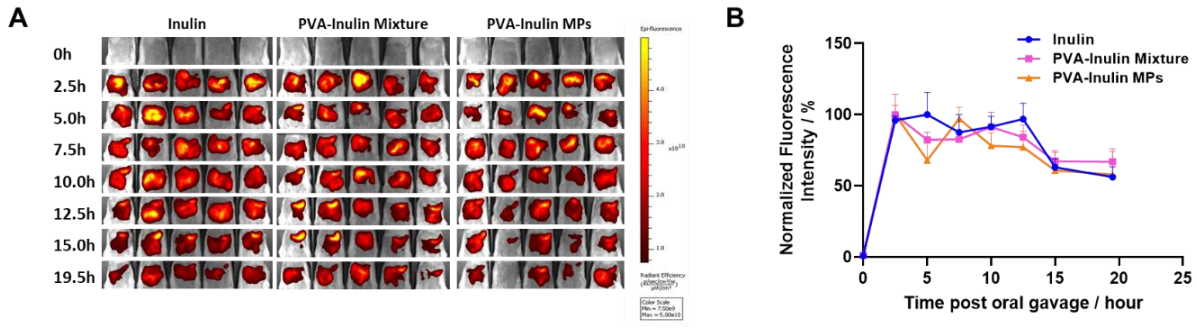

Figure 4-17: Gut retention study of PVA-inulin MPs. Mice were orally gavaged with Cy7-labelled inulin, PVA-C7y-Inulin mixture or Cy7-MPs. (a) Images of gastrointestinal tracts were acquired through IVIS imaging system at indicated time points and (b) normalized fluorescence intensity of the GI tract area, quantified from (a).) The fluorescent signal persisted in the abdomen area for up to 12.5 hours and then started to decrease in all tested formulations. No statistical difference was observed among groups, suggesting the GI transit time is comparable at individual levels by the endpoint of live animal imagine. Fig XX(b) provides quantification of the fluorescent signals in the abdomen area from Fig. XX(a), which demonstrates similar patterns of inulin clearance for all inulin formulations. Extended gut retention was not identified in the mouse live imaging results, because the method cannot differentiate the various segments of GI tract when the stomach and intestines are naturally arranged in mice. Furthermore, the delay in colon transit may be overwhelmed by the overall fluorescence signals along the GI tract, leading to negligible difference. Generated by Jin Xu.

Chapter 5 Conclusions and Future Work

The overarching objective of this dissertation was to explore how specific types of colloidal particles affect and interact with various environments. Specifically, I examined how active colloids affect the yield stress behavior of colloidal gels and interact with defect-rich colloidal crystals. I also investigated how electrospraying PVA-inulin microparticles affect the gut retention of inulin as mediated by their dissolution and rheological properties.

5.1 Effects of active motion

Active particles have a complex motion that can both influence and be influenced by its environment [71], [76], [174]. In this dissertation, we specifically studied platinum Janus particles whose motion results because of the asymmetric decomposition of hydrogen peroxide across the particle [16], [75]. We looked at how this motion manifested itself when embedded in colloidal gels and ultimately how it affected the yield stress behavior of colloidal gels. We additionally examined how this motion affected void properties and was affected by microstructural regions in defect-rich colloidal crystals. The next two subsections summarize these studies in more detail.

5.1.1 Rheological implications in colloidal gels

In Chapter 2, we probed how embedded active particles affect the yield stress behavior of colloidal gels. Colloidal gels were made through diffusion limited cluster aggregation (DLCA) by the addition of magnesium chloride, a divalent salt. These gels have been well studied and have established structure-property relationships [35], [224]–[226]. As such, they are a model system for studying how active particles may interact with and affect them. The active particle

used was a platinum Janus particle which self-propels as a result of the asymmetric decomposition reaction of hydrogen peroxide at the particle surface. This active particle is well studied and established in the literature [17], [19], [21], [75] making it an ideal candidate for the active particle system used.

Previously, it had been shown that embedded active particles cause a reduction of their viscoelastic moduli [20]. Because the yield stress of a gel is also critical for its use and performance [104], [111], we performed three yield stress measurements to understand implications of embedded active particles on this nonlinear rheological parameter: start up of steady shear, oscillatory strain amplitude sweeps, and creep compliance tests. Due to interference that can occur from the bubble formation that results during the decomposition reaction, two important procedural modifications were instituted that allowed for successful rheological measurements: (1) highly oxygen permeable polydimethyl siloxane (PDMS) plates were used to act as an oxygen trap and (2) an antifoaming agent was used to suppress bubble formation. In the active energy regime tested, all three measurements demonstrated that active particles cause a reduction of the yield stress. Furthermore, the start-up and steady shear and strain amplitude tests revealed that active energies studied cause no significant change in yield strain. This finding, as well as structural characterization with confocal microscopy and the radial distribution function, suggest that the activity level studied did not affect the gel structure.

To explain how the small fraction of active particles could have the profound effect that was observed, we hypothesized that active clusters rather than active particles drive the reduction of rheological properties. We used this hypothesis for the modeling of the gel mechanics. Furthermore, because no structural change was observed, modelling focused on the elastic

modulus, which if determined, would then allow the yield stress to be estimated. We found that the modulus reduction was well predicted by this theory of cluster activation.

These results have important implications for the future design of active gels. First and foremost, they show how a small number of active particles can have a profound rheological effect. They additionally suggest that gels with tunable rheological properties could be realized through the use of active particles. Both implications would be desirable in industry if implemented correctly. For example, in many cases dramatically changing a product formulation is not realistic. However, tunable rheological properties are still desired for different parts of the manufacturing process. Active matter could provide a route for just that: few particles are needed to impart a large rheological change on an existing structure; and such a change can be implemented through the simple addition of hydrogen peroxide or exposure to the specific activity-inducing field (i.e. chemical gradient, light, electric field, etc.).

Further study and incorporation of other active matter systems is needed to realize this potential though. For example, further insights into the mechanism for active motion as well as the importance of the placement of active particles within the gel is needed to understand and properly implement. To better understand the potential impact of these features, the author suggests two potential approaches: (1) systematically comparing the motion in three locations of a colloidal gel: clusters that contain an active particle, clusters that are close to an active particle, and clusters that are far from a particle; and (2) systematically studying the motion of fractal clusters (not within a gel) of different sizes that do and do not contain an active particle.

For approach (1), one would be confirming cluster activation and better understanding the length scale that the active force is experienced by active particles. Some initial attempts to take this approach were made. However, the small fraction of active particles present made it

challenging to locate and resolve the active particles in the gel. This small fraction therefore led to inconclusive results. Increasing the active particle fraction could help address this challenge, but as previously noted, higher fractions caused the formation of oxygen bubbles from the decomposition reaction. For approach (2), some initial attempts were also made. Fractal clusters were prepared by adding magnesium chloride to a solution of active particles and a much smaller concentration of passive particles. Though this smaller passive particle concentration meant that the system would not gel (see figure in Chapter 1), it also made it challenging to locate these clusters. In the future, preparing these dispersions in a device with a smaller volume (for example by using a spacer with a smaller thickness), could allow for easier location of clusters. However, we would encounter a competition between bubble formation if the device were sealed and sample evaporation if the device were left open.

Because bubbles interference prevented the use of higher concentrations of active particles or higher active energies (via hydrogen peroxide concentration), the full extent of the impact of active particles on colloidal gels could not be realized. For example, Omar and colleagues predicted higher active energies would change gel structure [70]. One possible way to experimentally access higher active particle concentrations or energies while maintaining low overall concentrations would be to use 2D colloidal gels. 2D gels would still allow for a fundamental understanding of how active particles effect gel structure. Another way to access higher active particle concentrations or energies would be to use a different active motion mechanism that does not produce a gaseous byproduct. One promising active mechanism is induced charge electrophoresis of metallodielectric particles in AC electric fields [10], [11]. This motion not only has no gaseous byproduct but also has the potential to reach higher active

energies [77]. Figure XX shows typical trajectories of this motion in 4 μm platinum Janus particles (25 nm Pt) in water from an AC electric field applied perpendicularly to the substrate.

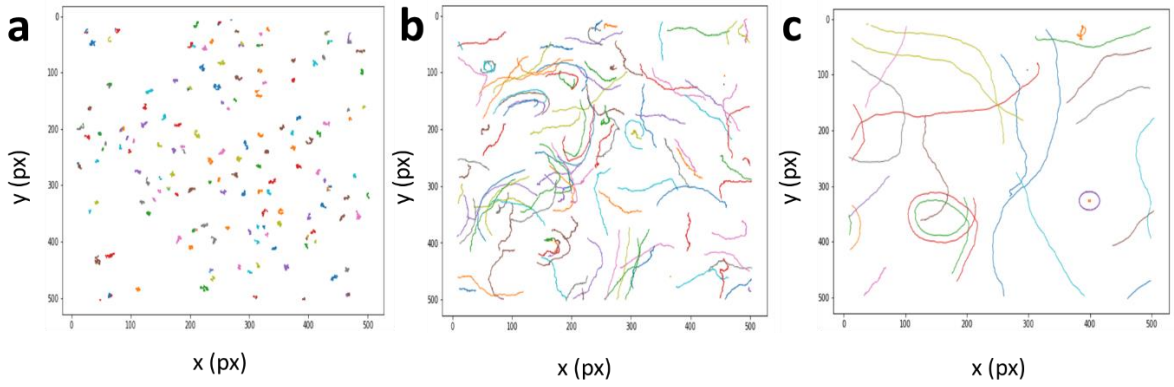

Figure 5-1: Trajectories of 4 μm platinum Janus particles (25nm Pt) in DI water with an AC electric field strength of (a) 0 V/cm, (b) 100 V/cm, and (c) 200 V/cm. The electric field was applied perpendicularly to the substrate made of ITO slides and a spacer with varying thickness. Pixel-micron ratio is 0.25 μm/px

Two disadvantages of this mechanism include that it: (1) is largely hindered by the presence of salt [10] which is needed for the creation of DLCA gels and (2) is usually a quasi-2-dimensional phenomenon because of the inherent attraction to the wall or substrate in an AC electric field [227] and particle sedimentation that occurs from the high density of the metallic side [11].

With these advantages and disadvantages in mind, some initial attempts were taken to incorporate these active particles into gels. Quasi-2D gels were used to account for Janus particle sedimentation. Furthermore, depletion gels (rather than DLCA gels) were used to diminish the reduction of active motion from salt. As described in Chapter 1, depletion gels form because a polymer depletant acts to maximize its entropy by pushing larger colloidal particles together [1]. At a high enough concentration of both the depletant and colloidal particles, gelation can occur. Examples of two 2D depletion gels made using polyethylene oxide (PEO – Mv = 600,000 g/mol) and sodium carboxymethyl cellulose (NaCMC – Mv = 70,000 g/mol) as depletants are shown in figure XX.

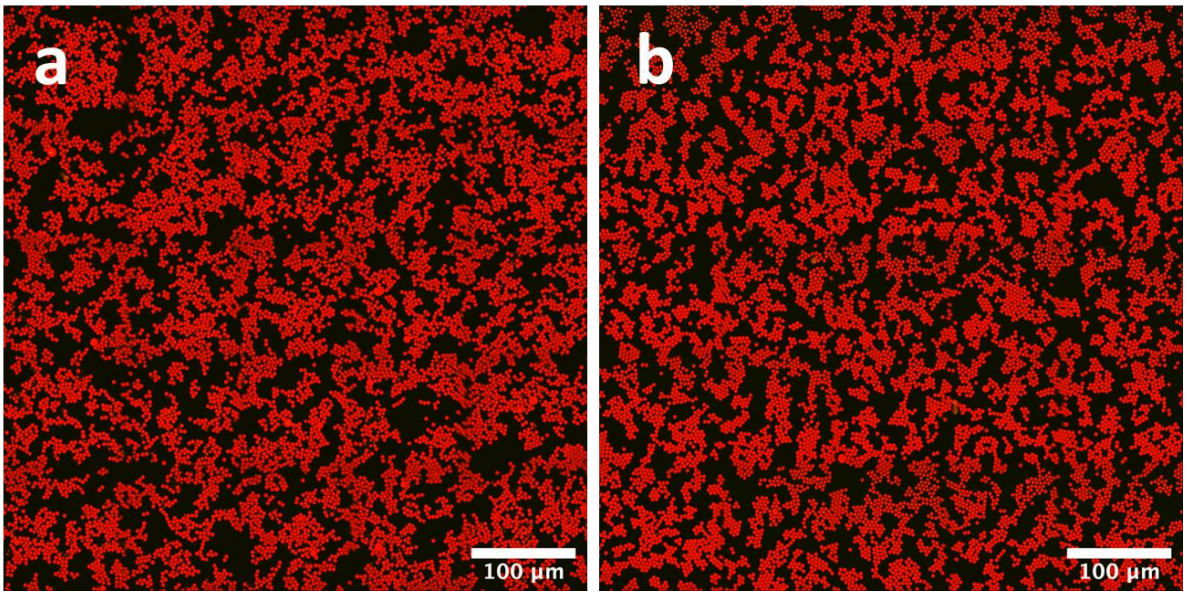

Figure 5-2: 2D depletion gels made in a sealed 8-well plate (200 □L/well) with 0.036 vol% 4 µm PS particles and (a) 1.0 g/L PEO and 1.5mM NaCl or (b) 0.9 g/L NaCMC. Gels were imaged here after 3.5 day.

Though 2D gels were successfully made, when active Janus particles were incorporated, the AC field induced Janus particle sticking almost immediately. This sticking is likely the result of depletion forces, the greater van der Waal forces of the metallic side [149], and small salt concentration. Many attempts to prevent Janus particle sticking in this environment were made, including exposure or coating of the substrate with (1) oxygen plasma for 20 minutes [228], [229], (2) 1-10 wt% bovine serum albumin (BSA) solution [230], (3) a solution of poly-sodium 4-styrenesulfonate (PSS) (4 mg/mL) [231], and (4) coating thin layer of SiO_2 [11], [232]. Unfortunately, none of these attempts was successful in preventing Janus particle sticking while maintaining active motion. Further study of the effect of polymers on AC electric field induced active motion could help resolve these challenges. However, a new active particle system may be better suited for studying the effect of high active energies and particle concentration on colloidal gel dynamics and rheology. Other desirable attributes of a such a new active particle system would be cost and environmental sustainability. Some directions for this are suggested in a later section.

5.1.2 Microdynamical implications of active particles in colloidal crystal monolayers

In Chapter 3, we explored how active particles interact with defect-rich colloidal crystal monolayers. Crystal monolayers were made of passive polystyrene spheres with a diameter of 4 μm. The active particle was the same 1 μm platinum Janus particles used in Chapter. The crystal was assembled using AC electric fields. We studied the Janus particle microdynamics and its effect on the properties of defect-rich void regions before and after activity was initiated. Void regions were identified and characterized for properties (size, number, anisotropy, etc.), using a python code.

We found that with increasing activity, void size and anisotropy increased while void number decreased. Additionally, active particles were also more likely to be found in void and void-adjacent regions (within 3 particle diameters) than their passive counterparts. We introduced three possible causes of these changes and described how active motion is the most plausible cause of them.

To better understand how the active motion imparts these changes on the crystal, we studied the microdynamics of active particles in the crystal monolayer. We confirmed that in the crystal, active Janus particle microdynamics were enhanced relative to the passive control. However, the microdynamical enhancement in the crystal was found to be slightly reduced relative to the free particle case. Furthermore, we found that the extent of microdynamical enhancement depended on the microstructural region of the active particle. Specifically, at the greatest active energy, the greatest microdynamical enhancement was found in void-adjacent regions and the least was found in the void regions.

We explained how the difference in regional microdynamics could be the result of the complex interactions of active colloids with their environment, specifically when confined. The

four facets of this complexity that were discussed were: (1) the energy potentials involved with each region; (2) the frequency of collisions found in each region; (3) the energy required for local particle rearrangements; and (4) the active particle interactions dominating in each region.

Considering these results, we proposed that the potential mechanism for these changes is the following: void properties change as a result of active particle collisions with the lattice. However, the local environment influences a particle's microdynamics and thereby its ability to transfer energy to the lattice and change void properties.

These results have many implications for our understanding of active motion and its effects on colloidal crystals. They suggest that changes in void properties and activity-controlled annealing are mostly likely mediated by the dynamical interactions in void-adjacent regions. Furthermore, they suggest that active particles in different microstructural regions contribute to changes in void properties to different extents. More generally, these results indicate that just as the active particle affects the crystal structure, the crystal structure affects the microdynamics of the active particle. Therefore, when considering future studies and applications where greater microstructural change is desired, this work suggests that it will be important to control active particle location as well as the specific active propulsion mechanism.

Like Chapter 3, the activity regime studied was limited due to bubble interference. By extension, the continued effects that active particles could have on the crystal were also limited. For example, trends in void properties could be strengthened with more time and active energy points and better compared with existing studies [58], [66]. Therefore, an important area for further research is to use a different active matter system without (or with more limited) bubble interference. Suggestions related to this active particle system selection will be discussed in the next section. It would also be interesting to study the microdynamics of the crystal lattice itself to

better understand the energy transfer that contributes to changes in void properties as well as to understand how active particles affect the rigidity of the lattice [233]. A final consideration for future work is to study how active particle shape (and size) may affect the ability to change void and crystal properties.

5.1.3 The need for a new active matter system

Chapters 2 and 3 continue to highlight an important limitation of the platinum Janus particle system for active motion: only low concentrations of active particles and low active energies (via hydrogen peroxide concentration) can be used before bubble interference. This limitation still allowed for initial studies of the impact of active particles on colloidal gels and colloidal crystals (as shown in this dissertation). However, for continued work and implementation of active particles, a different active particle system is needed. Furthermore, an active particle system without platinum is critical for acceptance in many industries. Platinum is costly and not environmentally sustainable; therefore many applications of active matter would require the use of other catalysts or gradients.

Fortunately, many new active particle systems could address these problems. For example, many researchers have found successful implementation of light activated active particles that don't contain platinum and can achieve higher active energies before bubble interference [58], [74], [178], [234]. One active particle system that the author thinks is promising for this group is the light activated TiO_2/SiO_2 Janus spheres described by Gibbs [9]. This particle could be easily implemented using the resources already readily available at the University of Michigan and the Lurie Nanofabrication facility. Furthermore, silica particles are another well-studied colloidal particle. Another exciting type of active particle system involves biocatalytic reactions with enzymes. Some reactions particularly applicable to biobased or

sustainability applications include those with the enzymes: catalase and urease. When these enzymes are linked to particles, the resulting active motion can have even greater energies (or speeds), will still function in physiological environments, and have little to no toxicity [235], [236].

Ultimately, understanding the desired application and its environment will be critical for active particle selection. As researchers better identify and understand the mechanisms and interactions involved in the motion of an active particle, active particle selection and implementation will be more successful. Furthermore, the creation of new synthetic active matter systems that do not have the limitations of the platinum Janus particle and can be made in higher quantities could allow for more widespread application.

5.2 Electrosprayed inulin microparticles

In Chapter 4, the particles of interest were PVA-inulin microparticles. We studied how the microparticle form in suspension affected rheological properties and ultimately the gut retention of inulin in mice. These microparticles were prepared using the electrospray method with PVA to promote successful particle production. The resulting particles were smaller and more polydisperse than the as-received inulin. FTIR and confocal microscopy confirmed the presence and colocalization of PVA and inulin in the particles. Upon hydration, these particles were observed to swell and agglomerate in both confocal microscopy and mastersizer size distributions. They also remained visually stable for more than four hours.

Because rheological properties have previously been shown to affect gut retention [94], linear and nonlinear measurements of the microparticle suspensions were taken. We found both the microparticle form and the presence of inulin affected these rheological properties. Specifically, the presence of inulin had a greater effect on the viscoelastic behavior at long times

and the microparticle form had a greater effect on the short-time viscoelastic behavior as well as the viscosity and shear thinning behavior. The greater effect of inulin at long times corresponds to the trends from the inulin release profile of these microparticles. This correspondence, as well as the rheological trends, indicate that the release of inulin may be impacting the transient rheological response.

From both *in vivo* quantification methods, we observed a delay in the maximum of fecal inulin content for PVA-inulin microparticles compared to as-received inulin and PVA-inulin mixtures. This finding indicates that the microparticles travel slower through the GI tract and increase its guts retention. We hypothesize that this increase in gut retention is a result of the mucoadhesive properties of PVA and the rheological properties of the samples. Though further characterization is needed to understand how this may ultimately affect any prebiotic benefits, these results already indicate that the microparticle form could improve the availability of inulin in the gut.

To better understand the implications of the microparticle form and sample rheology on the gut retention and the gut microbiome, further study is needed. For example, animal studies investigating the gut microbiome compositions as well as changes in levels of metabolites such as short chain fatty acids could inform of specific prebiotic effects of modified inulin. Furthermore, electrospraying inulin alone could help isolate factors that contribute to the increased gut retention. This could be possible by using a polymer that is not mucoadhesive or through the acetylation of inulin as done by Jain and coworkers [194]. This method could also help determine how particle size may affect inulin retention and bioavailability.

An alternative approach to studying the effect of microparticle form and size on the gut retention and bioavailability of inulin would be to use a different particle production method all

together. One such method is double emulsion precipitation with a colon-targeting polymer as the encapsulating material. This methods has potential for better size control and has successfully been used for inulin and PLGA [237], but not with colon-targeting polymers like Eudragit [238], [239]. Some initial attempts were made and spearheaded by Angelica Rose Galvan, but exact solvents and instrumentation would need to be additionally optimized. Furthermore, these attempts have shown signs of a generally low product yield and production rate which may hinder animal studies. Even still, this and other particle production methods warrant further study.

5.3 Closing

In conclusion, this thesis has shown how colloidal particles and small changes to such particles can have profound impacts on and interactions with their environments. Using insights from this work can help guide future design of active matter systems and prebiotic formulations.

Bibliography

[1] W. B. Russel, D. A. Saville, and W. R. Schowalter, *Colloidal Dispersions*. Cambridge University Press, 1989.

[2] S. C. Glotzer and M. J. Solomon, "Anisotropy of building blocks and their assembly into complex structures," *Nat. Mater. 2007 68*, vol. 6, no. 8, pp. 557–562, 2007.

[3] N. Ruthardt, D. C. Lamb, and C. Bräuchle, "Single-particle tracking as a quantitative microscopy-based approach to unravel cell entry mechanisms of viruses and pharmaceutical nanoparticles," *Mol. Ther.*, vol. 19, no. 7, pp. 1199–1211, 2011.

[4] A. El Kaffas, "Measuring the mechanical properties of apoptotic cells using particle tracking microrheology," Toronto Metropolitan University, 2008.

[5] N. L. Abbott and O. D. Velev, "Active particles propelled into researchers' focus," *Curr. Opin. Colloid Interface Sci.*, vol. 21, pp. 1–3, 2016.

[6] J. Palacci, S. Sacanna, A. Steinberg, D. Pine, and P. Chaikin, "Living Crystals of Light-Activated Colloidal Surfers," *Science (80-.).*, vol. 339, no. 6122, pp. 936–940, Feb. 2013.

[7] J. Palacci, S. Sacanna, S.-H. Kim, G.-R. Yi, D. J. Pine, and P. M. Chaikin, "Light-activated self-propelled colloids," *Philos. Trans. A. Math. Phys. Eng. Sci.*, vol. 372, no. 2029, Nov. 2014.

[8] D. P. Singh, U. Choudhury, P. Fischer, and A. G. Mark, "Non-Equilibrium Assembly of Light-Activated Colloidal Mixtures," *Adv. Mater.*, vol. 29, no. 32, p. 1701328, Aug. 2017.

[9] J. G. Gibbs, "Shape- and Material-Dependent Self-Propulsion of Photocatalytic Active Colloids, Interfacial Effects, and Dynamic Interparticle Interactions," *Langmuir*, p. acs.langmuir.9b02866, Dec. 2019.

[10] S. Gangwal, O. J. Cayre, M. Z. Bazant, and O. D. Velev, "Induced-Charge Electrophoresis of Metallodielectric Particles," *Phys. Rev. Lett.*, vol. 100, no. 5, p. 058302, Feb. 2008.

[11] J. Yan, M. Han, J. Zhang, C. Xu, E. Luijten, and S. Granick, "Reconfiguring active particles by electrostatic imbalance," *Nat. Mater.*, vol. 15, no. 10, pp. 1095–1099, 2016.

[12] A. F. Demirörs, M. T. Akan, E. Poloni, and A. R. Studart, "Active cargo transport with Janus colloidal shuttles using electric and magnetic fields," *Soft Matter*, vol. 14, no. 23, pp. 4741–4749, Jun. 2018.

[13] B. Behdani, K. Wang, and C. A. Silvera Batista, "Electric polarizability of metallodielectric Janus particles in electrolyte solutions," *Soft Matter*, vol. 17, no. 41, pp. 9410–9419, 2021.

[14] H. Massana-Cid, F. Meng, D. Matsunaga, R. Golestanian, and P. Tierno, "Tunable self-healing of magnetically propelling colloidal carpets."

[15] P. Mandal, G. Patil, H. Kakoty, and A. Ghosh, "Magnetic Active Matter Based on Helical Propulsion," *Acc. Chem. Res.*, vol. 51, no. 11, pp. 2689–2698, Nov. 2018.

[16] J. Howse, R. Jones, A. Ryan, T. Gough, R. Vafabakhsh, and R. Golestanian, "Self-Motile Colloidal Particles: From Directed Propulsion to Random Walk," *Phys. Rev. Lett.*, vol. 99, no. 4, p. 048102, Jul. 2007.

[17] S. Ebbens, M. H. Tu, J. R. Howse, and R. Golestanian, "Size dependence of the propulsion velocity for catalytic Janus-sphere swimmers," *Phys. Rev. E*, vol. 85, no. 2, p.

020401, Feb. 2012.
[18] O. Shemi and M. J. Solomon, “Self-Propulsion and Active Motion of Janus Ellipsoids,” *J. Phys. Chem. B*, vol. 122, no. 44, pp. 10247–10255, Nov. 2018.
[19] K. Dietrich, G. Volpe, M. N. Sulaiman, D. Renggli, I. Buttinoni, and L. Isa, “Active Atoms and Interstitials in Two-Dimensional Colloidal Crystals,” *Phys. Rev. Lett.*, vol. 120, 2018.
[20] M. E. Szakasits, K. T. Saud, X. Mao, and M. J. Solomon, “Rheological implications of embedded active matter in colloidal gels,” *Soft Matter*, vol. 15, no. 40, pp. 8012–8021, 2019.
[21] J. R. Howse, R. A. L. Jones, A. J. Ryan, T. Gough, R. Vafabakhsh, and R. Golestanian, “Self-Motile Colloidal Particles : From Directed Propulsion to Random Walk,” *Phys. Rev. Lett.*, vol. 99, no. 4, p. 048102, 2007.
[22] S. C. Takatori and J. F. Brady, “Swim stress, motion, and deformation of active matter: effect of an external field,” *Soft Matter*, vol. 10, no. 47, pp. 9433–9445, 2014.
[23] E. Zaccarelli, “Colloidal Gels: Equilibrium and Non-Equilibrium Routes,” *J. Phys. Condens. Matter*, vol. 19, no. 32, p. 323101, Aug. 2007.
[24] V. J. Anderson and H. N. W. Lekkerkerker, “Insights into phase transition kinetics from colloid science,” *Nat. 2002 4166883*, vol. 416, no. 6883, pp. 811–815, Apr. 2002.
[25] M. J. Solomon, “Personal communications.” .
[26] H.-J. Butt, K. (Karlheinz) Graf, M. 1963- Kappl, H.-J. Butt, K. Graf, and M. Kappl, *Physics and chemistry of interfaces*. Weinheim : Chichester, 2003.
[27] J. Israelachvili, *Intermolecular and Surface Forces*. Elsevier Inc., 2011.
[28] N. Akafuah, S. Poozesh, A. Salaimeh, G. Patrick, K. Lawler, and K. Saito, “Evolution of the Automotive Body Coating Process—A Review,” *Coatings*, vol. 6, no. 2, pp. 1–22, Jun. 2016.
[29] “Colloids in Food: Ingredients, Structure, and Stability,” *Annu. Rev. Food Sci. Technol.*, vol. 6, no. 1, pp. 211–233, Apr. 2015.
[30] T. Gibaud *et al.*, “New routes to food gels and glasses,” *Faraday Discuss.*, vol. 158, no. 0, pp. 267–284, Sep. 2012.
[31] S. Banerjee and S. Bhattacharya, “Food Gels: Gelling Process and New Applications,” *Crit. Rev. Food Sci. Nutr.*, vol. 52, no. 4, pp. 334–346, Apr. 2012.
[32] S. Sinha and S. Tarafdar, “Electric Field Induced Gel Formation and Fracture in Layers of Laponite,” in *Recent Trends in Surface and Colloid Science*, S. P. M. Bidyut Kumar Paul, Ed. World Scientific, 2012, pp. 337–344.
[33] E. Zaccarelli, “Colloidal Gels: Equilibrium and non-equilibrium routes,” *J. Phys. Condens. Matter*, vol. 19, no. 32, p. 323101, 2007.
[34] V. Prasad, V. Trappe, A. D. Dinsmore, P. N. Segre, L. Cipelletti, and D. A. Weitz, “Universal features of the fluid to solid transition for attractive colloidal particles,” *Faraday Discuss.*, vol. 123, pp. 1–12, 2003.
[35] A. H. Krall and D. A. Weitz, “Internal Dynamics and Elasticity of Fractal Colloidal Gels,” *Phys. Rev. Lett.*, vol. 80, no. 4, pp. 778–781, Jan. 1998.
[36] M. Carpineti and M. Giglio, “Spinodal-type dynamics in fractal aggregation of colloidal clusters,” *Phys. Rev. Lett.*, vol. 68, no. 22, pp. 3327–3330, Jun. 1992.
[37] M. Carpineti, F. Ferri, M. Giglio, E. Paganini, and U. Perini, “Salt-induced fast aggregation of polystyrene latex,” *Phys. Rev. A*, vol. 42, no. 12, pp. 7347–7354, 1990.
[38] P. J. Lu and D. A. Weitz, “Colloidal Particles: Crystals, Glasses, and Gels,”

http://dx.doi.org.proxy.lib.umich.edu/10.1146/annurev-conmatphys-030212-184213, vol. 4, no. 1, pp. 217–233, Mar. 2013.
[39] L. C. Hsiao, R. S. Newman, S. C. Glotzer, and M. J. Solomon, "Role of isostaticity and load-bearing microstructure in the elasticity of yielded colloidal gels," *Proc. Natl. Acad. Sci.*, vol. 109, no. 40, pp. 16029–16034, 2012.
[40] W. H. Shih, W. Y. Shih, S. Il Kim, J. Liu, and I. A. Aksay, "Scaling behavior of the elastic properties of colloidal gels," *Phys. Rev. A*, vol. 42, no. 8, pp. 4772–4779, 1990.
[41] A. Mohraz and M. J. Solomon, "Orientation and rupture of fractal colloidal gels during start-up of steady shear flow," *J. Rheol. (N. Y. N. Y).*, vol. 49, no. 3, pp. 657–681, 2005.
[42] M. E. Szakasits, W. Zhang, and M. J. Solomon, "Dynamics of Fractal Cluster Gels with Embedded Active Colloids," *Phys. Rev. Lett.*, vol. 119, no. 5, p. 058001, Jul. 2017.
[43] M. Lattuada, H. Wu, and M. Morbidelli, "A simple model for the structure of fractal aggregates," *J. Colloid Interface Sci.*, vol. 268, pp. 106–120, 2003.
[44] X. Wang, S. M. Husson, X. Qian, and S. R. Wickramasinghe, "Inverse colloidal crystal microfiltration membranes," *J. Memb. Sci.*, vol. 365, no. 1–2, pp. 302–310, Dec. 2010.
[45] B. Yu *et al.*, "A smart thermo- and pH-responsive microfiltration membrane based on three-dimensional inverse colloidal crystals," *Sci. Reports 2017 71*, vol. 7, no. 1, pp. 1–10, Sep. 2017.
[46] H. Yan, S. Sokolov, J. C. Lytle, A. Stein, F. Zhang, and W. H. Smyrl, "Colloidal-Crystal-Templated Synthesis of Ordered Macroporous Electrode Materials for Lithium Secondary Batteries," *J. Electrochem. Soc.*, vol. 150, no. 8, p. A1102, Jun. 2003.
[47] A. Narayanan, F. Mugele, and M. H. G. Duits, "Mechanical History Dependence in Carbon Black Suspensions for Flow Batteries: A Rheo-Impedance Study," *Langmuir*, vol. 33, no. 7, pp. 1629–1638, Feb. 2017.
[48] T. Liu, B. Vansaders, J. T. Keating, S. C. Glotzer, and M. J. Solomon, "Effect of Particles of Irregular Size on the Microstructure and Structural Color of Self-Assembled Colloidal Crystals," *Langmuir*, vol. 37, no. 45, pp. 13300–13308, Nov. 2021.
[49] T. Liu, B. Vansaders, S. C. Glotzer, and M. J. Solomon, "Effect of Defective Microstructure and Film Thickness on the Reflective Structural Color of Self-Assembled Colloidal Crystals," *ACS Appl. Mater. Interfaces*, vol. 12, no. 8, pp. 9842–9850, Feb. 2020.
[50] T. Liu, T. Liu, F. Gao, S. C. Glotzer, and M. J. Solomon, "Structural Color Spectral Response of Dense Structures of Discoidal Particles Generated by Evaporative Assembly," *J. Phys. Chem. B*, vol. 126, no. 6, pp. 1315–1324, Feb. 2022.
[51] A. A. Shah, M. Ganesan, J. Jocz, and M. J. Solomon, "Direct current electric field assembly of colloidal crystals displaying reversible structural color," *ACS Nano*, vol. 8, no. 8, pp. 8095–8103, Aug. 2014.
[52] J. Bin Kim, S. Y. Lee, J. M. Lee, and S. H. Kim, "Designing Structural-Color Patterns Composed of Colloidal Arrays," *ACS Appl. Mater. Interfaces*, vol. 11, no. 16, pp. 14485–14509, Apr. 2019.
[53] P. N. Pusey and W. Van Megen, "Phase behaviour of concentrated suspensions of nearly hard colloidal spheres," *Nature*, vol. 320, no. 6060, pp. 340–342, 1986.
[54] E. C. M. Vermolen *et al.*, "Fabrication of large binary colloidal crystals with a NaCl structure," *Proc. Natl. Acad. Sci. U. S. A.*, vol. 106, no. 38, pp. 16063–16067, Sep. 2009.
[55] A. Van Blaaderen, R. Ruel, and P. Wiltzius, "Template-directed colloidal crystallization," *Nat. 1997 3856614*, vol. 385, no. 6614, pp. 321–324, 1997.

[56] P. K. Kao, B. J. VanSaders, M. D. Durkin, S. C. Glotzer, and M. J. Solomon, “Anisotropy effects on the kinetics of colloidal crystallization and melting: Comparison of spheres and ellipsoids,” *Soft Matter*, vol. 15, no. 37, pp. 7479–7489, 2019.
[57] P.-K. Kao, B. J. VanSaders, S. C. Glotzer, and M. J. Solomon, “Accelerated annealing of colloidal crystal monolayers by means of cyclically applied electric fields,” *Sci. Reports 2021 111*, vol. 11, no. 1, pp. 1–13, May 2021.
[58] S. Ramananarivo, E. Ducrot, and J. Palacci, “Activity-controlled annealing of colloidal monolayers,” *Nat. Commun.*, vol. 10, no. 1, 2019.
[59] H. Míguez *et al.*, “Control of the photonic crystal properties of fee-packed submicrometer SiO2 spheres by sintering,” *Adv. Mater.*, vol. 10, no. 6, pp. 480–483, 1998.
[60] Y. H. Ye, F. LeBlanc, A. Haché, and V. Van Truong, “Self-assembling three-dimensional colloidal photonic crystal structure with high crystalline quality,” *Appl. Phys. Lett.*, vol. 78, no. 1, pp. 52–54, 2001.
[61] L. T. Shereda, R. G. Larson, and M. J. Solomon, “Local stress control of spatiotemporal ordering of colloidal crystals in complex flows,” *Phys. Rev. Lett.*, vol. 101, no. 3, p. 038301, Jul. 2008.
[62] B. J. Ackerson ’ and P. N. Pusey, “Shear-Induced Order in Suspensions of Hard Spheres,” vol. 61, no. 8, 1988.
[63] M. Mittal, P. P. Lele, E. W. Kaler, and E. M. Furst, “Polarization and interactions of colloidal particles in ac electric fields,” *J. Chem. Phys.*, vol. 129, no. 6, p. 064513, Aug. 2008.
[64] T. D. Edwards and M. A. Bevan, “Controlling colloidal particles with electric fields,” *Langmuir*, vol. 30, no. 36, pp. 10793–10803, Sep. 2014.
[65] H. Morgan and N. G. Green, *AC electrokinetics colloids and nanoparticles*. Baldock Hertfordshire England Philadelphia Pa. Williston VT: Research Studies Press ; Institute of Physics Pub. ; Distribution North America AIDC, 2003.
[66] B. Van Der Meer, L. Filion, and M. Dijkstra, “Fabricating large two-dimensional single colloidal crystals by doping with active particles,” *Soft Matter*, vol. 12, no. 14, pp. 3406–3411, 2016.
[67] J. Li *et al.*, “Self-Propelled Nanomotors Autonomously Seek and Repair Cracks,” *Nano Lett.*, vol. 15, no. 10, pp. 7077–7085, 2015.
[68] W. Gao, X. Feng, A. Pei, Y. Gu, J. Li, and J. Wang, “Seawater-driven magnesium based Janus micromotors for environmental remediation †,” *This J. is [a] R. Soc. Chem.*, vol. 4696, no. 5, pp. 4696–4700, 2013.
[69] “Artificial Micromotors in the Mouse’s Stomach: A Step toward in Vivo Use of Synthetic Motors,” *ACS Nano*, vol. 9, no. 1, pp. 117–123, Jan. 2015.
[70] A. K. Omar, Y. Wu, Z. G. Wang, and J. F. Brady, “Swimming to Stability: Structural and Dynamical Control via Active Doping,” *ACS Nano*, vol. 13, no. 1, pp. 560–572, 2019.
[71] B. Liebchen and A. K. Mukhopadhyay, “Interactions in active colloids,” *Journal of Physics Condensed Matter*, vol. 34, no. 8. IOP Publishing, p. 083002, 09-Dec-2022.
[72] K. Dietrich, D. Renggli, M. Zanini, G. Volpe, I. Buttinoni, and L. Isa, “Two-dimensional nature of the active Brownian motion of catalytic microswimmers at solid and liquid interfaces,” *New J. Phys.*, vol. 19, no. 6, 2017.
[73] J. Katuri, R. Poehnl, A. Sokolov, W. Uspal, and A. Snezhko, “Arrested-motility states in populations of shape-anisotropic active Janus particles,” *Sci. Adv.*, vol. 8, no. 26, p. 3604, Jul. 2022.

[74] U. Choudhury, A. V. Straube, P. Fischer, J. G. Gibbs, and F. Höfling, "Active colloidal propulsion over a crystalline surface," *New J. Phys.*, vol. 19, no. 12, 2017.
[75] A. Brown and W. Poon, "Ionic effects in self-propelled Pt-coated Janus swimmers," *Soft Matter*, vol. 10, no. 22, pp. 4016–4027, 2014.
[76] A. E. Patteson, A. Gopinath, and P. E. Arratia, "Active colloids in complex fluids," *Curr. Opin. Colloid Interface Sci.*, vol. 21, pp. 86–96, 2016.
[77] C. Bechinger, R. Di Leonardo, H. Löwen, C. Reichhardt, G. Volpe, and G. Volpe, "Active particles in complex and crowded environments," *Rev. Mod. Phys.*, vol. 88, no. 4, 2016.
[78] N. Koumakis, A. Lepore, C. Maggi, and & R. Di Leonardo, "Targeted delivery of colloids by swimming bacteria," 2013.
[79] L. Wang and J. Simmchen, "Review: Interactions of Active Colloids with Passive Tracers," *Condens. Matter*, vol. 4, no. 3, p. 78, Aug. 2019.
[80] L. Baraban *et al.*, "Catalytic Janus motors on microfluidic chip: Deterministic motion for targeted cargo delivery," *ACS Nano*, vol. 6, no. 4, pp. 3383–3389, Apr. 2012.
[81] L. Baraban, M. Tasinkevych, M. N. Popescu, S. Sanchez, S. Dietrich, and O. G. Schmidt, "Transport of cargo by catalytic Janus micro-motors," *Soft Matter*, vol. 8, no. 1, pp. 48–52, Jan. 2012.
[82] A. Fernandez-Nieves and A. M. Puertas, "Fluids, Colloids and Soft Materials: An Introduction to Soft Matter Physics," *Fluids, Colloids Soft Mater. An Introd. to Soft Matter Phys.*, pp. 1–408, Jan. 2018.
[83] D. I. Wilson, "What is rheology?," *Eye 2018 322*, vol. 32, no. 2, pp. 179–183, Dec. 2017.
[84] D. B. Genovese, J. E. Lozano, and M. A. Rao, "The Rheology of Colloidal and Noncolloidal Food Dispersions," *J. Food Sci.*, vol. 72, no. 2, pp. R11–R20, Mar. 2007.
[85] G. Tabilo-Munizaga and G. V. Barbosa-Cánovas, "Rheology for the food industry," *J. Food Eng.*, vol. 67, no. 1–2, pp. 147–156, Mar. 2005.
[86] P. Fischer, M. Pollard, P. Erni, I. Marti, and S. Padar, "Rheological approaches to food systems," *Comptes Rendus Phys.*, vol. 10, no. 8, pp. 740–750, Nov. 2009.
[87] I. Demirkesen, B. Mert, G. Sumnu, and S. Sahin, "Rheological properties of gluten-free bread formulations," *J. Food Eng.*, vol. 96, no. 2, pp. 295–303, 2010.
[88] P. Glibowski, S. Pikus, J. Jurek, and M. Kotowoda, "Factors affecting inulin crystallization after its complete dissolution," *Carbohydr. Polym.*, vol. 110, pp. 107–112, 2014.
[89] A. J. Reuvers, "Control of rheology of water-borne paints using associative thickeners," *Prog. Org. Coatings*, vol. 35, no. 1–4, pp. 171–181, 1999.
[90] G. H. Mckinley, "Visco-Elasto-Capillary Thinning and Break-Up of Complex Fluids," 2005.
[91] L. Nallely Jimenez, C. D. V Martí Nez Narvá Ez, C. Xu, S. Bacchi, and V. Sharma, "The rheologically-complex fluid beauty of nail lacquer formulations †," *Soft Matter*, vol. 17, p. 5197, 2021.
[92] N. Huang, "Rheological Characterization of Pharmaceutical and Cosmetic Formulations for Cutaneous Applications," *Curr. Pharm. Des.*, vol. 25, no. 21, pp. 2349–2363, Jul. 2019.
[93] R. G. Lentle, Y. Hemar, C. E. Hall, and K. J. Stafford, "Periodic fluid extrusion and models of digesta mixing in the intestine of a herbivore, the common brushtail possum (Trichosurus vulpecula)," *J. Comp. Physiol. B Biochem. Syst. Environ. Physiol.*, vol. 175, no. 5, pp. 337–347, 2005.

[94] K. Han *et al.*, “Generation of systemic antitumour immunity via the in situ modulation of the gut microbiome by an orally administered inulin gel,” *Nat. Biomed. Eng.*, vol. 5, no. 11, pp. 1377–1388, Jun. 2021.
[95] J. Aho, S. Hvidt, and S. Baldursdottir, “Rheology in Pharmaceutical Sciences,” in *Analytical Techniques in the Pharmaceutical Sciences*, Springer, New York, NY, 2016, pp. 719–750.
[96] K. R. N. Moelants, R. Cardinaels, S. Van Buggenhout, A. M. Van Loey, P. Moldenaers, and M. E. Hendrickx, “A Review on the Relationships between Processing, Food Structure, and Rheological Properties of Plant-Tissue-Based Food Suspensions,” *Compr. Rev. Food Sci. Food Saf.*, vol. 13, no. 3, pp. 241–260, May 2014.
[97] D. Weipert, “The Benefits of Basic Rheometry in Studying Dough Rheology’,” 1987.
[98] H. M. Wyss, “Rheology of soft materials,” *Fluids, Colloids Soft Mater. An Introd. to Soft Matter Phys.*, pp. 149–164, 2018.
[99] C. W. Macosko, *Rheology :principles, measurements, and applications*. New York, NY :, 1994.
[100] L. B. Bindels, N. M. Delzenne, P. D. Cani, and J. Walter, “Towards a more comprehensive concept for prebiotics,” *Nat. Rev. Gastroenterol. Hepatol.*, vol. 12, no. 5, pp. 303–310, May 2015.
[101] J. L. Carlson, J. M. Erickson, B. B. Lloyd, and J. L. Slavin, “Health effects and sources of prebiotic dietary fiber,” *Current Developments in Nutrition*, vol. 2, no. 3. 2018.
[102] S. Kolida, K. Tuohy, and G. R. Gibson, “Prebiotic effects of inulin and oligofructose,” *Br. J. Nutr.*, vol. 87, no. S2, pp. S193–S197, May 2002.
[103] J. Eisenlauer and E. Killmann, “Stability of colloidal silica (aerosil) hydrosols. I. Preparation and characterization of silica (aerosil) hydrosols,” *J. Colloid Interface Sci.*, vol. 74, no. 1, pp. 108–119, Mar. 1980.
[104] A. Sun and S. Gunasekaran, “Yield Stress in Foods: Measurements and Applications,” *Int. J. Food Prop.*, vol. 12, no. 1, pp. 70–101, 2009.
[105] J. Colombo and E. Del Gado, “Stress localization, stiffening, and yielding in a model colloidal gel,” *J. Rheol. (N. Y. N. Y).*, vol. 58, no. 5, pp. 1089–1116, Sep. 2014.
[106] R. Wessel and R. C. Ball, “Fractal aggregates and gels in shear flow,” *Phys. Rev. A*, vol. 46, no. 6, 1992.
[107] P. C. F. Møller, S. Rodts, M. A. J. Michels, and D. Bonn, “Shear banding and yield stress in soft glassy materials,” *Phys. Rev. E*, vol. 77, no. 4, pp. 1–5, 2008.
[108] H. J. Walls, S. B. Caines, A. M. Sanchez, and S. A. Khan, “Yield stress and wall slip phenomena in colloidal silica gels,” *J. Rheol. (N. Y. N. Y).*, vol. 47, no. 4, pp. 847–868, Jul. 2003.
[109] M. C. Yang, L. E. Scriven, and C. W. Macosko, “Some Rheological Measurements on Magnetic Iron Oxide Suspensions in Silicone Oil,” *J. Rheol. (N. Y. N. Y).*, vol. 30, no. 5, pp. 1015–1029, Oct. 1986.
[110] T. Divoux, M. A. Fardin, S. Manneville, and S. Lerouge, “Shear Banding of Complex Fluids,” *Annu. Rev. Fluid Mech.*, vol. 48, no. 1, pp. 81–103, Jan. 2016.
[111] D. Bonn, M. M. Denn, L. Berthier, T. Divoux, and S. Manneville, “Yield stress materials in soft condensed matter,” *Rev. Mod. Phys.*, vol. 89, no. 3, p. 035005, 2017.
[112] A. E. James, D. J. A. Williams, and P. R. Williams, “Direct measurement of static yield properties of cohesive suspensions,” *Rheol. Acta*, vol. 26, no. 5, pp. 437–446, Sep. 1987.
[113] J. C. Conrad *et al.*, “Arrested fluid-fluid phase separation in depletion systems:

Implications of the characteristic length on gel formation and rheology," *J. Rheol. (N. Y. N. Y).*, vol. 54, no. 2, pp. 421–438, Mar. 2010.
[114] G. Popkin, "The physics of life," *Nature*, vol. 529, no. 7584, pp. 16–18, 2016.
[115] K. K. Dey, F. Wong, A. Altemose, and A. Sen, "Catalytic Motors—Quo Vadimus?," *Curr. Opin. Colloid Interface Sci.*, vol. 21, pp. 4–13, Feb. 2016.
[116] S. J. Ebbens, "Active colloids: Progress and challenges towards realising autonomous applications," *Curr. Opin. Colloid Interface Sci.*, vol. 21, pp. 14–23, Feb. 2016.
[117] S. J. Ebbens and J. R. Howse, "In pursuit of propulsion at the nanoscale," *Soft Matter*, vol. 6, no. 4, pp. 726–738, 2010.
[118] J. Zhang, E. Luijten, B. A. Grzybowski, and S. Granick, "Active colloids with collective mobility status and research opportunities," *Chemical Society Reviews*, vol. 46, no. 18. pp. 5551–5569, 2017.
[119] J. Palacci, S. Sacanna, A. P. Steinberg, D. J. Pine, and P. M. Chaikin, "Living crystals of light-activated colloidal surfers," *Science (80-.).*, vol. 339, no. 6122, pp. 936–940, 2013.
[120] G. Kokot, G. V Kolmakov, I. S. Aranson, and A. Snezhko, "Dynamic self-assembly and self- organized transport of magnetic micro-swimmers," *Sci. Rep.*, vol. 7, no. 14726, pp. 1–9, 2017.
[121] U. Ohiri, C. W. Shields, K. Han, T. Tyler, O. D. Velev, and N. Jokerst, "Reconfigurable engineered motile semiconductor microparticles," *Nat. Commun.*, vol. 9, no. 1, 2018.
[122] S. Ebbens *et al.*, "Electrokinetic effects in catalytic platinum-insulator Janus swimmers," *EPL*, vol. 106, no. 5, 2014.
[123] S. Ebbens, R. A. L. Jones, A. J. Ryan, R. Golestanian, and J. R. Howse, "Self-assembled autonomous runners and tumblers," *Phys. Rev. E*, vol. 82, no. 1, 2010.
[124] S. J. Ebbens and D. A. Gregory, "Catalytic Janus Colloids: Controlling Trajectories of Chemical Microswimmers," *Acc. Chem. Res.*, vol. 51, no. 9, pp. 1931–1939, 2018.
[125] M. E. Szakasits, W. Zhang, and M. J. Solomon, "Dynamics of Fractal Cluster Gels with Embedded Active Colloids," *Phys. Rev. Lett.*, vol. 119, no. 5, 2017.
[126] M. Carpineti and M. Giglio, "Spinodal-type dynamics in fractal aggregation of colloidal clusters," *Phys. Rev. Lett.*, vol. 68, no. 22, pp. 3327–3330, 1992.
[127] D. Allan, L. Uieda, F. Boulogne, R. W. Perry, T. A. Caswell, and N. Keim, "trackpy: Trackpy v0.2.4," Oct. 2014.
[128] V. Ramasubramani, B. D. Dice, E. S. Harper, M. P. Spellings, J. A. Anderson, and S. C. Glotzer, "freud: A Software Suite for High Throughput Analysis of Particle Simulation Data," *Computer Physics Communications*. 2019.
[129] M. Lattuada, H. Wu, A. Hasmy, and M. Morbidelli, "Estimation of fractal dimension in colloidal gels," *Langmuir*, vol. 19, no. 15, pp. 6312–6316, Jul. 2003.
[130] A. D. Dinsmore, V. Prasad, I. Y. Wong, and D. A. Weitz, "Microscopic Structure and Elasticity of Weakly Aggregated Colloidal Gels," *Phys. Rev. Lett.*, vol. 96, no. 18, pp. 1–6, 2006.
[131] S. C. Takatori, W. Yan, and J. F. Brady, "Swim pressure: Stress generation in active matter," *Phys. Rev. Lett.*, vol. 113, no. 2, pp. 1–5, 2014.
[132] G. Firpo, E. Angeli, L. Repetto, and U. Valbusa, "Permeability thickness dependence of polydimethylsiloxane (PDMS) membranes," *J. Memb. Sci.*, vol. 481, pp. 1–8, May 2015.
[133] A. Mata, A. J. Fleischman, and S. Roy, "Characterization of Polydimethylsiloxane (PDMS) Properties for Biomedical Micro/Nanosystems," *Biomed. Microdevices*, vol. 74, pp. 281–293, 2005.

[134] T. Li, P. Yu, and Y. Luo, “Deoxygenation performance of polydimethylsiloxane mixed-matrix membranes for dissolved oxygen removal from water,” *J. Appl. Polym. Sci.*, vol. 132, no. 4, pp. 1–9, Jan. 2015.
[135] N. B. Uriev and I. Y. Ladyzhinsky, “Fractal models in rheology of colloidal gels,” *Colloids Surfaces A Physicochem. Eng. Asp.*, vol. 108, no. 1, pp. 1–11, Mar. 1996.
[136] J. Bibette, T. G. Mason, Hu Gang, and D. A. Weitz, “Kinetically induced ordering in gelation of emulsions,” *Phys. Rev. Lett.*, vol. 69, no. 6, pp. 981–984, 1992.
[137] D. A. Weitz and M. Oliveria, “Fractal structures formed by kinetic aggregation of aquenous gold colloids,” *Phys. Rev. Lett.*, vol. 52. pp. 1433–1436, 1984.
[138] M. H. Lee and E. M. Furst, “Response of a colloidal gel to a microscopic oscillatory strain.,” *Phys. Rev. E*, vol. 77, no. 4, p. 041408, Apr. 2008.
[139] L. Cipelletti, S. Manley, R. C. Ball, and D. A. Weitz, “Universal aging features in the restructuring of fractal colloidal gels,” *Phys. Rev. Lett.*, vol. 84, no. 10, pp. 2275–2278, 2000.
[140] S. Aime, L. Cipelletti, and L. Ramos, “Power law viscoelasticity of a fractal colloidal gel,” *J. Rheol. (N. Y. N. Y).*, vol. 62, no. 6, pp. 1429–1441, 2018.
[141] R. L. Bagley and P. J. Torvik, “A Theoretical Basis for the Application of Fractional Calculus to Viscoelasticity,” *J. Rheol. (N. Y. N. Y).*, vol. 27, no. 3, pp. 201–210, 1983.
[142] Z. Varga and J. W. Swan, “Large scale anisotropies in sheared colloidal gels,” *J. Rheol. (N. Y. N. Y).*, vol. 62, no. 2, pp. 405–418, 2018.
[143] Z. Varga *et al.*, “Hydrodynamics control shear-induced pattern formation in attractive suspensions,” *Proc. Natl. Acad. Sci.*, vol. 116, no. 25, pp. 12193–12198, Jun. 2019.
[144] W. Gao, A. Pei, X. Feng, C. Hennessy, and J. Wang, “Organized self-assembly of janus micromotors with hydrophobic hemispheres,” *J. Am. Chem. Soc.*, vol. 135, no. 3, pp. 998–1001, Jan. 2013.
[145] F. Schmidt, B. Liebchen, H. Löwen, and G. Volpe, “Light-controlled assembly of active colloidal molecules,” *J. Chem. Phys.*, vol. 150, no. 9, p. 094905, Mar. 2019.
[146] P. Meakin, I. Majid, S. Havlin, and H. Eugene Stanley, “Topological properties of diffusion limited aggregation and cluster-cluster aggregation,” *J. Phys. A Gen. Phys.*, vol. 17, no. 18, pp. L975–L981, 1984.
[147] P. Varadan and M. J. Solomon, “Shear-induced microstructural evolution of thermoreversible colloidal gel,” *Langmuir*, vol. 17, no. 10, pp. 2918–2929, May 2001.
[148] H. Massana-Cid, J. Codina, I. Pagonabarraga, and P. Tierno, “Active apolar doping determines routes to colloidalclusters and gels,” *Proc. Natl. Acad. Sci.*, vol. 115, no. 42, pp. 10618–10623, 2018.
[149] O. Shemi and M. J. Solomon, “Effect of surface chemistry and metallic layer thickness on the clustering of metallodielectric Janus spheres,” *Langmuir*, vol. 30, no. 51, pp. 15408–15415, Dec. 2014.
[150] K. M. Herbert, S. Schrettl, S. J. Rowan, and C. Weder, “50th Anniversary Perspective: Solid-State Multistimuli, Multiresponsive Polymeric Materials,” *Macromolecules*, vol. 50, no. 22, pp. 8845–8870, Nov. 2017.
[151] M. Wei, Y. Gao, X. Li, and M. J. Serpe, “Stimuli-responsive polymers and their applications,” *Polym. Chem.*, vol. 8, no. 1, pp. 127–143, Jan. 2017.
[152] L. Montero De Espinosa, W. Meesorn, D. Moatsou, and C. Weder, “Bioinspired Polymer Systems with Stimuli-Responsive Mechanical Properties,” *Chem. Rev.*, vol. 117, no. 20, pp. 12851–12892, 2017.

[153] N. Deneke, M. L. Rencheck, and C. S. Davis, “An engineer’s introduction to mechanophores,” *Soft Matter*, vol. 16, no. 27, pp. 6230–6252, Jul. 2020.
[154] L. Pavlovsky, J. G. Younger, and M. J. Solomon, “In situ rheology of Staphylococcus epidermidis bacterial biofilms,” *Soft Matter*, vol. 9, no. 1, pp. 122–131, Jan. 2013.
[155] R. H. Ewoldt and G. H. Mckinley, “Creep Ringing in Rheometry or How to Deal with Oft-discarded Data in Step Stress Tests,” *Rheol. Bull.*, vol. 76, pp. 4-6-22–24, Jan. 2007.
[156] H. Cong, B. Yu, J. Tang, Z. Li, and X. Liua, “Current status and future developments in preparation and application of colloidal crystals,” *Chem. Soc. Rev.*, vol. 42, no. 19, pp. 7774–7800, Sep. 2013.
[157] C. M. Doherty, R. A. Caruso, B. M. Smarsly, and C. J. Drummond, “Colloidal crystal templating to produce hierarchically porous LiFePO 4 electrode materials for high power lithium ion batteries,” *Chem. Mater.*, vol. 21, no. 13, pp. 2895–2903, Jul. 2009.
[158] B. VanSaders and S. C. Glotzer, “Sculpting crystals one Burgers vector at a time: Toward colloidal lattice robot swarms,” *Proc. Natl. Acad. Sci. U. S. A.*, vol. 118, no. 3, Jan. 2021.
[159] B. VanSaders and S. C. Glotzer, “Pinning dislocations in colloidal crystals with active particles that seek stacking faults,” *Soft Matter*, vol. 16, no. 17, pp. 4182–4191, 2020.
[160] Y. Qiao, X. Ma, Z. Liu, M. A. Manno, N. C. Keim, and X. Cheng, “Tuning the rheology and microstructure of particle-laden fluid interfaces with Janus particles,” *J. Colloid Interface Sci.*, vol. 618, pp. 241–247, Jul. 2022.
[161] A. Altemose, A. J. Harris, and A. Sen, “Autonomous Formation and Annealing of Colloidal Crystals Induced by Light-Powered Oscillations of Active Particles,” *ChemSystemsChem*, vol. 2, no. 1, Jan. 2020.
[162] B. Van Der Meer, M. Dijkstra, and L. Filion, “Removing grain boundaries from three-dimensional colloidal crystals using active dopants,” *Soft Matter*, vol. 12, no. 25, pp. 5630–5635, Jun. 2016.
[163] J. W. Swan, J. L. Bauer, Y. Liu, and E. M. Furst, “Directed colloidal self-assembly in toggled magnetic fields,” *Soft Matter*, vol. 10, no. 8, pp. 1102–1109, Feb. 2014.
[164] M. Frenkel, P. Arya, E. Bormashenko, and S. Santer, “Quantification of ordering in active light driven colloids,” *J. Colloid Interface Sci.*, vol. 586, pp. 866–875, Mar. 2021.
[165] A. Boymelgreen, G. Yossifon, and T. Miloh, “Propulsion of Active Colloids by Self-Induced Field Gradients,” *Langmuir*, vol. 32, no. 37, pp. 9540–9547, 2016.
[166] A. T. Brown, W. C. K. Poon, C. Holm, and J. De Graaf, “Ionic screening and dissociation are crucial for understanding chemical self-propulsion in polar solvents,” *Soft Matter*, vol. 13, no. 6, pp. 1200–1222, Feb. 2017.
[167] D. B. Allan, T. Caswell, N. C. Keim, and C. M. van der Wel, “trackpy: Trackpy v0.4.1,” Apr. 2018.
[168] K. T. Saud, M. Ganesan, and M. J. Solomon, “Yield stress behavior of colloidal gels with embedded active particles,” *J. Rheol. (N. Y. N. Y).*, vol. 65, no. 2, pp. 225–239, 2021.
[169] A. A. Shah, B. Schultz, W. Zhang, S. C. Glotzer, and M. J. Solomon, “Actuation of shape-memory colloidal fibres of Janus ellipsoids,” *Nat. Mater. 2014 141*, vol. 14, no. 1, pp. 117–124, Nov. 2014.
[170] J. Reback *et al.*, “pandas-dev/pandas: Pandas .” Zenodo, 18-Mar-2020.
[171] S. Van Der Walt *et al.*, “Scikit-image: Image processing in python,” *PeerJ*, vol. 2014, no. 1. PeerJ Inc., p. e453, 19-Jun-2014.
[172] G. Bradski, “The OpenCV Library.” 2000.
[173] O. D. Velev, S. Gangwal, and D. N. Petsev, “Particle-localized AC and DC manipulation

and electrokinetics," *Annual Reports on the Progress of Chemistry - Section C*, vol. 105. pp. 213–246, 2009.
[174] H. Yu *et al.*, "Confined Catalytic Janus Swimmers in a Crowded Channel: Geometry-Driven Rectification Transients and Directional Locking," *Small*, vol. 12, no. 42, pp. 5882–5890, Nov. 2016.
[175] F. Martínez-Pedrero and P. Tierno, "Advances in colloidal manipulation and transport via hydrodynamic interactions," *J. Colloid Interface Sci.*, vol. 519, pp. 296–311, Jun. 2018.
[176] G. Volpe, ab Ivo Buttinoni, D. Vogt, and C. Bechinger ab, "Microswimmers in patterned environments."
[177] W. E. Uspal, M. N. Popescu, M. Tasinkevych, and S. Dietrich, "Shape-dependent guidance of active Janus particles by chemically patterned surfaces," *New J. Phys.*, vol. 20, no. 1, p. 015013, Jan. 2018.
[178] A. L. Holterhoff, M. Li, and J. G. Gibbs, "Self-Phoretic Microswimmers Propel at Speeds Dependent upon an Adjacent Surface's Physicochemical Properties," *J. Phys. Chem. Lett.*, vol. 9, no. 17, pp. 5023–5028, Sep. 2018.
[179] L. J. Perez, T. Bhattacharjee, S. S. Datta, R. Parashar, and N. L. Sund, "Impact of confined geometries on hopping and trapping of motile bacteria in porous media," *Phys. Rev. E*, vol. 103, p. 12611, 2021.
[180] Z. Xiao, M. Wei, and W. Wang, "A Review of Micromotors in Confinements: Pores, Channels, Grooves, Steps, Interfaces, Chains, and Swimming in the Bulk," *ACS Appl. Mater. Interfaces*, vol. 11, no. 7, pp. 6667–6684, Feb. 2019.
[181] A. M.Boymelgreen, G. Kunti, P. Garcia-Sanchez, A. Ramos, G. Yossifon, and T. Miloh, "The role of particle-electrode wall interactions in mobility of active Janus particles driven by electric fields," *J. Colloid Interface Sci.*, vol. 616, pp. 465–475, Jun. 2022.
[182] X. Cao, E. Panizon, A. Vanossi, N. Manini, E. Tosatti, and C. Bechinger, "Pile-up transmission and reflection of topological defects at grain boundaries in colloidal crystals," *Nat. Commun.*, vol. 11, no. 1, Dec. 2020.
[183] M. E. Szakasits, K. T. Saud, X. Mao, and M. J. Solomon, "Rheological implications of embedded active matter in colloidal gels," *Soft Matter*, vol. 15, no. 40, 2019.
[184] Y. Liu *et al.*, "Effect of inulin with different degrees of polymerization on dough rheology, gelatinization, texture and protein composition properties of extruded flour products," *LWT*, vol. 159, p. 113225, Apr. 2022.
[185] L. Zhang, X. Wang, S. Li, J. Sun, and X. Liu, "Effect of inulin on the pasting, textural, and rheological properties of sweet potato starch," *CYTA - J. Food*, vol. 17, no. 1, pp. 733–743, Jan. 2019.
[186] T. V. Nieto-Nieto, Y. X. Wang, L. Ozimek, and L. Chen, "Inulin at low concentrations significantly improves the gelling properties of oat protein - A molecular mechanism study," *Food Hydrocoll.*, vol. 50, pp. 116–127, 2015.
[187] T. Barclay, M. Ginic-Markovic, P. Cooper, and N. Petrovsky, "Inulin - A versatile polysaccharide with multiple pharmaceutical and food chemical uses," *Journal of Excipients and Food Chemicals*, vol. 1, no. 3. International Pharmaceutical Excipients Council of the Americas, pp. 27–50, 23-Nov-2010.
[188] M. A. Mensink, H. W. Frijlink, K. Van Der Voort Maarschalk, and W. L. J. Hinrichs, "Inulin, a flexible oligosaccharide I: Review of its physicochemical characteristics," *Carbohydrate Polymers*, vol. 130. Elsevier Ltd, pp. 405–419, 14-Jun-2015.
[189] T. Van De Wiele, N. Boon, S. Possemiers, H. Jacobs, and W. Verstraete, "Inulin-type

fructans of longer degree of polymerization exert more pronounced in vitro prebiotic effects," *J. Appl. Microbiol.*, vol. 102, no. 2, pp. 452–460, Feb. 2007.
[190] W. Wahbi, R. Siam, J. Kegere, W. A. El-Mehalmey, and W. Mamdouh, "Novel Inulin Electrospun Composite Nanofibers: Prebiotic and Antibacterial Activities," *ACS Omega*, vol. 5, p. 3015, 2020.
[191] D. Zaeim, M. Sarabi-Jamab, B. Ghorani, and R. Kadkhodaee, "Double layer co-encapsulation of probiotics and prebiotics by electro-hydrodynamic atomization," *LWT*, vol. 110, pp. 102–109, Aug. 2019.
[192] S. Beirão-da-Costa *et al.*, "Inulin potential for encapsulation and controlled delivery of Oregano essential oil," *Food Hydrocoll.*, vol. 33, no. 2, pp. 199–206, Dec. 2013.
[193] A. Sarkar *et al.*, "Pickering emulsions co-stabilized by composite protein/ polysaccharide particle-particle interfaces: Impact on in vitro gastric stability," *Food Hydrocoll.*, vol. 84, pp. 282–291, Nov. 2018.
[194] A. K. Jain, V. Sood, M. Bora, R. Vasita, and D. S. Katti, "Electrosprayed inulin microparticles for microbiota triggered targeting of colon," *Carbohydr. Polym.*, vol. 112, pp. 225–234, Nov. 2014.
[195] F. Afinjuomo, S. Abdella, S. H. Youssef, Y. Song, and S. Garg, "Inulin and Its Application in Drug Delivery," *Pharmaceuticals*, vol. 14, no. 9, Sep. 2021.
[196] D. Zaeim, M. Sarabi-Jamab, B. Ghorani, R. Kadkhodaee, W. Liu, and R. H. Tromp, "Microencapsulation of probiotics in multi-polysaccharide microcapsules by electro-hydrodynamic atomization and incorporation into ice-cream formulation," *Food Struct.*, vol. 25, no. 100147, 2020.
[197] A. Popov, E. Enlow, J. Bourassa, and H. Chen, "Mucus-penetrating nanoparticles made with 'mucoadhesive' poly(vinyl alcohol)," *Nanotechnology, Biol. Med.*, vol. 12, pp. 1863–1871, 2016.
[198] S. Oguz, N. Tam, A. Aydogdu, G. Sumnu, and S. Sahin, "Development of novel pea flour-based nanofibres by electrospinning method," *Int. J. Food Sci. Technol.*, vol. 53, no. 5, pp. 1269–1277, May 2018.
[199] B. Felice, M. P. Prabhakaran, M. Zamani, A. P. Rodríguez, and S. Ramakrishna, "Electrosprayed poly(vinyl alcohol) particles: preparation and evaluation of their drug release profile," *Polym. Int.*, vol. 64, no. 12, pp. 1722–1732, Dec. 2015.
[200] M. R. Rostami, M. Yousefi, A. Khezerlou, M. Aman Mohammadi, and S. M. Jafari, "Application of different biopolymers for nanoencapsulation of antioxidants via electrohydrodynamic processes," *Food Hydrocolloids*, vol. 97. Elsevier B.V., p. 105170, 01-Dec-2019.
[201] B. Ghorani and N. Tucker, "Fundamentals of electrospinning as a novel delivery vehicle for bioactive compounds in food nanotechnology," *Food Hydrocolloids*, vol. 51. Elsevier B.V., pp. 227–240, 01-Oct-2015.
[202] C. Jacobsen, P. J. García-Moreno, A. C. Mendes, R. V. Mateiu, and I. S. Chronakis, "Use of Electrohydrodynamic Processing for Encapsulation of Sensitive Bioactive Compounds and Applications in Food," *Annu. Rev. Food Sci. Technol.*, vol. 9, no. 1, pp. 525–549, Mar. 2018.
[203] Y. Kaneo, S. Hashihama, A. Kakinoki, T. Tanaka, T. Nakano, and Y. Ikeda, "Pharmacokinetics and biodisposition of poly(vinyl alcohol) in rats and mice.," *Drug Metab. Pharmacokinet.*, vol. 20, no. 6, pp. 435–442, 2005.
[204] A. Hauser-Kawaguchi, M. Milne, F. Li, T. Y. Lee, and L. G. Luyt, "The development of a

near infrared inulin optical probe for measuring glomerular filtration rate," *Int. J. Biol. Macromol.*, vol. 123, pp. 255–260, Feb. 2019.
[205] R. Perez-Masia, J. M. Lagaron, and A. Lopez-Rubio, "Surfactant-aided electrospraying of low molecular weight carbohydrate polymers from aqueous solutions," *Carbohydr. Polym.*, vol. 101, no. 1, pp. 249–255, Jan. 2014.
[206] C. M. Librán, S. Castro, and J. M. Lagaron, "Encapsulation by electrospray coating atomization of probiotic strains," *Innov. Food Sci. Emerg. Technol.*, vol. 39, pp. 216–222, Feb. 2017.
[207] M. Abyadeh, A. A. Karimi Zarchi, M. A. Faramarzi, and A. Amani, "Evaluation of Factors Affecting Size and Size Distribution of Chitosan-Electrosprayed Nanoparticles," *Avicenna J. Med. Biotechnol.*, vol. 9, no. 3, p. 126, 2017.
[208] A. Í. S. Morais *et al.*, "Fabrication of polymeric microparticles by electrospray: The impact of experimental parameters," *Journal of Functional Biomaterials*, vol. 11, no. 1. 2020.
[209] A. Smeets, C. Clasen, and G. Van den Mooter, "Electrospraying of polymer solutions: Study of formulation and process parameters," *Eur. J. Pharm. Biopharm.*, vol. 119, pp. 114–124, Oct. 2017.
[210] A. Alehosseini, B. Ghorani, M. Sarabi-Jamab, and N. Tucker, "Principles of electrospraying: A new approach in protection of bioactive compounds in foods," *Critical Reviews in Food Science and Nutrition*, vol. 58, no. 14. Taylor and Francis Inc., pp. 2346–2363, 22-Sep-2018.
[211] M. Cloupeau and B. Prunet-Foch, "Electrostatic spraying of liquids: Main functioning modes," *J. Electrostat.*, vol. 25, no. 2, pp. 165–184, Oct. 1990.
[212] J. M. Grace and J. C. M. Marijnissen, "A review of liquid atomization by electrical means," *J. Aerosol Sci.*, vol. 25, no. 6, pp. 1005–1019, Sep. 1994.
[213] H. Melanie, A. Susilowati, Y. M. Iskandar, P. D. Lotulung, and D. G. S. Andayani, "Characterization of Inulin from Local Red Dahlia (Dahlia sp. L) Tubers by Infrared Spectroscopy," *Procedia Chem.*, vol. 16, pp. 78–84, 2015.
[214] W. M. El-Kholy, R. A. Aamer, and A. N. A. Ali, "Utilization of inulin extracted from chicory (Cichorium intybus L.) roots to improve the properties of low-fat synbiotic yoghurt," *Ann. Agric. Sci.*, vol. 65, no. 1, pp. 59–67, Jun. 2020.
[215] P. Padmanabhan, J. Grosse, A. B. M. A. Asad, G. K. Radda, and X. Golay, "Gastrointestinal transit measurements in mice with 99mTc-DTPA-labeled activated charcoal using NanoSPECT-CT," *EJNMMI Res.*, vol. 3, no. 1, p. 60, 2013.
[216] D. Harpaz, T. Axelrod, A. L. Yitian, E. Eltzov, R. S. Marks, and A. I. Y. Tok, "Dissolvable Polyvinyl-Alcohol Film, a Time-Barrier to Modulate Sample Flow in a 3D-Printed Holder for Capillary Flow Paper Diagnostics," *Materials (Basel).*, vol. 12, no. 3, Jan. 2019.
[217] M. Das Kirtania, N. Kahali, and A. Maity, "Inulin-based hydrogel," in *Plant and Algal Hydrogels for Drug Delivery and Regenerative Medicine*, T. K. Giri and B. Ghosh, Eds. Elsevier, 2021, pp. 261–292.
[218] B. Bchir, N. Sadin, S. N. Ronkart, and C. Blecker, "Effect of powder properties on the physicochemical and rheological characteristics of gelation inulin–water systems," *Colloid Polym. Sci.*, vol. 297, no. 6, pp. 849–860, Jun. 2019.
[219] A. K. Hardacre, R. G. Lentle, S. Y. Yap, and J. A. Monro, "Does viscosity or structure govern the rate at which starch granules are digested?," *Carbohydr. Polym.*, vol. 136, pp.

667–675, Jan. 2016.
[220] A. Tamargo, C. Cueva, M. D. Alvarez, B. Herranz, M. V. Moreno-Arribas, and L. Laguna, “Physical effects of dietary fibre on simulated luminal flow, studied by in vitro dynamic gastrointestinal digestion and fermentation,” *Food Funct.*, vol. 10, no. 6, pp. 3452–3465, Jun. 2019.
[221] H. J. Flint, K. P. Scott, S. H. Duncan, P. Louis, and E. Forano, “Microbial degradation of complex carbohydrates in the gut,” *Gut Microbes*, vol. 3, no. 4. Taylor & Francis, Jul-2012.
[222] D. Dryn, J. Luo, M. Melnyk, A. Zholos, and H. Hu, “Inhalation anaesthetic isoflurane inhibits the muscarinic cation current and carbachol-induced gastrointestinal smooth muscle contractions,” *Eur. J. Pharmacol.*, vol. 820, pp. 39–44, Feb. 2018.
[223] W. Suchaoin *et al.*, “Mucoadhesive polymers: Synthesis and in vitro characterization of thiolated poly(vinyl alcohol),” *Int. J. Pharm.*, vol. 503, no. 1–2, pp. 141–149, 2016.
[224] A. Mohraz and M. J. Solomon, “Gelation and internal dynamics of colloidal rod aggregates,” *J. Colloid Interface Sci.*, vol. 300, no. 1, pp. 155–162, 2006.
[225] P. J. Lu, E. Zaccarelli, F. Ciulla, A. B. Schofield, F. Sciortino, and D. A. Weitz, “Gelation of particles with short-range attraction,” *Nature*, vol. 453, no. 7194, pp. 499–503, 2008.
[226] M. Lattuada, H. Wu, and M. Morbidelli, “Radial density distribution of fractal clusters,” *Chem. Eng. Sci.*, vol. 59, no. 21, pp. 4401–4413, 2004.
[227] M. S. Kilic and M. Z. Bazant, “Induced-charge electrophoresis near a wall,” *Electrophoresis*, vol. 32, no. 5, pp. 614–628, Feb. 2011.
[228] C. A. Silvera Batista, H. Rezvantalab, R. G. Larson, and M. J. Solomon, “Controlled Levitation of Colloids through Direct Current Electric Fields,” *Langmuir*, p. acs.langmuir.7b00835, 2017.
[229] F. Ma, S. Wang, L. Smith, and N. Wu, “Two-Dimensional Assembly of Symmetric Colloidal Dimers under Electric Fields,” *Adv. Funct. Mater.*, vol. 22, no. 20, pp. 4334–4343, Oct. 2012.
[230] T. M. Ma, “Fibrin Networks Infected by Staphylococcal Biofilms : Mechanics , Structure and Instability,” University of Michigan, 2018.
[231] J. Gong and N. Wu, “Electric-Field Assisted Assembly of Colloidal Particles into Ordered Nonclose-Packed Arrays,” *Langmuir*, vol. 33, no. 23, pp. 5769–5776, 2017.
[232] X. Huo, Y. Wu, A. Boymelgreen, and G. Yossifon, “Analysis of Cargo Loading Modes and Capacity of an Electrically-Powered Active Carrier,” 2019.
[233] I. Buttinoni and R. P. A. Dullens, “Mechanical properties of colloidal crystals at fluid interfaces,” *JPhys Mater.*, vol. 4, no. 2, p. 25001, 2021.
[234] A. L. Holterhoff, V. Girgis, J. G. Gibbs, R. Li, / Chemcomm, and C. Communication, “Material-dependent performance of fuel-free, light-activated, self-propelling colloids,” *Chem. Commun.*, vol. 56, no. 29, pp. 4082–4085, Apr. 2020.
[235] S. Hermanová and M. Pumera, “Biocatalytic Micro- and Nanomotors,” *Chem. – A Eur. J.*, vol. 26, no. 49, pp. 11085–11092, Sep. 2020.
[236] H. Yuan, X. Liu, L. Wang, and X. Ma, “Fundamentals and applications of enzyme powered micro/nano-motors,” *Bioact. Mater.*, vol. 6, pp. 1727–1749, 2021.
[237] B. Fayed, A. Abood, H. S. El-Sayed, A. M. Hashem, and N. S. H. Mehanna, “A synbiotic multiparticulate microcapsule for enhancing inulin intestinal release and Bifidobacterium gastro-intestinal survivability,” *Carbohydr. Polym.*, vol. 193, pp. 137–143, Aug. 2018.
[238] S. K. Jain, A. K. Jain, and K. Rajpoot, “Expedition of Eudragit® Polymers in the

Development of Novel Drug Delivery Systems," *Curr. Drug Deliv.*, vol. 17, no. 6, pp. 448–469, May 2020.

[239] M. Z. I. Khan, H. P. Štedul, and N. Kurjaković, "A pH-dependent colon-targeted oral drug delivery system using methacrylic acid copolymers. II. Manipulation of drug release using Eudragit® L100 and Eudragit S100 combinations," *Drug Dev. Ind. Pharm.*, vol. 26, no. 5, pp. 549–554, 2000.